Reconstructing gene regulatory pathways from cross-sectional data for the design of basket trials

Pratik Worah*
NYU and Google Research

Cliff Stein
Columbia University

Abstract

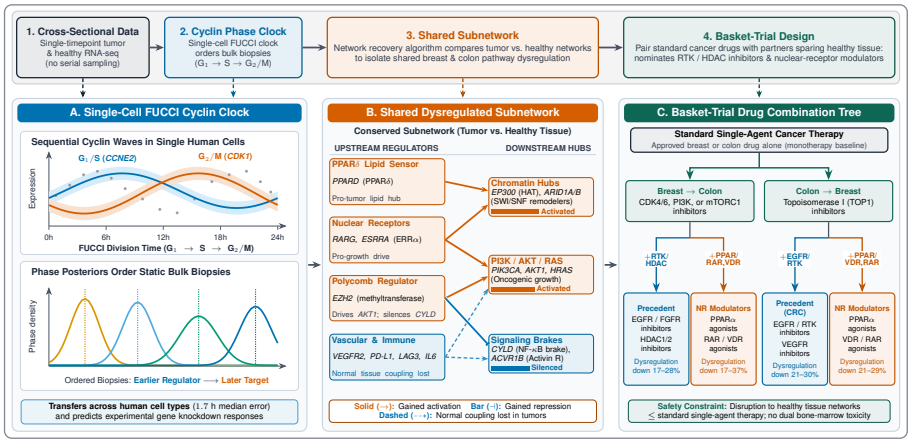
Basket trials match therapies across cancer types using shared biomarkers, yet single-gene markers often miss the pathway-level changes that drive treatment resistance. Discovering pathway markers for basket trials from patient atlases remains difficult because routine biopsies are snapshots, while the space of candidate pathways and drug combinations is combinatorially vast. Here, we use an approximate cyclin clock to order sequencing data from tumor biopsies along the cell cycle and reconstruct the underlying gene regulatory networks. As an application, comparing breast and colorectal tumors against matched healthy tissues uncovers a shared dysregulated subnetwork centered on PPAR nuclear receptors, in which PPARδ gains activating links to pro-growth genes while a tumor-suppressive brake is silenced. We then screen for drug combinations that reverse this shared subnetwork while sparing the healthy-tissue networks. Our predicted combinations pair standard cancer drugs with kinase, HDAC, or nuclear-receptor modulators; the top-ranked ones include drug classes with prior clinical or preclinical support and new candidates for basket trials.

Highlights

- An approximate cyclin clock calibrated on single cells orders tumor biopsies
- A network recovery algorithm reconstructs shared pathways across tumor types
- Breast and colon tumors share PPAR nuclear-receptor dysregulation
- Screening pairs standard cancer drugs with RTK, HDAC, or nuclear-receptor agents

In Brief

Basket clinical trials test whether a drug effective in one cancer can also treat another cancer. However, single drugs often fail when backup pathways restore tumor growth, requiring drug combinations. Designing combinations from patient databases is difficult because biopsies are snapshots that do not show which genes drive one another. Ordering static biopsies with an approximate cell-division clock recovers directed gene pathways. Comparing these pathways between tumors and healthy tissues uncovers regulatory changes shared across breast and colorectal cancers. We then use these pathways to rank drug combinations that counter shared tumor changes while limiting disruption to healthy tissue.



Graphical Abstract. Reconstructing shared dysregulated pathways for basket-trial drug design. Top: Four-stage workflow aligned with Panels A–C below. **(A)** A single-cell FUCCI cyclin clock orders cross-sectional bulk biopsies along cell division ($G_1 \to S \to G_2/M$) so earlier upstream regulators precede later downstream targets. **(B)** Comparing tumor and healthy networks in breast and colorectal cancers reveals a shared set of altered regulatory links centered on the PPAR nuclear-receptor family: *PPARD*, *RARG*, and *ESRRA* gain activating links to *PIK3CA* and chromatin coactivators (*EP300, ARID1A/B*), while *EZH2* activates *AKT1* and represses the NF-κB brake *CYLD*. **(C)** Starting from standard single-agent breast or colon therapies (monotherapy baseline), the screen pairs each therapy with targeted RTK or HDAC inhibitors (blue; classes with clinical or preclinical precedent) or with PPARα, RAR, and VDR agonists not classed as myelosuppressive in our screen (orange), reducing shared pathway dysregulation by up to 37% without increasing disruption to healthy tissue networks.

*Correspondence: `pworah@uchicago.edu`. This work was done independently of the author's Google and NYU affiliations.

1 Introduction

Basket trials test targeted therapies across anatomically distinct cancers that share an actionable molecular alteration [1–6]. When successful, basket trials broaden patient access by repurposing drugs whose clinical dosing and safety are already established in another tumor type. Yet matching solid tumors by a single mutated or overexpressed gene often falls short because signaling pathways contain backup loops that reactivate growth under single-drug blockade. A classic example is *BRAF* V600E inhibition: single-agent therapy produces high response rates in melanoma, whereas colorectal tumors carrying the same mutation rapidly restore proliferation through EGFR unless both proteins are inhibited together [7–9]. Comparable feedback loops drive adaptive resistance to single-agent CDK4/6 and PI3K–AKT–mTOR inhibitors in hormone-receptor-positive breast cancer [10, 11]. Extending basket trials beyond single-gene biomarkers therefore requires mapping how regulatory pathways shift across cancer types and identifying drug pairs that block shared escape routes without compounding toxicity in healthy organs [12].

Large patient atlases such as The Cancer Genome Atlas (TCGA) and the Genotype-Tissue Expression (GTEx) project profile thousands of untreated primary tumors alongside healthy human tissues [13–17]. Despite their clinical breadth, turning cross-sectional tissue atlases into rational combination designs faces two fundamental barriers. First, diagnostic biopsies are snapshots rather than serial samples from the same patient. Standard co-expression analyses measure whether two genes rise and fall together across patients [18–20]. Such analyses capture symmetric association but do not reveal which gene acts upstream and which responds downstream unless additional structural assumptions are imposed [21]. Second, transcriptional drug-repurposing screens such as Connectivity Map and LINCS L1000 rank compounds that invert static differential expression signatures [22]. Treating altered genes as an unordered signature ignores how drug effects propagate through connected tissue networks and provides no safeguard against combinations that disrupt healthy organ homeostasis.

Existing computational network tools address parts of this problem in isolation. Single-cell trajectory and RNA-velocity methods infer directed cellular progression [23, 24], yet large clinical-trial archives and diagnostic repositories consist predominantly of bulk biopsies lacking single-cell resolution. Conversely, regulatory-network reconstruction methods for bulk or single-cell data infer transcription-factor associations from steady-state variation across samples or cells [25–28]. These methods lack an internal temporal ordering and do not explicitly bound disruption to healthy tissues for combination therapy. Bridging routine bulk atlases and combination trial design requires an internal biological clock that orders patient biopsies while remaining robust to biopsy noise and tissue pooling.

Here, we introduce a computational basket-trial design framework that combines a cell-division clock calibrated on single-cell data, a directed network recovery algorithm, and constrained optimization for drug screening. Calibrating a compact cyclin clock on human cells profiled concurrently by scRNA-seq and fluorescent cell-cycle indicator (FUCCI) reporters [29–31] allows us to order cross-sectional bulk biopsies along cell division. This ordering separates upstream regulators from downstream targets across a 100-gene panel of nuclear receptors and druggable cancer genes [32–35].

We first validate directed network recovery across stochastic simulations, cross-lineage single-cell transfer, pooled pseudo-bulk cohorts, and shRNA knockdowns. Applying this framework to primary luminal A (LumA)[1] breast and chromosomally unstable (CIN)[2] colorectal cancers then reveals a set of 107 regulatory changes shared by both cancers and centered on the PPAR family of nuclear receptors. In this shared subnetwork, the nuclear receptors *PPARD* and *RARG* [38, 39] and the chromatin regulator *EZH2* [40] switch on chromatin coactivators and growth-promoting genes such as *PIK3CA* and *AKT1* [41], and switch off the tumor suppressor *CYLD* [42].

We then use constrained optimization to pair standard breast and colorectal therapies with

[1] Luminal A is the predominant hormone-receptor-positive ($ER^+/PR^+, HER2^-$) breast cancer subtype [13, 36].

[2] Chromosomal instability (CIN) is the predominant microsatellite-stable, aneuploid colorectal cancer subtype [14, 37].

candidate partner drugs that reverse this shared tumor subnetwork without increasing disruption to healthy organ networks. Without training on clinical outcomes, the screen ranks several combination classes with clinical or preclinical precedent among its top candidates, most strongly TOP1 chemotherapy with EGFR or VEGF-pathway inhibitors, which improved outcomes in Phase III colorectal trials [43–46]. The screen also nominates PPARα, retinoid, and vitamin D receptor (VDR) agonists, none of which was classed as bone-marrow suppressing in our screen, as partners for standard breast and colorectal therapies.

2 Results

2.1 Overview of the computational basket-trial design framework

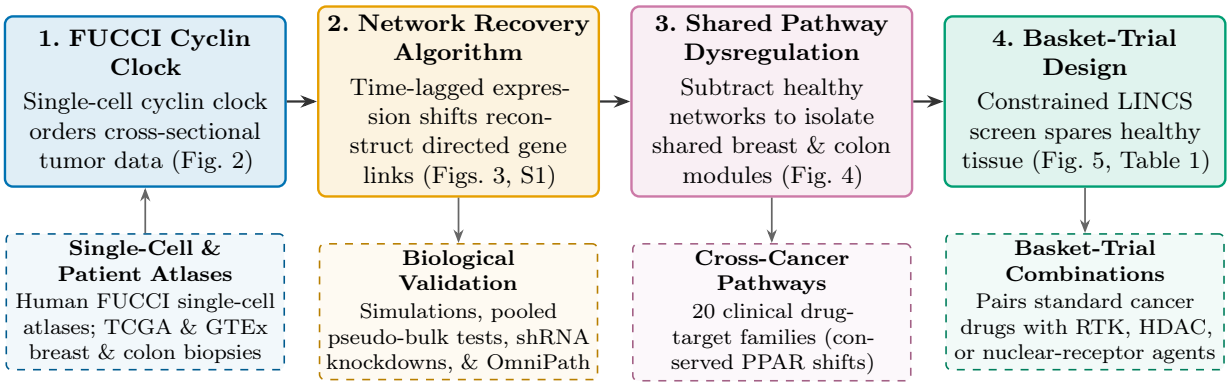


Figure 1: **Four-stage workflow.** (1) A cyclin clock calibrated on single-cell FUCCI fluorescence orders biopsies along the cell cycle (Section 2.3; Figure 2). (2) Comparisons between earlier and later biopsies yield directed gene networks, validated on simulations, pooled single cells, knockdowns, and curated pathways (Sections 2.2–2.4; Figures 2, 3, and S1). (3) Comparing tumor and matched healthy networks isolates changes shared by breast and colorectal cancers (Section 2.5; Figure 4). (4) A drug screen constrained to spare healthy-tissue networks ranks partner drugs for standard therapies (Sections 2.7–2.8; Figure 5; Table 1). Bottom row, data inputs and outputs of each stage.

Figure 1 summarizes our workflow, which is easiest to motivate by working backward from the clinical goal. To design a cross-cancer drug combination, we need to know which tumor pathway changes a partner drug should reverse and which healthy-tissue pathways it should leave intact (Stage 4). Finding those changes requires comparing tumor and healthy gene regulatory networks (Stage 3). Reconstructing those networks requires knowing which genes act upstream and which respond downstream (Stage 2). That, in turn, requires placing biopsies in time order, information that routine single-visit biopsies lack (Stage 1). Because dividing cells pass through the gap, DNA-synthesis, and mitotic phases in a fixed order, cell division provides a biological clock embedded within routine patient cohorts. Below, we describe the four stages in more detail in the forward direction, from biopsies to drug combinations:

1. Cell-cycle clock (Stage 1; Figure 2): A Bayesian Fourier clock, calibrated on single cells whose cell-cycle phase was measured by FUCCI fluorescence, orders bulk RNA-seq biopsies along the cell cycle ($G_1 \to S \to G_2/M$) using cyclin and mitotic transcripts such as *CCNB1*, *CDK1*, and *TOP2A*.
2. Network recovery (Stage 2; Figures 2 and 3; Figure S1): If high expression of regulator j in biopsies from earlier phases is followed by higher or lower expression of target i in biopsies from later phases, j likely activates or represses i; ordinary co-expression cannot make this distinction without additional structural assumptions [21]. Our algorithm (Algorithm 1; Section 5.3.4) detects these lead–lag patterns by comparing biopsies roughly one-sixth of a cycle apart (≈ 1 rad). Our 100-gene panel comprises 29 nuclear receptors and 71 solid-tumor

drug targets (Table S8). Because patient cohorts contain fewer biopsies than candidate gene pairs on this panel, a group-sparsity penalty keeps only a small set of active upstream hub regulators [32, 47–49]. Our theorems (Theorems 1 and 2 in Methods; proofs in Supplementary Section S1) show that this coarse lag averages out local errors in the clock ordering, cancels patient-specific baseline differences, and reduces uneven progression speed to a single positive scale factor.

3. Shared pathway changes (Stage 3; Figure 4): Rescaling each tumor and matched healthy network to unit size (Frobenius norm) removes organ-specific differences in proliferation rate. Comparing the signs of interactions between tumor and healthy networks then isolates pathway changes shared by breast and colorectal cancers (Methods).
4. Drug-combination screen (Stage 4; Figure 5; Table 1): Rather than ranking compounds by how well they reverse a list of altered genes, we propagate 6-h LINCS drug-response profiles [22] through the inferred networks. Standard therapies such as *palbociclib*, *everolimus*, and *irinotecan* are paired with candidate oncology or nuclear-receptor partners under three constraints (Algorithm 2): (i) the two drugs have non-overlapping primary targets and do not both suppress the bone marrow; (ii) the combination engages the shared subnetwork at least as strongly as the standard therapy alone at full dose; and (iii) predicted disruption of the recipient organ's healthy network is no greater than with the standard therapy alone. Because the same networks score both tumor efficacy and healthy-tissue sparing, toxicity control is built into the screen rather than applied afterward.

Together, these stages turn routine tumor and healthy biopsies into directed gene networks, isolate the pathway changes shared across cancers, and rank drug combinations that reverse those changes while sparing healthy tissue. Before analyzing patient tumors, we tested how clock errors and tissue pooling affect network recovery.

2.2 Interaction signs survive clock noise and tissue pooling

Any transcriptomic progression clock applied to clinical RNA-seq biopsies encounters two distinct sources of measurement distortion. First, division phases estimated from a single expression profile per sample carry substantial estimation noise compared with live-cell imaging markers. Second, rather than capturing a single synchronized cell, each bulk tissue biopsy averages thousands of cells whose division timing is only partially aligned, which dampens expression swings across the cycle. Determining when directed regulatory links survive both distortions is therefore a prerequisite for analyzing archival patient cohorts.

To test recovery against a known answer, we simulated a 10-gene stochastic gene-regulatory system with known interactions, sampled unordered cells from it, and ordered them with a noisy clock whose error matches that of our human single-cell clock ($\sigma_{\text{clock}} = 0.45$ rad; Methods and Supplementary Section S1). We then asked whether our algorithm recovers the true interactions across clinical cohort sizes and a tenfold range of progression speeds, comparing it with two baselines: the same estimate without the sparsity penalty (an unpenalized fit), and our algorithm applied to randomly ordered samples (Figure S1, left). Before running the simulations, we fixed two recovery criteria: (i) sign accuracy, the fraction of true interactions whose sign (activation or repression) is recovered correctly, had to exceed its random-order average by at least 10 percentage points; and (ii) the correlation between estimated and true interaction strengths had to exceed the 95th percentile of random orderings. Finally, we simulated pooled bulk biopsies by averaging 100 partially synchronized cells per sample, with progressively wider spread in cell-cycle phase, to test whether interaction signs survive when pooling shrinks the estimated strengths (Figure S1, right).

Both criteria were met in all 12 single-cell simulation settings ($n = 91$–$1{,}000$). Our algorithm recovered the correct sign for 85.6–91.9% of true interactions, versus $\approx 50\%$ (chance) for random orderings, and its estimated strengths correlated with the true strengths at $r = 0.283$–0.577, compared with $r = 0.088$–0.518 for unpenalized fits (Table S1). In the nine pooled-bulk settings, wider phase spread within each biopsy shrank the estimated interaction strengths, as expected

when cells at different phases are averaged together. Interaction signs were more robust: sign accuracy exceeded the 95th percentile of random orderings in 7 of 9 settings, reaching 73.5–81.9% when cells within a biopsy were tightly synchronized (0.3 rad spread) and 56.5–59.6% at moderate (1.0 rad) spread (Table S2).

For drug design, the sign of an interaction is the most useful quantity: it states whether a regulator activates or represses its target, and therefore whether inhibiting that regulator should lower or raise the target's expression. Interaction strengths, by contrast, depend on each tissue's proliferation rate and on how many unsynchronized cells a biopsy pools, so they cannot be compared directly between tumor and healthy tissue or between breast and colon. Because signs survive pooling, later sections compare tumor and healthy networks by their interaction signs. This strategy requires a clock that works reliably across human cell types, which we build and test next.

2.3 A cell-cycle clock calibrated on single cells works across cell types and pooled samples

The simulations above used a synthetic clock with the error level of a real one. To analyze patient biopsies, we need an actual clock that reads cell-cycle phase from gene expression and works across human cell types without recalibration. We designed this clock around two requirements. First, it uses only core cell-cycle genes, calibrated against FUCCI fluorescence (a direct reporter of each cell's cycle phase), so that the same parameters apply to cell types that divide at different speeds. Second, none of its genes belong to the 100-gene panel whose network we infer, so ordering the samples cannot bias the inferred interactions.

We built the clock from 11 well-known cell-cycle genes (*CCND1–3*, *CCNE1–2*, *CCNA2*, *CCNB1–2*, *CDK1*, *UBE2C*, and *TOP2A*; Methods; Table S8). Each of these genes rises and falls at a characteristic point in the cycle: G_1/S cyclins peak early, S-phase genes in the middle, and G_2/M mitotic genes late. To learn these patterns, we used 1,146 human U2OS osteosarcoma cells in which both the transcriptome (scRNA-seq) and the true cycle position (two-color FUCCI reporters, over a 25.4 h cycle) were measured in the same cell [31]. For each clock gene, we fitted a smooth periodic curve (a two-harmonic Fourier series) giving its expected expression at every point in the cycle (Figure 2A). For a new cell or sample, the clock compares its 11-gene expression profile with these curves and uses Bayes' rule to compute the probability of each cycle position. Held-out cells typically had a single clear most-likely position (Figure 2C). To test whether the clock generalizes, we froze all parameters learned from U2OS cells and applied the clock unchanged to 888 human induced pluripotent stem cells (iPSCs) from six donors [30]. Finally, because patient biopsies are bulk samples rather than single cells, we mimicked bulk tissue by pooling 100 held-out U2OS cells into each sample, a standard "pseudo-bulk" construction in single-cell analysis [50, 51]. Unlike real biopsies, these pooled samples come with a known reference: the network inferred from the same cells individually, ordered by their measured FUCCI time. This lets us check whether ordering pooled samples by the clock recovers that reference network.

The clock placed held-out U2OS cells close to their true cycle position (median error 1.71 h, or 6.7% of the cycle, across 20 held-out splits), and it still worked, though less precisely, in stem cells it had never seen (median error 3.62 h). In both cases it beat all 1,000 clocks trained on shuffled labels ($p < 0.001$; Figure 2B,E; circular correlation 0.760 in U2OS and 0.447 in iPSCs; pairwise concordance 72.1% in U2OS). In pooled cohorts of clinical size ($n \in \{91, 171, 245\}$), clock ordering beat random orderings in all 12 settings, and networks inferred after clock ordering matched the single-cell reference network as well as networks inferred after ordering by the measured FUCCI fluorescence itself ($r = 0.300$–0.366 versus $r = 0.296$–0.367 across 100 stratified 20-gene subsets of cancer and nuclear-receptor genes; $r = 0.604$–0.713 for clock ordering on strongly cycling genes; Figure 2F; Table S3).

Thus, a clock trained on one human cell line works on an unrelated cell type without retraining, and orders pooled samples as well as direct fluorescence measurements do. This gives us confidence to apply the same clock, unchanged, to patient tumor and healthy-tissue biopsies.

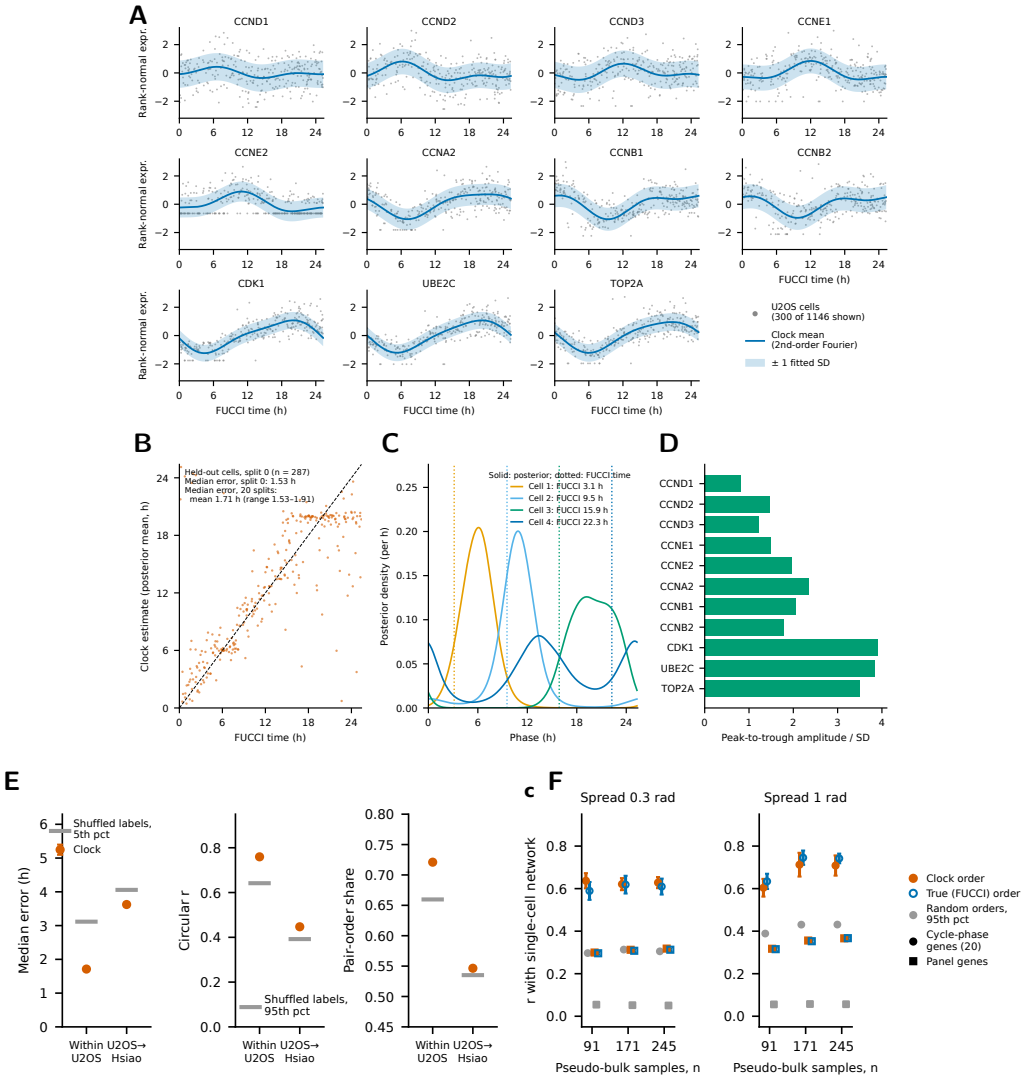


Figure 2: **Validation of the 11-gene cell-cycle clock (Section 2.3).** (A) Expression of the 11 clock genes in 300 U2OS cells (grey dots) versus measured FUCCI time, with fitted curves (blue) and ±1 SD bands (light blue). (B) Predicted versus measured cycle time for held-out U2OS cells ($n = 287$; dashed line, $y = x$). (C) Predicted phase probabilities for four held-out cells; dotted lines, measured times. (D) Signal-to-noise ratio of each clock gene. (E) Clock accuracy in held-out U2OS cells and in 888 iPSCs [30] (orange) versus 1,000 clocks trained on shuffled labels (grey, 5th–95th percentiles). (F) Correlation r between networks from 100-cell pooled samples and the single-cell reference network, for clock (orange), FUCCI (blue), and random (grey, 95th percentile) orderings; circles, 20 cycling genes; squares, 100 subsets of cancer and nuclear-receptor genes (Table S3).

2.4 Clock-ordered patient networks show cell-cycle waves and predict knockdown responses

Having shown that the clock orders pooled cell-line samples accurately, we next applied it to patient biopsies. These are harder: each biopsy mixes tumor cells with stromal and immune cells, patients differ genetically, and tissues divide more slowly than cell lines. We therefore used two tests of whether clock ordering captures genuine tumor biology rather than artifacts. First, if the clock orders patients correctly, genes that change over the cell cycle but were not used to build the clock should rise and fall smoothly from one patient to the next, much as they do over time within a single dividing cell. If the ordering were essentially random, by contrast, neighboring patients would be unrelated and these genes would show no consistent pattern. Second, the inferred tumor networks should predict how cells respond when individual genes are experimentally knocked down.

We trained the clock of Section 2.3 on all 1,146 U2OS cells and applied it without further changes to four TCGA and GTEx bulk RNA-seq cohorts [13, 14, 16, 17]: untreated primary LumA breast cancer ($n = 498$), primary CIN colorectal cancer ($n = 245$), matched healthy breast ($n = 217$, pooling 96 TCGA adjacent-normal and 121 GTEx mammary samples), and healthy colon ($n = 91$, pooling 43 TCGA adjacent-normal and 48 GTEx mucosal samples; Methods). We first removed expression differences explained by each biopsy's mix of epithelial, stromal, and immune cells and by differences between data sources (Tables S8 and S9). When patients were then ordered by the clock, genes outside the clock, such as the Polycomb methyltransferase *EZH2* and the hypoxia factor *EPAS1*, rose and fell smoothly, whereas randomly ordered patients showed flat profiles (Figure 3A,B).

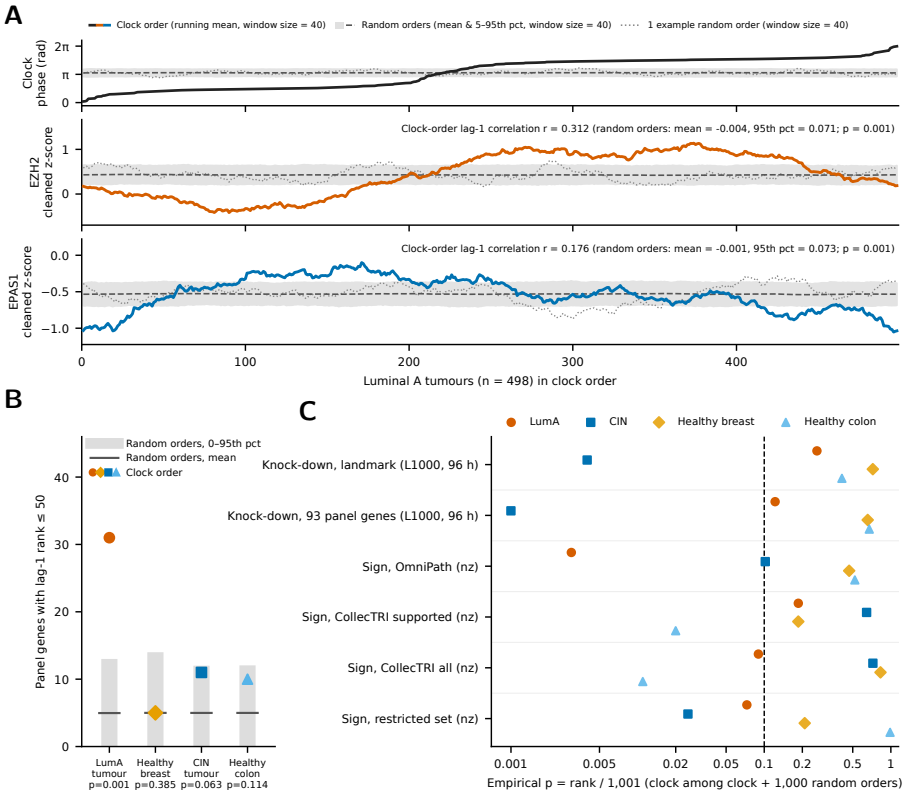


Figure 3: **Validation of clock-ordered networks in patient biopsies (Section 2.4).** (A) Running averages (window of 40) of clock phase (top) and adjusted expression of the non-clock genes *EZH2* (middle) and *EPAS1* (bottom) across 498 LumA breast tumors ordered by the clock; grey band, 5th–95th percentiles of 1,000 random orderings; dashed line, their mean; dotted line, one random ordering. (B) Number of the 93 non-clock genes with significant lag-1 autocorrelation ($p \leq 0.05$) in each cohort (symbols) versus random orderings (tick, mean; grey bar, 0–95th percentiles). (C) Permutation p-values (log scale; dashed line, $p = 0.10$) for comparisons with LINCS shRNA knockdowns and curated OmniPath and CollecTRI interactions (all 42 tests in Table S4).

Ordering by the clock passed both tests. For the first test, we measured smoothness as the correlation between a gene's expression in neighboring patients along the ordering (lag-1 autocorrelation) and compared it with 1,000 random orderings of the same patients. In LumA breast tumors, 31 of the 93 genes outside the clock varied significantly more smoothly than under random ordering ($p = 0.001$), including *EZH2* ($r = 0.312$) and *EPAS1* ($r = 0.176$; both $p = 0.001$). In CIN colon tumors, 11 of 93 genes did so ($p = 0.063$). Healthy tissues, which divide more slowly and therefore carry a weaker cell-cycle signal, showed fewer such genes (Figure 3B).

For the second test, we fixed 42 tests in advance, each comparing an inferred network with experimental perturbation data or curated pathway databases. If our networks were no better

than random, about 4 of these tests (10%) would pass at $p \leq 0.10$ by chance; 14 passed (binomial $p = 8.4 \times 10^{-5}$), including 9 of the 24 tests on the two tumor cohorts ($p = 2.8 \times 10^{-4}$; Table S4). The strongest evidence came from gene knockdowns: the CIN colon network predicted how expression changed 96 h after shRNA knockdown of individual genes in the LINCS resource [22] ($p = 0.004$ for the 24 directly measured landmark genes; $p = 0.001$ across all 93 panel genes), and the LumA network did so only under stricter sparsity settings (Table S10). Inferred interaction signs also agreed with the curated OmniPath [52, 53] ($p = 0.003$ in LumA) and CollecTRI [54] ($p = 0.011$–0.020 in healthy colon) databases (Table S4). One family of tests failed: the networks predicted the effects of broad chromosomal copy-number changes no better than random orderings (Figure 3C; Table S4).

Networks inferred from clock-ordered patient biopsies therefore predict independent knockdown experiments and agree with curated pathway directions, although they do not capture the effects of broad chromosomal copy-number changes.

2.5 Breast and colorectal cancers share regulatory changes centered on PPAR receptors

The previous section showed that clock-ordered networks are reliable within each tissue. This section compares them across tissues to find regulatory changes shared by breast and colorectal cancers, which are the natural targets for basket-trial combinations. Such a comparison must first remove differences that reflect the organ rather than the cancer. Colonic crypts and colorectal tumors divide quickly, so their estimated interaction strengths are roughly twice as large as those in breast tissue (Figure S2); comparing raw strengths would therefore mostly reflect the colon. We avoid this by rescaling each network to the same total size (unit Frobenius norm) and then comparing only the signs of interactions, which the simulations showed to be robust.

After this rescaling, breast and colorectal tumors share far more altered interactions than expected by chance, and the shared changes concentrate in a compact 107-link shared subnetwork. To find them, we labeled each strong interaction in each network as activating, neutral, or inhibitory, and, for each cancer, compared the label in the tumor with the label in the matched healthy tissue (Methods). An interaction counts as altered when its label differs between tumor and healthy tissue, for example when an activating link becomes neutral. Of the 9,900 possible directed interactions among our 100 genes, 1,339 were altered in both cancers, and 663 were altered in the same direction in both. Both counts exceed those obtained in 1,000 control comparisons with shuffled gene labels ($p = 0.001$ and $p = 0.014$; Table S5). We then looked for groups of regulators and targets in which these shared changes cluster, selecting the three densest blocks of 8 regulators by 8 targets. Together, these blocks form the shared subnetwork of 107 changes linking 19 upstream regulators to 22 downstream genes: 59 interactions shift toward activation in tumors (gained activation or lost repression), and 48 shift toward repression (lost activation or gained repression; Figure 4; Figure S3).

Which kinds of regulators drive these shared changes? We grouped the regulators on our panel into the 20 clinical drug-target families they belong to, such as receptor tyrosine kinases, histone deacetylases, and PPAR receptors [33, 34], and asked whether the changes in each family's outgoing interactions were similar in breast and colorectal tumors. Only the PPAR nuclear-receptor family showed a similarity that survives correction for testing 20 families: the PPAR receptors (*PPARA, PPARD, PPARG*) [38, 55] changed in similar ways in both cancers (correlation of outgoing changes $r_G = 0.296$, defined in Section 5.4; $\mathrm{FDR}_{20} = 0.040$[3]; Table S6). Polycomb and DNA-methyltransferase regulators (*EZH2, DNMT3A*) showed weaker, suggestive similarity ($\mathrm{FDR}_{20} = 0.070$) [40], and insulin-like growth factor (*IGF1R*), retinoid, angiogenic, immune-checkpoint, and lipid-kinase families were similar only before correction. By contrast, *HDAC1/2* showed no shared change ($r_G = -0.240$; Table S6) [39, 41, 56–58].

[3] FDR_{20} is the Benjamini–Hochberg false discovery rate across the 20 drug-target families tested. Testing many families at once makes some small p-values likely by chance, so we report this corrected value: an FDR_{20} of 0.040 means that, among families called significant at this level, about 4% are expected to be false positives.

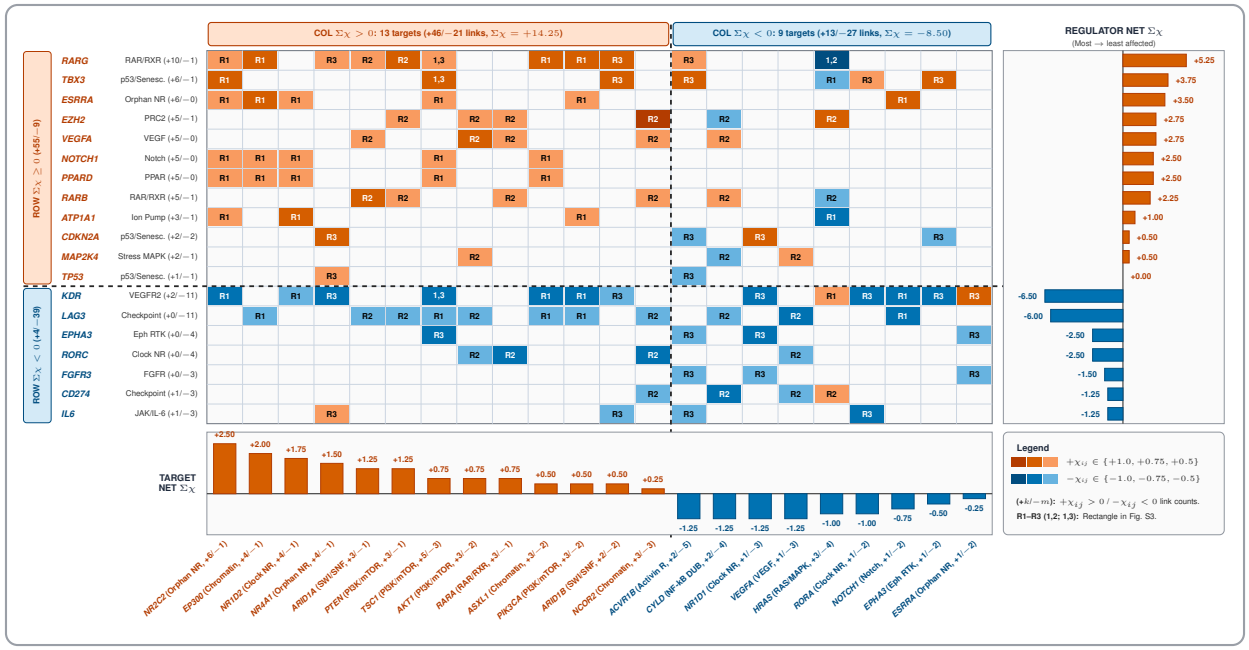


Figure 4: Subnetwork of 107 interactions altered in both LumA breast and CIN colorectal cancers (Sections 2.5–2.6). Rows, 19 upstream regulators; columns, 22 targets, drawn from three blocks R1–R3 (Figure S3). Cell color gives the average change in interaction sign from healthy to tumor tissue across both cancers (χ_{ij}): orange, toward activation (59 links); blue, toward repression (48 links); shade, magnitude (0.50, 0.75, 1.00). Bars, net change per row and column ($\Sigma\chi$); labels, numbers of positive and negative links per gene ($+k/-m$). Definitions in Section 5.3.6.

Thus, although LumA breast tumors arise in hormone-responsive mammary ducts and colorectal tumors in the rapidly renewing intestinal lining, both share a set of regulatory changes centered on the PPAR receptor family, with weaker similarity in Polycomb regulators. We next examine which specific genes these regulators switch on or off within the shared subnetwork.

2.6 Shared changes link nuclear receptors and EZH2 to growth genes

Healthy mammary ducts and colonic crypts both maintain their structure by balancing stem- and progenitor-cell renewal against differentiation, using nuclear receptors, chromatin regulators, and signals from the surrounding stroma [38, 39, 59]. To see which of these controls change in both cancers, we examined the individual links of the shared subnetwork.

Links from receptors for microenvironmental signals mostly shift toward repression in both cancers (Figure 4; Figure S3). In healthy breast and colon, signals from blood vessels and immune cells help coordinate epithelial maturation during routine tissue renewal. In tumors, the vascular endothelial receptor *KDR*, the immune-checkpoint proteins *LAG3* and *CD274*, the inflammatory cytokine *IL6*, and receptor kinases that respond to stromal signals (such as *FGFR3*; complete row counts in Figure 4) all show shared shifts toward repression. These shifts mainly reflect the loss of activating links, present in healthy tissue, onto chromatin-remodeling subunits and onto the activin receptor *ACVR1B*, which promotes epithelial differentiation [60]. This pattern is consistent with tumor cells becoming less responsive to differentiation signals from their surroundings.

Links from intracellular regulators shift the other way (Figure 4; Figure S3). In tumors, the lipid-sensing receptor *PPARD* (+5/0 shared positive/negative links), the retinoic acid receptor *RARG* (+10/−1), the metabolic orphan receptor *ESRRA* (+6/0), and the stress kinase *MAP2K4* (+2/−1) switch from neutral or repressive links in healthy tissue to activating links onto *PIK3CA* and the chromatin coactivators *EP300*, *ARID1A*, *ARID1B*, and *ASXL1* [38, 59, 61]. In tumors, the Polycomb methyltransferase *EZH2* [40] (+5/−1) activates *AKT1* and *HRAS* and represses *CYLD*,

a deubiquitinase and tumor suppressor that inhibits NF-κB signaling [42]. By contrast, the tumor suppressor *RARB* [39] (+5/−1) activates growth-restraining genes (*PTEN, CYLD, NCOR2*) and represses *HRAS*. Thus, in our networks, *PPARD* and *RARG* links point toward growth, whereas *RARB* links point toward growth restraint and differentiation.

In summary, the shared subnetwork shows two opposing changes in both cancers: microenvironmental receptors lose activating links onto differentiation genes, while nuclear receptors and *EZH2* gain activating links onto shared growth genes and *EZH2* represses the growth brake *CYLD*. Together, these changes define a multi-gene target for combination therapy.

2.7 Drug screening ranks combination classes with clinical or preclinical precedent

Drug combinations fail in the clinic either when unblocked feedback pathways restore tumor proliferation or when overlapping toxicities in healthy organs, such as dual bone-marrow suppression, force doses too low to be effective. We therefore asked whether propagating public 6-h LINCS drug-response profiles [22] through our inferred tumor and healthy subnetworks can prioritize candidate cross-cancer regimens. No clinical-trial outcomes, synergy screens, or resistance biomarkers were used as inputs.

To test basket-trial transfer in both directions, we moved standard LumA breast therapies, the CDK4/6 inhibitor *palbociclib*, the class-I PI3K inhibitor *pictilisib* (a proxy for *alpelisib*), and the mTORC1 inhibitor *everolimus* [62–64], into CIN colorectal cancer. We also moved the colorectal topoisomerase-I (TOP1) chemotherapies *irinotecan* and *topotecan* [65, 66] into LumA breast cancer (Figure 5; Table 1; Methods). Each standard therapy was paired with drugs from a 39-compound oncology pool and a 54-compound nuclear-receptor pool [67–69] under three constraints (Algorithm 2): (i) the two drugs have non-overlapping primary targets and do not both suppress the bone marrow; (ii) the combination engages the shared subnetwork at least as strongly as the standard therapy alone at full dose; and (iii) predicted disruption of the recipient organ's healthy network is no greater than with the standard therapy alone (≤ 1.00).

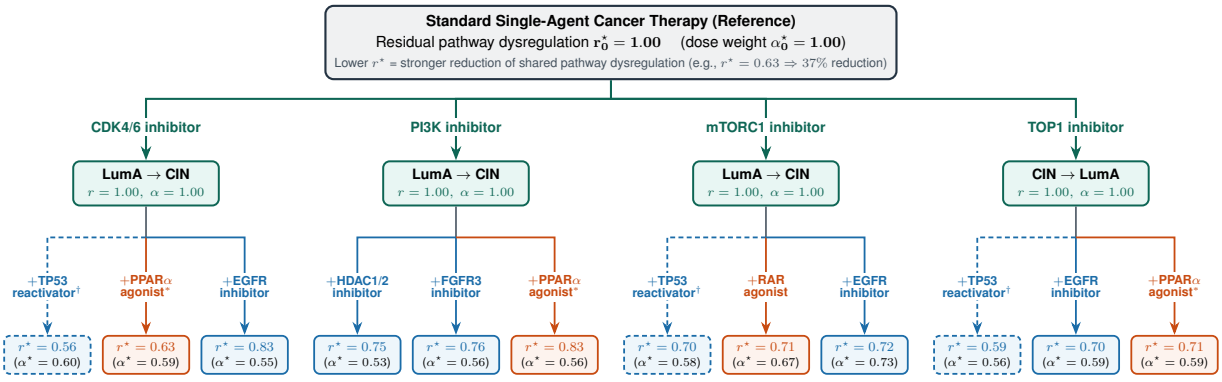


Figure 5: Decision tree of top-ranked combinations (Sections 2.7–2.8). Root, standard therapy alone. Level 1, standard LumA breast therapies (CDK4/6, PI3K, or mTORC1 inhibitors) applied to CIN colorectal cancer, and colorectal TOP1 chemotherapy applied to LumA breast cancer. Level 2, top partner classes: oncology drugs (solid blue, classes with clinical or preclinical precedent; dashed blue†, mutant-TP53 reactivator discussed in Section 2.8) and bone-marrow-sparing nuclear-receptor drugs (vermilion; *PPAR family, Section 2.5). Nodes show residual dysregulation $r^\star$ (1.00 = standard therapy alone) and backbone dose weight $\alpha^\star$ (Section 5.3.7). Drug-level scores in Table 1 and Table S7.

To score a combination, we compute $r^\star$, the shared tumor dysregulation that remains after treatment, relative to the standard therapy given alone. A value of $r^\star = 1.00$ means the partner adds nothing, and $r^\star = 0.70$ means the combination reverses 30% more of the shared tumor changes than the standard therapy alone. In practice, we predict how each drug's expression response propagates through the 107 shared tumor changes and measure how much of that dysregulation the

Table 1: **Top-ranked combinations for each standard therapy (Sections 2.7–2.8).** Columns: standard therapy and transfer direction; best oncology partners and best bone-marrow-sparing nuclear-receptor partners, with residual dysregulation $r^\star$ in parentheses (1.00 = standard therapy alone; Section 5.3.7); predicted disruption of the recipient organ's healthy network relative to the standard therapy alone (constrained to ≤ 1.00); and supporting clinical or preclinical evidence. *Eprenetapopt* is omitted (Section 2.8; Tables S7 and S11).

Backbone & Basket Transfer	**Oncology Partners ($r^\star$)**	**Novel Nuclear-Receptor Partners ($r^\star$)**	**Healthy Network Ratio**	**Clinical or Preclinical Precedent vs. Novel Hypothesis**
CDK4/6 inhibitor *palbociclib* LumA breast → CIN colon	**EGFR:** *erlotinib* (0.83), *gefitinib* (0.84) **FGFR1–3:** *infigratinib* (0.92)	**PPARα:** *gemfibrozil* (0.63), *fenofibrate* (0.76) **VDR:** *calcifediol* (0.75) **RAR:** *tretinoin* (0.79)	0.69–1.00	**Precedent:** Preclinical: FGFR1 or EGFR-family signaling linked to CDK4/6-inhibitor resistance in breast cancer [11, 70, 71]. Clinical: *palbociclib* + EGFR antibody *cetuximab* mixed in Phase II (single-arm activity in head and neck cancer [72]; primary endpoints not met in a randomized head and neck trial and in mCRC [73, 74]); CDK4/6 + FGFR only early-phase. **Novel:** PPARα fibrate/RAR + CDK4/6 in CRC; VDR context from Phase II SUNSHINE (primary PFS comparison not significant) [75].
PI3K inhibitor *pictilisib* (class-I PI3K proxy) LumA breast → CIN colon	**HDAC1/2:** *tacedinaline* (0.75) **FGFR3/VEGFR:** *dovitinib* (0.76), *infigratinib* (0.83) **JAK1/2:** *ruxolitinib* (0.80)	**PPARα:** *gemfibrozil* (0.83) **RAR:** *tretinoin* (0.85) **VDR:** *doxercalciferol* (0.87)	0.51–0.74	**Precedent:** Preclinical: PI3K–mTOR blockade relieves feedback and reactivates RTK signaling [10, 41]. Clinical: PI3K/mTOR + HDAC inhibition only in Phase I [76]; PI3K/mTOR + RTK inhibition modest or negative in Phase II [77, 78]. **Novel:** Nuclear-receptor co-targeting of R1/R2 *PPARD/RARG–PIK3CA* dysregulation in CRC.
mTORC1 inhibitor *everolimus* LumA breast → CIN colon	**EGFR/HER:** *gefitinib* (0.72), *neratinib* (0.94) **HDAC1/2:** *entinostat* (0.78) **FGFR3/KIT:** *masitinib* (0.90)	**RAR:** *tretinoin* (0.71) **PPARα:** *fenofibrate* (0.80) **VDR:** *calcifediol* (0.95)	0.80–1.00	**Precedent:** Preclinical: mTOR inhibition relieves feedback and reactivates RTK/AKT signaling [10]. Clinical: *everolimus* + RTK inhibitors modest or negative in Phase II (+ VEGFR inhibitor *tivozanib* in mCRC [77]; + *erlotinib* in lung cancer [78]) and Phase I with VEGFR inhibitors [79, 80]; mTOR + HDAC only Phase I [76]. **Novel:** Retinoid or fibrate + everolimus in CRC.
TOP1 chemotherapy *irinotecan* / *topotecan* CIN colon → LumA breast	**EGFR:** *gefitinib* (0.70) **JAK1/2:** *ruxolitinib* (0.70) **MET:** *tivantinib* (0.79), *crizotinib* (0.82–0.87) **VEGFR:** *linifanib* (0.79)	**PPARα:** *gemfibrozil* (0.71–0.77), *fenofibrate* (0.76) **VDR:** *doxercalciferol* (0.79), *calcifediol* (0.86) **RAR:** *tretinoin* (0.79)	0.70–0.97	**Precedent:** In mCRC, adding EGFR antibodies (Phase III and randomized Phase II [43, 44, 81]) or VEGF-pathway antibodies or aflibercept (Phase III [45, 46, 82]) to *irinotecan*-based chemotherapy improved outcomes; *irinotecan* + *cetuximab* is a standard control arm [83]. Untested in LumA breast cancer and with the small-molecule inhibitors nominated here. TOP1 + MET inhibitor *tivantinib* missed its randomized Phase II primary endpoint [84]; no TOP1 + JAK-inhibitor trials. **Novel:** Non-myelosuppressive PPARα/VDR/RAR + TOP1 regimens for LumA breast cancer.

combination leaves in place, compared with the standard therapy alone. The exact definition, and the optimization that chooses the dose of each drug, appear in Methods (Section 5.3.7; Algorithm 2); scores for every candidate are listed in Supplementary Table S7. Figure 5 shows the best-scoring partner classes for each standard therapy, and Table 1 lists the individual drugs and their scores.

The top-ranked oncology partners fall into combination classes with clinical or preclinical precedent, but the strength of that precedent varies widely (blue leaves in Figure 5; second and last columns of Table 1). First, the strongest precedent is for TOP1 chemotherapy with EGFR or VEGF-pathway inhibitors. In metastatic colorectal cancer, adding EGFR antibodies to *irinotecan*-based chemotherapy improved response rates or progression-free survival in randomized Phase II and Phase III trials [43, 44, 81], and adding VEGF-pathway antibodies or aflibercept improved overall survival in Phase III trials [45, 46, 82]. These trials tested antibodies in colorectal cancer, whereas our screen nominates small-molecule inhibitors (*gefitinib*, *linifanib*) with TOP1 chemotherapy for LumA breast cancer, where these combinations are untested. By contrast, adding the MET inhibitor *tivantinib* to *irinotecan* and *cetuximab* did not meet its primary endpoint in a randomized Phase II trial [84], and we found no trial of TOP1 chemotherapy with a JAK inhibitor. Second, EGFR or FGFR inhibitors added to the CDK4/6 inhibitor *palbociclib* target an escape route identified in preclinical studies [11, 70, 71]. Clinically, *palbociclib* plus the EGFR antibody *cetuximab* was active in a single-arm Phase II trial in head and neck cancer [72] but did not meet its primary endpoints in a randomized head and neck trial or in colorectal cancer [73, 74], and CDK4/6 plus FGFR inhibition has been tested only in early-phase trials. Third, HDAC or receptor tyrosine kinase inhibitors added to PI3K or mTOR inhibitors could counter the feedback reactivation of kinase signaling seen in preclinical studies [10]. However, mTOR plus HDAC inhibition has reached only Phase I [76], and mTOR plus receptor tyrosine kinase inhibition gave modest or negative results in Phase II [77, 78] after Phase I testing [79, 80]. For each standard therapy, the best of these partners reversed a further 17–30% of the shared tumor changes ($r^\star = 0.70$–0.83) while keeping predicted disruption of healthy tissue at 51–100% of the single-drug level.[4]

Recovering these combination classes suggests that the screen captures known resistance mechanisms. However, only the TOP1 combinations have positive Phase III evidence, and only in colorectal cancer. This motivates the search for gentler partners described next.

2.8 Nuclear-receptor drugs as partners for standard cancer therapies

The combinations above all add a second targeted or cytotoxic drug, and such pairs are often limited in patients by overlapping side effects such as low blood counts, diarrhea, and mucosal injury. This subsection asks whether gentler partners can do the same job. Because nuclear receptors are prominent upstream regulators in the shared subnetwork, we screened nuclear-receptor drugs, most of which do not suppress the bone marrow, as partners for the same four standard therapies.

Across all four standard therapies (*palbociclib*, *pictilisib*, *everolimus*, and *irinotecan*/*topotecan*), the screen of 54 nuclear-receptor drugs consistently favored three classes: PPARα agonists (fibrates), retinoic acid receptor (RAR) agonists, and vitamin D receptor (VDR) agonists (vermilion leaves in Figure 5; third column of Table 1). For each standard therapy, the best of these partners reversed a further 17–37% of the shared tumor changes ($r^\star = 0.63$–0.83) without increasing predicted disruption of the healthy tissue network. By drug, the fibrates *gemfibrozil* and *fenofibrate* scored $r^\star = 0.63$–0.83, the retinoid *tretinoin* 0.71–0.85, and the VDR agonists *calcifediol* and *doxercalciferol* 0.75–0.95 (per-therapy scores in Table 1). In our networks, these drugs act against the *PPARD/RARG* growth module identified above, and none was classed as bone-marrow suppressing in our screen. One such pairing has been tested clinically: in the randomized Phase II SUNSHINE trial in metastatic colorectal cancer, adding high-dose vitamin D_3 to standard chemotherapy did not significantly

[4]Per-drug scores ($r^\star$): *palbociclib* with *erlotinib* (0.83), *gefitinib* (0.84), or *infigratinib* (0.92); *pictilisib* or *everolimus* with *tacedinaline* (0.75), *entinostat* (0.78), *gefitinib* (0.72), or *dovitinib* (0.76); TOP1 chemotherapy with *gefitinib* (0.70), *ruxolitinib* (0.70), *tivantinib* (0.79), or *linifanib* (0.79). Clinical and preclinical evidence for each class is summarized in the last column of Table 1.

prolong progression-free survival in the primary comparison ($P = 0.07$), although an adjusted multivariable analysis favored vitamin D [75].

End-to-end sensitivity audits across regularization multipliers, sign thresholds, and cell-line backgrounds separated candidates sensitive to individual network links from robust drug classes (Tables S10 and S11). On the full shared subnetwork, the mutant-p53 reactivator *eprenetapopt* [85, 86] achieved the lowest raw score for five standard-therapy profiles ($r^\star = 0.56$–0.70; dashed blue leaves in Figure 5), but this rank depended on two *TP53* links that were inactive in both healthy cohorts. Restricting the screen to the 90 links supported across all four cohorts shifted the top oncology hits to *dovitinib* (0.76), *gefitinib* (0.74), and *vemurafenib* (0.74). Across every sensitivity perturbation, receptor tyrosine kinase and deacetylase inhibitors, as well as PPARα, RAR, and VDR agonists, remained enriched among top-ranked combinations.

Taken together, screening combinations under a safety bound on healthy tissue networks nominates two complementary classes of cross-cancer regimens built on standard breast and colorectal therapies. The first comprises targeted kinase and deacetylase combinations that block adaptive signaling feedback. The second comprises nuclear-receptor combinations, spanning fibrates, retinoids, and vitamin D analogs, that counter shared pathway dysregulation without adding a second bone-marrow-suppressing drug.

3 Discussion

We asked whether routine tumor and healthy-tissue biopsies, each of which captures a single moment, can be used to design drug combinations for basket trials. Ordering biopsies with a cell-cycle clock allowed us to reconstruct directed gene networks, find regulatory changes shared by breast and colorectal cancers, and rank drug combinations that reverse those changes while sparing healthy tissue. Below, we place these results in clinical context, compare the approach with existing computational methods, discuss the biology of the shared subnetwork and the drug classes it points to, explain why the method works on noisy patient data, and outline open questions, next steps, and limitations.

Basket trials have shown that a shared driver mutation does not guarantee the same benefit in every organ, because tissue-specific feedback can restore tumor growth [1, 7–9]. Our results suggest that routine tumor and healthy-tissue RNA-seq cohorts contain enough information to infer the direction of regulatory interactions once biopsies are ordered by a cell-cycle clock. The inferred networks predicted independent knockdown and pathway data better than random orderings, most clearly in colorectal tumors, although not every test passed; in particular, the networks did not predict the effects of broad chromosomal copy-number changes (Section 2.4). If confirmed experimentally, this approach would let basket-trial design match tumors by shared multi-gene pathway changes rather than by single-gene biomarkers.

Two features distinguish our approach from existing computational methods. First, it works with directed networks. Tools such as the Connectivity Map rank drugs by how well they reverse a list of altered genes [22], and co-expression networks cannot tell which gene drives which without additional structural assumptions [21]; we instead propagate each drug's predicted effect through directed tumor and healthy networks. Second, it builds safety into the ranking by requiring that a combination disrupt the healthy-tissue network no more than the standard therapy alone. As supporting evidence, although the screen used no clinical-trial, synergy, or resistance data, it ranked several combination classes with clinical or preclinical precedent highly. The strongest is TOP1 chemotherapy with EGFR or VEGF-pathway inhibition, which improved outcomes in Phase III trials in metastatic colorectal cancer [43–46] but is untested in the LumA breast setting our screen proposes. CDK4/6 with EGFR inhibition and mTOR with receptor tyrosine kinase inhibition reached Phase II with mixed or negative results [72–74, 77, 78]. PI3K or mTOR with HDAC inhibition has reached only Phase I [76], CDK4/6 with FGFR inhibition rests mainly on preclinical evidence [11], and TOP1 chemotherapy with MET inhibition did not meet its primary endpoint in a randomized Phase II trial [84]. Because our oncology pool was drawn from clinically developed

drugs, many of which have been combined in trials, this agreement shows that the rankings are clinically plausible; it does not by itself show that the screen outperforms chance.

Biologically, the changes shared by LumA breast and colorectal cancers center on the PPAR receptors, the only drug-target family that passed correction for multiple testing; Polycomb and DNA-methyltransferase regulators show weaker similarity (Section 2.5). This is plausible because both mammary ducts and colonic crypts use nuclear receptors and chromatin regulators to balance self-renewal against differentiation [38, 39, 59]. Within the shared subnetwork, PPARδ, RARγ, and ERRα gain activating links to *PIK3CA* and chromatin coactivators, and EZH2 represses the tumor suppressor *CYLD* (Section 2.6).

Our finding that PPARδ gains activating links to pro-growth genes in both tumor types fits a substantial body of experimental work, although that work has not been unanimous. PPARδ is elevated in human colorectal cancer and repressed by APC [87], and activating it accelerates intestinal and mammary tumors in mice [88–91]. Drug studies point the same way: in Apc-mutant mice, the PPARδ antagonist GSK3787 suppressed colorectal tumors, whereas the PPARδ agonist GW501516 accelerated them, and PPARδ raised levels of pro-growth and pro-invasive proteins, including AKT1, at the invasive front of human colorectal cancers [61]. Three earlier studies, however, found as many or more intestinal tumors in mice lacking PPARδ [92–94]. These studies deleted PPARδ from every cell from birth, which also alters metabolism and other processes throughout the body, whereas later studies that deleted it only in the intestinal lining found fewer tumors [61, 95]. On this basis, Liu and colleagues conclude that PPARδ promotes colorectal tumorigenesis, progression, and invasion [61]. Our screen did not include PPARδ antagonists, none of which is approved for clinical use, so testing whether directly blocking PPARδ adds to standard therapies is a natural follow-up.

The nuclear-receptor partners that the screen nominates are consistent with this subnetwork but are not fully explained by it. The screen ranks drugs by their measured expression responses in cell lines, propagated through the inferred networks, rather than by the receptors they target, and two of the top classes raise mechanistic questions. Pan-RAR agonists such as *tretinoin* activate RARγ, which gains pro-growth links in our networks, as well as RARβ, which here activates growth-restraining genes (*PTEN*, *CYLD*, *NCOR2*; Section 2.6). Their predicted benefit may reflect the net balance of these two branches. Similarly, it is not established that activating PPARα counteracts changes linked to PPARδ, although PPARα activators are known to suppress the angiogenic receptor VEGFR-2 [55]. These mechanisms should be tested directly rather than assumed. For vitamin D receptor agonists, a randomized Phase II trial of adding vitamin D to colorectal chemotherapy was encouraging but did not reach significance in its primary comparison [75].

Two design choices help the method cope with noisy patient data. First, comparing biopsies about one-sixth of a cycle apart, rather than immediate neighbors, averages out small errors in the clock ordering, and differences in how fast cells move through the cycle reduce to a single scale factor that disappears when each network is rescaled (Section 5.3.4; Supplementary Section S1). Second, the sparsity penalty selects a small number of hub regulators, matching the known hub structure of transcriptional networks [48, 49, 96]. It also leaves each gene's own turnover unpenalized, so that the turnover terms absorb differences in baseline expression between patients. For slowly dividing tissues, or under treatments that suppress cell-cycle genes [97], the same framework could use other progression markers in place of the cell-cycle clock.

Several questions remain about how far these results extend. We analyzed one molecular subtype of each cancer, so it is not known whether other breast and colorectal subtypes, or other cancer types, share the same subnetwork. The drug scores rest on 6-h, single-dose cell-line responses, so they do not capture dosing schedules, drug exposure in patients, or interactions between the two drugs in a combination; any nominated regimen would need standard dose-finding and safety evaluation.

The most direct next step is to test the top combinations in patient-derived breast and colorectal tumor organoids alongside matched healthy mammary and colonic organoids. Such experiments would check both predictions at once: that each combination slows tumor growth more than the

standard therapy alone, and that it spares healthy epithelium. Combinations that pass could then move into window-of-opportunity or basket trials. More broadly, our results suggest that public tumor and healthy-tissue cohorts, ordered by a cell-cycle clock, can help prioritize which drug combinations are worth testing in basket trials.

3.1 Limitations

Several limitations affect how these findings should be interpreted. First, bulk biopsies mix tumor cells with fibroblasts, blood vessels, and immune cells [98, 99]. Even after adjusting for cell-type markers, the inferred links describe whole-tissue interactions. Indeed, 32 of the 107 shared links involve vascular, cytokine, or immune-checkpoint receptors (such as *KDR* and *CD274*; Figure 4) and likely reflect cross-talk between tumor cells and their microenvironment. Second, to compare fast-dividing colon with slower-dividing breast tissue, the cross-cancer comparison uses interaction signs rather than strengths and does not model multi-step feedback loops. Third, the inferred links are statistical associations and do not by themselves establish whether a regulator such as PPARδ promotes or restrains tumor growth (Section 3).

Fourth, inference was limited to a 100-gene panel in cohorts with different mutation profiles. For example, *TP53* is mutated far more often in CIN colorectal than in LumA breast cancer [13, 14, 100]. As a result, the high rank of the mutant-p53 reactivator *eprenetapopt* rested on a few sparse *TP53* links, which disappeared when we kept only links active in all four cohorts (Table S11). Fifth, the healthy-tissue cohorts are smaller than the tumor cohorts, which increases sampling noise, and drug responses come from 6-h treatments of established cell lines (MCF7 and HT29) rather than patient tissue. As a result, permutation p-values for individual drug rankings are modest (≥ 0.061 across the 19–54 candidate drugs per pool; Tables S7 and S11). Experimental validation in matched tumor and healthy organoids and in animal models is therefore needed before clinical use.

4 Data and code availability

- All transcriptomic, copy-number, perturbation, and chemical-biology datasets analyzed in this study are publicly available from existing repositories. Accession numbers and web portals are listed in the Data sources and software table (Methods): UCSC Xena Toil RNA-seq recompute hub (`https://xenabrowser.net/datapages/`) [17], cBioPortal TCGA PanCancer Atlas (`https://www.cbioportal.org/`) [101–103], U2OS FUCCI scRNA-seq (GEO: GSE146773) [31], human iPSC FUCCI scRNA-seq (GEO: GSE121265) [30], LINCS L1000 shRNA and compound signatures (GEO: GSE92742) [22], OmniPath [52, 53], CollecTRI [54], ChEMBL release 37 [67], WHO ATC [68], NLM MeSH 2026 [69], and HGNC [104].
- Self-contained Python packages and replication notebooks implementing data preparation, clock training, ADMM network estimation, extraction of shared subnetworks, and combination ranking accompany this manuscript.
- This study did not generate new wet-lab reagents or biological materials.
- Any additional information required to reanalyze the data reported in this paper is available from the authors upon request.

5 Methods

5.1 Data sources and software

Resource	Source	Identifier
Deposited data		
Human U2OS FUCCI scRNA-seq (1,146 cells)	Mahdessian et al. [31]	GEO: GSE146773
Human iPSC FUCCI scRNA-seq (888 cells, 6 donors)	Hsiao et al. [30]	GEO: GSE121265
TCGA & GTEx Toil bulk RNA-seq ($\log_2(\mathrm{TPM}+1)$, GENCODE v23)	Goldman et al. [17]	https://xenabrowser.net/datapages/
TCGA PanCancer Atlas clinical subtypes (BRCA LumA, COAD/READ CIN) & GISTIC2 copy-number calls	Cerami et al. [101]; Hoadley et al. [103]; Liu et al. [105]	https://www.cbioportal.org/; GDC PanCanAtlas
LINCS L1000 Level 5 consensus 96-h shRNA & 6-h compound signatures (MCF7, HT29, SW480)	Subramanian et al. [22]	GEO: GSE92742
OmniPath curated directed signaling interactions	Türei et al. [52, 53]	https://omnipathdb.org/
CollecTRI curated transcription-factor regulons	Müller-Dott et al. [54]	https://github.com/saezlab/CollecTRI
ChEMBL small-molecule mechanisms, targets, & trial phases	Zdrazil et al. [67]	ChEMBL release 37 (https://www.ebi.ac.uk/chembl/)
WHO Anatomical Therapeutic Chemical (ATC) index, NLM MeSH 2026, & HGNC gene nomenclature	WHO [68]; NLM [69]; Seal et al. [104]	https://atcddd.fhi.no/; https://meshb.nlm.nih.gov/; https://www.genenames.org/
Software and algorithms		
Python scientific stack	Python Software Foundation	Python 3.13; NumPy 2.3.5; SciPy 1.17.1; pandas 2.3.3; scikit-learn 1.8.0
Convex optimization & serialization libraries	Diamond & Boyd; community packages	cvxpy 1.8.2 (CLARABEL 0.11.1, OSQP 1.1.1, SCS 3.2.11); pyarrow 23.0.1; h5py 3.14.0; xarray 2026.9.0; matplotlib 3.10.7
Clock-ordered ADMM network reconstruction & drug-combination solver	This paper	Included with manuscript

5.2 Datasets and cohorts

All human tissue and single-cell analyses used de-identified, publicly available cohorts requiring no new participant recruitment. Bulk RNA-seq cohorts ($\log_2(\mathrm{TPM}+1)$, GENCODE v23) of untreated primary (TCGA sample code 01) Luminal A breast adenocarcinoma ($n = 498$) and chromosomally unstable colorectal adenocarcinoma ($n = 245$) were assembled from the UCSC Xena Toil recompute hub [17] using cBioPortal TCGA PanCancer Atlas subtype classifications [36, 37, 101–103, 105]. Tissue-matched non-malignant breast ($n = 217$: 96 TCGA adjacent-normal plus 121 GTEx mammary samples) and colon ($n = 91$: 43 TCGA adjacent-normal plus 48 GTEx transverse/sigmoid colon samples) cohorts retained GTEx samples [15, 16] only if their epithelial marker mean was at least the 10th percentile, and their adipose (breast) or smooth-muscle (colon) marker mean at most the 90th percentile, of the corresponding TCGA adjacent-normal cohort. Single-cell clock training and cross-lineage validation used 1,146 human U2OS osteosarcoma cells with paired scRNA-seq and FACS FUCCI pseudotime (0–25.4 h; GEO: GSE146773) [31] and 888 quality-controlled human iPSCs from six donors with microscopy-derived FUCCI phases $\tau \in [0, 2\pi)$ (GEO: GSE121265) [30]. Perturbation analyses used LINCS L1000 Level 5 consensus signatures in human MCF7 breast and HT29/SW480 colorectal carcinoma lines (GEO: GSE92742) [22].

5.3 Computational methods

5.3.1 Gene panel selection and bulk tissue composition adjustment

To balance pathway coverage with identifiability at clinical cohort sizes ($n = 91$–498), we selected a targeted 100-gene bulk panel ($p = 100$) nested within a 200-gene candidate pool (Table S8). Selection required HGNC-approved protein-coding status [104], $\geq 80\%$ non-missing coverage across TCGA/GTEx/cBioPortal, median expression ≥ 0.5 TPM in all four bulk cohorts, and zero

overlap with the 11 cell-cycle clock genes. The 100-gene bulk panel comprises all 29 expressed human nuclear hormone receptors [35], 45 shared breast and colorectal cancer drivers and clinical biomarkers [13, 14, 103, 105], and 26 additional targets of FDA/EMA-approved drugs (ChEMBL max_phase = 4) [33, 34, 67, 68]. The +100 extended pool adds 59 OmniPath directed signaling intermediates, 27 clinical-stage targets (max_phase ≥ 2), and 14 channel/transporter/cytokine genes (157 of 200 expressed in $\geq 50\%$ of U2OS cells). Within each bulk cohort, expression was linearly regressed on four coarse cell-type marker means: epithelial (*EPCAM, KRT8, KRT18, KRT19, CDH1*), adipose (*ADIPOQ, PLIN1, FABP4, LEP, LPL* in breast) or smooth muscle (*ACTA2, MYH11, TAGLN, CNN1, DES* in colon), stromal (*COL1A1, COL1A2, COL3A1, FN1, DCN, VIM*), and pan-immune (*PTPRC, CD3D, CD68*), plus a batch indicator (GTEx versus TCGA) in pooled normal cohorts. Cohort means were then added back to the residuals before each tumor–healthy pair was standardized by its pooled mean and SD.

5.3.2 Bayesian two-harmonic Fourier cell-cycle clock

To infer circular cell-cycle phase $\tau \in [0, 2\pi)$ from static transcriptomes, we modeled rank-based inverse-normal transformed expression z_g of each of the $d = 11$ canonical cell-cycle markers (*CCND1, CCND2, CCND3, CCNE1, CCNE2, CCNA2, CCNB1, CCNB2, CDK1, UBE2C, TOP2A*) as conditionally Gaussian given phase, $z_g \mid \tau \sim \mathcal{N}(\mu_g(\tau), \sigma_g^2)$, where $\tau = 2\pi t / T_{\text{cyc}}$ ($T_{\text{cyc}} =$ 25.4 h in U2OS) [31]. Each periodic curve $\mu_g(\tau)$ was fitted by ridge-regularized second-order Fourier regression on $[\cos\tau, \sin\tau, \cos 2\tau, \sin 2\tau]$ ($\alpha_{\text{ridge}} = 10^{-2}$ on harmonic coefficients, unpenalized intercept, residual SD floor $\sigma_{\min} = 0.05$). Marker likelihoods, tempered by a 5-fold cross-validated likelihood temperature β, were combined with a von Mises kernel density prior $p(\tau)$ ($\kappa_{\text{prior}} = 4.0$) over a 254-point phase grid to yield the posterior density $p(\tau \mid z) \propto p(\tau) \prod_{g=1}^{d} \mathcal{N}(z_g \mid \mu_g(\tau), \sigma_g^2)^{\beta}$. The circular mean of this posterior gives the phase estimate $\hat{\tau}_i$. After out-of-sample U2OS validation and transfer to iPSCs without retraining, the clock was frozen on all 1,146 U2OS cells and applied to rank-normalized, composition-adjusted bulk cohorts to obtain phases $\theta_i \in [0, 2\pi)$ (unwrapped by 2π per cycle when modeling linear progression time).

5.3.3 Ornstein–Uhlenbeck dynamical model with shared and private variance

We model unordered expression snapshots as samples of an Ornstein–Uhlenbeck (OU) system with shared and private components, paired with an exogenous approximate clock (complete error constants and proofs in Supplementary Section S1).

Definition 1 (Ornstein–Uhlenbeck process with shared and private components)**.** Consider a p-dimensional linear OU system

$$dx_t = Bx_t\,dt + A\,dW_t, \tag{1}$$

where $x_t \in \mathbb{R}^p$ is the centered gene-expression state, $B \in \mathbb{R}^{p\times p}$ is a Hurwitz-stable drift matrix ($\max_{1\leq i\leq p} \operatorname{Re}\lambda_i(B) < 0$) whose off-diagonal entry B_{ij} is the direct linear rate at which regulator j drives target i and whose diagonal $B_{jj} < 0$ captures intrinsic mRNA degradation and homeostatic self-damping, $A \in \mathbb{R}^{p\times p}$ is the diffusivity matrix, W_t is standard p-dimensional Brownian motion, and $\Sigma \succ 0$ is the stationary covariance solving the continuous-time Lyapunov equation

$$B\Sigma + \Sigma B^{\top} = -AA^{\top}. \tag{2}$$

We observe $n \geq 3$ cross-sectional snapshots $z_i := x^i_{t_i} \in \mathbb{R}^p$ at unknown progression times $0 \leq t_1 < t_2 < \cdots < t_n$. Each sample trajectory evolves as $dx^i_t = Bx^i_t\,dt + A\,dW^i_t$ with initial state $x^i_0 = \sqrt{\rho}\,z^0 + \sqrt{1-\rho}\,\tilde{z}^i$ and Brownian motion $W^i_t = \sqrt{\rho}\,W^0_t + \sqrt{1-\rho}\,\tilde{W}^i_t$, where $\rho \in [0,1]$ is the shared progression variance fraction, $W^0, \tilde{W}^1, \ldots, \tilde{W}^n$ are independent Brownian motions, and $z^0, \tilde{z}^1, \ldots, \tilde{z}^n \sim \mathcal{N}(0, \Sigma)$ are independent stationary initial states, giving marginal covariance $\Sigma = \rho\Sigma + (1-\rho)\Sigma$.

From unordered snapshots alone, only the static sample covariance $S = \frac{1}{n-1}\sum_{i=1}^{n}(z_i - \bar{z})(z_i - \bar{z})^\top \approx \Sigma$ is observable. The skew-symmetric commutator $B\Sigma - \Sigma B^\top$, and hence asymmetric B, therefore remains unidentifiable without additional structural assumptions [21].

Definition 2 (Approximate clock and lag-ℓ summary matrices)**.** An *approximate clock* is an exogenous scalar vector $\tau = (\tau_1, \ldots, \tau_n) \in \mathbb{R}^n$ with distinct entries that increases on average with t and is conditionally independent of expression trajectories given t. Canonically, $\tau_i = \tau(t_i)$ is generated by the drift-diffusion process

$$d\tau(t) = v\, dt + \varepsilon\, dW'_t \qquad (v > 0,\ \varepsilon > 0). \tag{3}$$

Let π sort τ in ascending order ($\theta_k := \tau_{\pi(k)}$, $\theta_1 < \cdots < \theta_n$), and let $w_k := z_{\pi(k)} - \bar{z}$ ($\bar{z} = \frac{1}{n}\sum_{i=1}^{n} z_i$). For macroscopic index lag $\ell \in \{1, \ldots, n-2\}$, $N := n - \ell$ pairs, and mean clock step $\Delta := \frac{1}{N}\sum_{k=1}^{N}(\theta_{k+\ell} - \theta_k) > 0$, define the static covariance S, symmetric difference covariance D, and antisymmetric lead–lag covariance J:

$$\begin{aligned} S &= \frac{1}{n-1}\sum_{k=1}^{n} w_k w_k^\top, \qquad D = \frac{1}{\Delta N}\sum_{k=1}^{N}(w_{k+\ell} - w_k)(w_{k+\ell} - w_k)^\top, \\ J &= \frac{1}{\Delta N}\sum_{k=1}^{N}\left(w_{k+\ell} w_k^\top - w_k w_{k+\ell}^\top\right). \end{aligned} \tag{4}$$

5.3.4 Clock-ordered network reconstruction with group sparsity and ADMM solver (Algorithm 1)

Given snapshots $Z \in \mathbb{R}^{n\times p}$ sorted by clock phases θ, we select the index lag ℓ whose mean phase step Δ is closest to 1 rad. We then form $S_{\text{in}} = S + \eta_{\text{ridge}} I$ ($\eta_{\text{ridge}} = 10^{-3}\,\text{tr}(S)/p$ in bulk tissues; 0 in low-dimensional simulations), D, and J via Eq. (4). Algorithm 1 estimates $\hat{B}$ by penalizing off-diagonal regulator columns $B_{-j,j} \in \mathbb{R}^{p-1}$ while leaving self-damping diagonals B_{jj} unpenalized.

Algorithm 1 Clock-ordered dynamical system reconstruction

Input: Snapshot matrix $Z \in \mathbb{R}^{n\times p}$; approximate clock values $\tau \in \mathbb{R}^n$ ($\max_i \tau_i > \min_i \tau_i$); macroscopic index lag $\ell \in \{1, \ldots, n-2\}$; regularization parameters $\lambda, r > 0$ (using conditioned S_{in} in place of S in bulk cohorts)

Output: Reconstructed directed interaction matrix $\hat{B} \in \mathbb{R}^{p\times p}$

1: *Order snapshots:* Sort Z by τ via permutation π ($\theta_1 \le \cdots \le \theta_n$) and center $w_k = z_{\pi(k)} - \bar{z}$.

2: *Compute lag-ℓ matrices:* Form S (or S_{in}), D, and J at lag ℓ via Eq. (4).

3: *Solve strongly convex column-group program:*

$$\hat{B} \leftarrow \arg\min_{B\in\mathbb{R}^{p\times p}} \sum_{j=1}^{p} \|B_{-j,j}\|_2 + \frac{1}{\lambda}\left\|BS + SB^\top + D\right\|_F^2 + \frac{1}{r\lambda}\left\|BS - SB^\top - J\right\|_F^2. \tag{5}$$

4: **return** $\hat{B}$

The antisymmetric weight $r = r_{\text{null}} := \overline{\|J_b\|_F^2}\,/\,\overline{\|D_b - \bar{D}_{\text{rand}}\|_F^2}$ equalizes the Frobenius dispersion of null residuals across R uniform random sample permutations ($R = 1{,}000$ in bulk cohorts, where $\mathbb{E}[J_b \mid Z] = 0$ and $\bar{D}_{\text{rand}} = \frac{2}{\Delta} S$ by Proposition S2 in Supplementary Section S1). From the unpenalized ($\lambda \to 0$) solution $B_{\text{unpen}} = \frac{1}{2}(J - D)S_{\text{in}}^{-1}$ solving the coupled balance equations

$$XS + SX^\top = -D, \qquad XS - SX^\top = J, \tag{6}$$

we set $\lambda = c_{\text{mult}}\, s_{\text{unpen}}(S_{\text{in}}, D, J, r_{\text{null}})$ at default $c_{\text{mult}} = 1.0$ (sensitivity across $c_{\text{mult}} \in \{0.5, 1.0, 1.5, 2.0, 2.5\}$ in Table S10), where

$$s_{\text{unpen}}(S_{\text{in}}, D, J, r_{\text{null}}) = 4\left(1 + r_{\text{null}}^{-1}\right)\left(\text{median}_{1\le i\le p}\,\lambda_i(S_{\text{in}})\right)^2 \text{median}_{1\le j\le p}\,\|B_{\text{unpen},-j,j}\|_2. \tag{7}$$

By Proposition S1 (Supplementary Section S1), Eq. (5) is strongly convex with a unique global minimizer that is scale-equivariant with respect to Δ. We solve Eq. (5) via the alternating direction method of multipliers (ADMM) in the eigenbasis $S_{\text{in}} = Q\Lambda Q^\top$, splitting B and $\tilde{B} = Q^\top BQ$. Each iteration uses $O(p^2)$ closed-form 2×2 updates per pair $(\tilde{B}_{ab}, \tilde{B}_{ba})$ and column-wise off-diagonal block soft-thresholding on B, with adaptive residual balancing to a relative primal/dual tolerance of 10^{-5}. Theorems 1 and 2 summarize population identifiability (complete non-uniform progression bounds and proofs in Supplementary Section S1).

Theorem 1 (Informal: Expected lag covariances and cancellation of private variance; complete statement in Supplementary Section S1)**.** *Evaluated on the approximate clock at lag ℓ, $\mathbb{E}[D \mid t, \tau]$ and $\mathbb{E}[J \mid t, \tau]$ recover $-(B\Sigma + \Sigma B^\top)$ and $B\Sigma - \Sigma B^\top$ up to shared positive scale $s = \rho\bar{h}/\Delta$ (for mean true time lag $\bar{h}$), plus a bias from private variance $\frac{2(1-\rho)}{\Delta}\Sigma$ in $\mathbb{E}[D]$ only (canceling identically in $\mathbb{E}[J]$), plus error matrices. These error matrices are bounded by an exponentially decaying term from clock ordering inversions in $\text{SNR} = v^2\delta t/\varepsilon^2$, a finite-step Taylor term proportional to $\overline{h^2}/\bar{h}$, and an $O(1/N)$ mean-centering term in $\mathbb{E}[J]$.*

Theorem 2 (Informal: Off-diagonal sign recovery up to cohort scale; complete statement in Supplementary Section S1)**.** *For $S \succ 0$, symmetric D, and antisymmetric J, Eq. (6) has unique closed-form solution $X = \frac{1}{2}(J - D)S^{-1}$, which is Hurwitz stable whenever $D \succ 0$. For $\rho \in (0, 1]$, evaluating at $S = \Sigma$ and $(D, J) = (\mathbb{E}[D \mid t, \tau], \mathbb{E}[J \mid t, \tau])$ yields $X = s(B - \mu I) + E$ with $s = \rho\bar{h}/\Delta > 0$ and diagonal shift $\mu = \frac{1-\rho}{\rho h} \geq 0$ (this shift likewise affects only the unpenalized diagonal of $\hat{B}$; Remark S2 in Supplementary Section S1). Here $\|E\|_F/s$ vanishes as clock SNR grows, lag step shrinks, and total time span increases, so the off-diagonal entries and signs of B are recovered up to scale s.*

5.3.5 Synthetic and single-cell pseudo-bulk benchmark protocols

In Benchmark 1 (Figure S1; Tables S1 and S2), a 10-gene stochastic system comprising a 2-gene nonlinear limit-cycle oscillator (speed parameter $a \in \{0, 0.9\}$, instantaneous speed $\propto 1 + a\sin\theta$) driving an 8-gene linear network B ($\sigma \in \{0.03, 0.1, 0.3\}$, $n \in \{91, 171, 245, 1{,}000\}$) was simulated across 20 seeds per regime with Gaussian clock error $\sigma_{\text{clock}} = 0.45$ rad. Of these regimes, 12 single-cell regimes sampled individual trajectories, and 9 bulk regimes ($a = 0.9, \sigma = 0.1$) pooled 100 cells per biopsy with circular phase spread 0.3, 1.0, or 2.0 rad under shared sample-level noise. Results were benchmarked against 20 random orderings per seed. In Benchmark 3 (Figure 2F; Table S3), across 10 random U2OS splits (holding out 287 cells per split as in Benchmark 2), the 859 remaining cells were split into 429 clock-training cells and 430 test cells; a de novo 11-gene clock then ordered $n \in \{91, 171, 245\}$ 100-cell pseudo-bulk samples (spread 0.3 or 1.0 rad). Reconstructions were evaluated against the unpooled 430-cell reference network B_{sc}, ordered by measured FUCCI time, on the 20 strongest cycle-phase genes and on 100 stratified 20-gene subsets of the 157 U2OS-expressed candidate genes, and were benchmarked against 100 random orderings per split.

5.3.6 Scale-invariant sign shifts and shared subnetwork extraction

To eliminate cohort-specific scale factors s_g and diagonal shifts (Theorem 2; Corollary S1 and Remark S3 in Supplementary Section S1), each bulk fit $\hat{B}_g$ was normalized by its off-diagonal Frobenius norm:

$$\tilde{B}_g := \frac{\hat{B}_g}{\|\text{offdiag}(\hat{B}_g)\|_F}. \tag{8}$$

For tissue $g \in \{t, h\}$ in cancer $c \in \{\text{LumA}, \text{CIN}\}$, we formed the zero-diagonal thresholded sign matrix $S^{(c)}_{g,ij} := \text{sign}_{\epsilon^{(c)}}(\tilde{B}^{(c)}_{g,ij})$ $(i \neq j)$ at primary cutoff $\epsilon^{(c)} = 2.0\, m^{(c)}_h$ (where $m^{(c)}_h = \text{median}_{i \neq j,\, \tilde{B}^{(c)}_{h,ij} \neq 0} |\tilde{B}^{(c)}_{h,ij}|$; sensitivity across $\{1.5, 2.0, 2.5\}\, m^{(c)}_h$ in Table S5) and the directional

sign shift between tumor and healthy networks

$$\operatorname{sign}_\epsilon(z) := \begin{cases} +\frac{1}{2}, & z > \epsilon, \\ 0, & |z| \le \epsilon, \\ -\frac{1}{2}, & z < -\epsilon, \end{cases} \qquad \chi_{ij}^{(c)} := S_{t,ij}^{(c)} - S_{h,ij}^{(c)} \in \left\{-1, -\tfrac{1}{2}, 0, +\tfrac{1}{2}, +1\right\} \quad (i \neq j). \tag{9}$$

The bicluster union $\mathcal{U}$ and the 107-link shared subnetwork were defined by three rounds of alternating 8×8 biclustering ($k_{\text{rect}} = 8$, down-weighting selected entries by $\gamma_{\text{rect}} = 0.5$ per round; sensitivity across $k_{\text{rect}} \in \{3, 5, 8\}$ in Table S5) on the positive concordance $K_{ij} = \chi_{ij}^{(\text{LumA})}\chi_{ij}^{(\text{CIN})}\mathbb{I}(\chi_{ij}^{(\text{LumA})}\chi_{ij}^{(\text{CIN})} > 0)$:

$$\Delta B_{\text{rect},ij} := \begin{cases} \frac{1}{2}\left(\chi_{ij}^{(\text{LumA})} + \chi_{ij}^{(\text{CIN})}\right), & (i,j) \in \mathcal{U} \text{ and } \chi_{ij}^{(\text{LumA})}\chi_{ij}^{(\text{CIN})} > 0, \\ 0, & \text{otherwise.} \end{cases} \tag{10}$$

5.3.7 Constrained optimization of drug combinations (Algorithm 2)

Six standard backbones R (*palbociclib, pictilisib, everolimus, irinotecan, active metabolite of irinotecan*, and *topotecan*) were represented by 6-h L1000 Level 5 vectors $u_R \in \mathbb{R}^{100}$ (averaged across MCF7 and HT29 when both were assayed [22]). Each backbone was paired with candidates $e \in \mathcal{F}(R)$ from the 39-compound oncology pool or the 54-compound nuclear-receptor repurposing pool, excluding pairs with overlapping panel targets or dual myelosuppressive mechanisms across *TOP1, DNMT3A, HDAC1/2, CDK4/6, KIT*. With $(\alpha_0, c_0, \gamma) = (0.4, 0.05, 1.0)$, Algorithm 2 solves the constrained combination problem exactly by a 1D ray search over $q = c_e/\alpha \in [c_0, 1]$ on a 1,901-point grid.

Algorithm 2 Constrained ranking of drug combinations on the shared subnetwork

Input: Shared subnetwork ΔB_{rect}; healthy sign network of the recipient organ $S_h^{(2)}$; backbone vector $u_R \in \mathbb{R}^p$; compatible partner pool $\mathcal{F}(R)$ with vectors $\{u_e\}_{e\in\mathcal{F}(R)}$; bounds $0 < c_0 \le \alpha_0 \le 1$ and $\gamma > 0$

Output: Feasible candidate drugs $(e, \alpha^\star, c_e^\star)$ ranked by residual activity $r^\star$ on ΔB_{rect}

1: Set baselines $\tau_R \leftarrow \||\Delta B_{\text{rect}}|\,|u_R|\|_2$ and $h_R \leftarrow \|S_h^{(2)}u_R\|_2$; rescale $\tilde{u}_e \leftarrow (\tau_R/\tau_e)\,u_e$ where $\tau_e \leftarrow \||\Delta B_{\text{rect}}|\,|u_e|\|_2$ (entrywise $|\cdot|$).

2: **for** each candidate drug $e \in \mathcal{F}(R)$ **do**

3: Solve over backbone weight $\alpha \in [\alpha_0, 1]$ and partner weight $c_e \in [c_0, \alpha]$:

$$\min_{\alpha\in[\alpha_0,1],\, c_e\in[c_0,\alpha]} \left\|\Delta B_{\text{rect}}(\alpha u_R + c_e\tilde{u}_e)\right\|_2 \quad \text{s.t.} \quad \begin{cases} \left\||\Delta B_{\text{rect}}|\,|\alpha u_R + c_e\tilde{u}_e|\right\|_2 \ge \tau_R, \\ \left\|S_h^{(2)}(\alpha u_R + c_e\tilde{u}_e)\right\|_2 \le \gamma\, h_R, \end{cases} \tag{11}$$

by exploiting positive homogeneity ($c_e = q\alpha$): set $\alpha^\star(q) = \alpha_{\min}(q)$ for each feasible $q \in [c_0, 1]$, i.e., each q with $\alpha_{\min}(q) \le \alpha_{\max}(q)$, where

$$\alpha_{\min}(q) := \max\left(\alpha_0,\, \frac{c_0}{q},\, \frac{\tau_R}{\||\Delta B_{\text{rect}}|\,|u_R + q\tilde{u}_e|\|_2}\right), \; \alpha_{\max}(q) := \min\left(1,\, \frac{\gamma\, h_R}{\|S_h^{(2)}(u_R + q\tilde{u}_e)\|_2}\right). \tag{12}$$

4: **end for**

5: **return** Candidates ranked in ascending order of $r^\star(R, e) = \|\Delta B_{\text{rect}}(\alpha^\star u_R + c_e^\star\tilde{u}_e)\|_2/\|\Delta B_{\text{rect}}u_R\|_2$.

5.4 Statistical analysis

All statistical tests, cohort sizes (n), and dispersion metrics are reported in the Results, figure legends, and Tables S1–S11. All analyses used fixed pseudorandom seeds and input tables. Single-

cell clock accuracy was evaluated on 20 random 75%/25% U2OS splits ($n = 287$ test cells/split) and on $n = 888$ iPSCs, and was benchmarked against 1,000 clocks fit to shuffled phases. Bulk cohort reconstructions ($n = 498$ LumA, $n = 245$ CIN, $n = 217$ healthy breast, $n = 91$ healthy colon) were benchmarked against $R = 1{,}000$ uniform random sample permutations ($p = \text{rank}/(R+1)$, pre-declared benchmark threshold $p \leq 0.10$) across 42 external tests (Figure 3; Table S4). These tests were (1) lag-1 autocorrelation across the 93 non-clock assayed panel genes ($p \leq 0.05$ count and 40-sample circular running means); (2) mean zero-centered Spearman correlation between predicted steady-state knockdown responses $(\hat{B}_g^{-1})_{\cdot,j}$ (unit push $u = -e_j$) and 96-h L1000 shRNA z-scores in MCF7 or pooled HT29/SW480 across 24 directly measured landmark genes (primary) and all 93 assayed panel genes (secondary); (3) trans-chromosomal GISTIC2 copy-number dosage responses; and (4) sign agreement with curated links in OmniPath, supported CollecTRI, full CollecTRI, and high-coverage targets ($\geq 20\%$ of known upstream regulators on the 100-gene panel), computed on non-zero fitted links (nz) and with zeros counted as wrong (zw). Cross-cancer conservation was tested against 1,000 simultaneous row/column gene-label permutations of the CIN network. Tests were run across the 20 druggable mechanism families [33, 34] using Pearson correlation r_G and mean shift product $\mu_{\text{LumA}}\mu_{\text{CIN}}$ on the $99|G|$-dimensional outgoing profile $\Delta\tilde{B}^{(c)}_{\cdot,G} = \tilde{B}^{(c)}_{t,\cdot,G} - \tilde{B}^{(c)}_{h,\cdot,G}$ with Benjamini–Hochberg FDR_{20} and FDR_{22} control (Table S6), and across all 9,900 off-diagonal gene pairs and the 3,960 links among the 40 regulators active in all four cohorts (Table S5). Top combination scores $r^\star$ were audited against 1,000 network gene-label permutations (p_{net}), 1,000 shared (p_{push}) and independent ($p_{\text{push,ind}}$) permutations of partner drug signatures, the subset of 90 links active across all four cohorts, MCF7-only versus HT29-only pushes, $\epsilon \in \{1.5, 2.0, 2.5\}\, m_h$, $k_{\text{rect}} \in \{3, 5, 8\}$, and $c_{\text{mult}} \in \{0.5, \ldots, 2.5\}$ (Tables S10 and S11).

References

[1] Brian P. Hobbs, Roberto Carmagnani Pestana, Emily C. Zabor, Alexander M. Kaizer, and David S. Hong. Basket trials: Review of current practice and innovations for future trials. *Journal of Clinical Oncology*, 40:3520–3528, 2022. doi: 10.1200/JCO.21.02285.

[2] Vivek Subbiah, Howard A. Burris, III, and Razelle Kurzrock. Revolutionizing cancer drug development: Harnessing the potential of basket trials. *Cancer*, 130:186–200, 2024. doi: 10.1002/cncr.35085.

[3] Peter J. O'Dwyer, Robert J. Gray, Keith T. Flaherty, Alice P. Chen, Shuli Li, Victoria Wang, Lisa M. McShane, David R. Patton, James V. Tricoli, P. Mickey Williams, A. John Iafrate, Jeffrey Sklar, Edith P. Mitchell, Naoko Takebe, David J. Sims, Brent Coffey, Tony Fu, Mark Routbort, Larry V. Rubinstein, Richard F. Little, Carlos L. Arteaga, Donna Marinucci, Stanley R. Hamilton, Barbara A. Conley, Lyndsay N. Harris, and James H. Doroshow. The NCI-MATCH trial: lessons for precision oncology. *Nature Medicine*, 29:1349–1357, 2023. doi: 10.1038/s41591-023-02379-4.

[4] Michael C. Heinrich, Heikki Joensuu, George D. Demetri, Christopher L. Corless, Jane Apperley, Jonathan A. Fletcher, Denis Soulieres, Stephan Dirnhofer, Amy Harlow, Ajia Town, Arin McKinley, Shane G. Supple, John Seymour, Lilla Di Scala, Allan van Oosterom, Richard Herrmann, Zariana Nikolova, Grant McArthur, and Imatinib Target Exploration Consortium Study B2225. Phase II, open-label study evaluating the activity of imatinib in treating life-threatening malignancies known to be associated with imatinib-sensitive tyrosine kinases. *Clinical Cancer Research*, 14:2717–2725, 2008. doi: 10.1158/1078-0432.CCR-07-4575.

[5] Dung T. Le, Jennifer N. Durham, Kellie N. Smith, Hao Wang, Bjarne R. Bartlett, Laveet K. Aulakh, Steve Lu, Holly Kemberling, Cara Wilt, Brandon S. Luber, Fay Wong, Nilofer S. Azad, Agnieszka A. Rucki, Dan Laheru, Ross Donehower, Atif Zaheer, George A. Fisher, Todd S. Crocenzi, James J. Lee, Tim F. Greten, Austin G. Duffy, Kristen K. Ciombor,

Aleksandra D. Eyring, Bao H. Lam, Andrew Joe, S. Peter Kang, Matthias Holdhoff, Ludmila Danilova, Leslie Cope, Christian Meyer, Shibin Zhou, Richard M. Goldberg, Deborah K. Armstrong, Katherine M. Bever, Amanda N. Fader, Janis Taube, Franck Housseau, David Spetzler, Nianqing Xiao, Drew M. Pardoll, Nickolas Papadopoulos, Kenneth W. Kinzler, James R. Eshleman, Bert Vogelstein, Robert A. Anders, and Luis A. Diaz, Jr. Mismatch repair deficiency predicts response of solid tumors to PD-1 blockade. *Science*, 357:409–413, 2017. doi: 10.1126/science.aan6733.

[6] John D. Hainsworth, Funda Meric-Bernstam, Charles Swanton, Herbert Hurwitz, David R. Spigel, Christopher Sweeney, Howard A. Burris, III, Ron Bose, Bongin Yoo, Alisha Stein, Mary Beattie, and Razelle Kurzrock. Targeted therapy for advanced solid tumors on the basis of molecular profiles: Results from MyPathway, an open-label, phase IIa multiple basket study. *Journal of Clinical Oncology*, 36:536–542, 2018. doi: 10.1200/JCO.2017.75.3780.

[7] Anirudh Prahallad, Chong Sun, Sidong Huang, Federica Di Nicolantonio, Ramon Salazar, Davide Zecchin, Roderick L. Beijersbergen, Alberto Bardelli, and René Bernards. Unresponsiveness of colon cancer to BRAF(V600E) inhibition through feedback activation of EGFR. *Nature*, 483:100–103, 2012. doi: 10.1038/nature10868.

[8] David M. Hyman, Igor Puzanov, Vivek Subbiah, Jason E. Faris, Ian Chau, Jean-Yves Blay, Jürgen Wolf, Noopur S. Raje, Eli L. Diamond, Antoine Hollebecque, Radj Gervais, Maria Elena Elez-Fernandez, Antoine Italiano, Ralf-Dieter Hofheinz, Manuel Hidalgo, Emily Chan, Martin Schuler, Susan Frances Lasserre, Martina Makrutzki, Florin Sirzen, Maria Luisa Veronese, Josep Tabernero, and José Baselga. Vemurafenib in multiple nonmelanoma cancers with BRAF V600 mutations. *New England Journal of Medicine*, 373:726–736, 2015. doi: 10.1056/NEJMoa1502309.

[9] Scott Kopetz, Axel Grothey, Rona Yaeger, Eric Van Cutsem, Jayesh Desai, Takayuki Yoshino, Harpreet Wasan, Fortunato Ciardiello, Fotios Loupakis, Yong Sang Hong, Neeltje Steeghs, Tormod K. Guren, Hendrik-Tobias Arkenau, Pilar Garcia-Alfonso, Per Pfeiffer, Sergey Orlov, Sara Lonardi, Elena Elez, Tae-Won Kim, Jan H.M. Schellens, Christina Guo, Asha Krishnan, Jeroen Dekervel, Van Morris, Aitana Calvo Ferrandiz, L.S. Tarpgaard, Michael Braun, Ashwin Gollerkeri, Christopher Keir, Kati Maharry, Michael Pickard, Janna Christy-Bittel, Lisa Anderson, Victor Sandor, and Josep Tabernero. Encorafenib, binimetinib, and cetuximab in BRAF V600E-mutated colorectal cancer. *New England Journal of Medicine*, 381:1632–1643, 2019. doi: 10.1056/NEJMoa1908075.

[10] Vanessa S. Rodrik-Outmezguine, Sarat Chandarlapaty, Nen C. Pagano, Poulikos I. Poulikakos, Maurizio Scaltriti, Elizabeth Moskatel, José Baselga, Sylvie Guichard, and Neal Rosen. mTOR kinase inhibition causes feedback-dependent biphasic regulation of AKT signaling. *Cancer Discovery*, 1(3):248–259, 2011. doi: 10.1158/2159-8290.CD-11-0085.

[11] Luigi Formisano, Yao Lu, Alberto Servetto, Ariella B. Hanker, Valerie M. Jansen, Joshua A. Bauer, Dhivya R. Sudhan, Angel L. Guerrero-Zotano, Sarah Croessmann, Yan Guo, Paula Gonzalez Ericsson, Kyung-min Lee, Mellissa J. Nixon, Luis J. Schwarz, Melinda E. Sanders, Teresa C. Dugger, Marcelo Rocha Cruz, Amir Behdad, Massimo Cristofanilli, Aditya Bardia, Joyce O'Shaughnessy, Rebecca J. Nagy, Richard B. Lanman, Nadia Solovieff, Wei He, Michelle Miller, Fei Su, Yu Shyr, Ingrid A. Mayer, Justin M. Balko, and Carlos L. Arteaga. Aberrant FGFR signaling mediates resistance to CDK4/6 inhibitors in ER+ breast cancer. *Nature Communications*, 10:1373, 2019. doi: 10.1038/s41467-019-09068-2.

[12] Kristen M. Cunanan, Alexia Iasonos, Ronglai Shen, Colin B. Begg, and Mithat Gönen. An efficient basket trial design. *Statistics in Medicine*, 36(10):1568–1579, 2017. doi: 10.1002/sim.7227.

[13] Cancer Genome Atlas Network. Comprehensive molecular portraits of human breast tumours. *Nature*, 490:61–70, 2012. doi: 10.1038/nature11412.

[14] Cancer Genome Atlas Network. Comprehensive molecular characterization of human colon and rectal cancer. *Nature*, 487:330–337, 2012. doi: 10.1038/nature11252.

[15] GTEx Consortium. The Genotype-Tissue Expression (GTEx) project. *Nature Genetics*, 45: 580–585, 2013. doi: 10.1038/ng.2653.

[16] GTEx Consortium. The GTEx consortium atlas of genetic regulatory effects across human tissues. *Science*, 369:1318–1330, 2020. doi: 10.1126/science.aaz1776.

[17] Mary J. Goldman, Brian Craft, Mim Hastie, Kristupas Repečka, Fran McDade, Akhil Kamath, Ayan Banerjee, Yunhai Luo, Dave Rogers, Angela N. Brooks, Jingchun Zhu, and David Haussler. Visualizing and interpreting cancer genomics data via the Xena platform. *Nature Biotechnology*, 38:675–678, 2020. doi: 10.1038/s41587-020-0546-8.

[18] Michael B. Eisen, Paul T. Spellman, Patrick O. Brown, and David Botstein. Cluster analysis and display of genome-wide expression patterns. *Proceedings of the National Academy of Sciences*, 95(25):14863–14868, 1998. doi: 10.1073/pnas.95.25.14863.

[19] Nir Friedman. Inferring cellular networks using probabilistic graphical models. *Science*, 303 (5659):799–805, 2004. doi: 10.1126/science.1094068.

[20] Jan Krumsiek, Karsten Suhre, Thomas Illig, Jerzy Adamski, and Fabian J. Theis. Gaussian graphical modeling reconstructs pathway reactions from high-throughput metabolomics data. *BMC Systems Biology*, 5:21, 2011. doi: 10.1186/1752-0509-5-21.

[21] Philipp Dettling, Roser Homs, Carlos Améndola, Mathias Drton, and Niels Richard Hansen. Identifiability in continuous Lyapunov models. *SIAM Journal on Matrix Analysis and Applications*, 44(4):1799–1821, 2023. doi: 10.1137/22M1520311.

[22] Aravind Subramanian, Rajiv Narayan, Steven M. Corsello, David D. Peck, Ted E. Natoli, Xiaodong Lu, Joshua Gould, John F. Davis, Andrew A. Tubelli, Jacob K. Asiedu, David L. Lahr, Jodi E. Hirschman, Zihan Liu, Melanie Donahue, Bina Julian, Mariya Khan, David Wadden, Ian C. Smith, Daniel Lam, Arthur Liberzon, Courtney Toder, Mukta Bagul, Marek Orzechowski, Oana M. Enache, Federica Piccioni, Sarah A. Johnson, Nicholas J. Lyons, Alice H. Berger, Alykhan F. Shamji, Angela N. Brooks, Anita Vrcic, Corey Flynn, Jacqueline Rosains, David Y. Takeda, Roger Hu, Desiree Davison, Justin Lamb, Kristin Ardlie, Larson Hogstrom, Peyton Greenside, Nathanael S. Gray, Paul A. Clemons, Serena Silver, Xiaoyun Wu, Wen-Ning Zhao, Willis Read-Button, Xiaohua Wu, Stephen J. Haggarty, Lucienne V. Ronco, Jesse S. Boehm, Stuart L. Schreiber, John G. Doench, Joshua A. Bittker, David E. Root, Bang Wong, and Todd R. Golub. A next generation connectivity map: L1000 platform and the first 1,000,000 profiles. *Cell*, 171:1437–1452.e17, 2017. doi: 10.1016/j.cell.2017.10.049.

[23] Wouter Saelens, Robrecht Cannoodt, Helena Todorov, and Yvan Saeys. A comparison of single-cell trajectory inference methods. *Nature Biotechnology*, 37:547–554, 2019. doi: 10.1038/s41587-019-0071-9.

[24] Volker Bergen, Marius Lange, Stefan Peidli, F. Alexander Wolf, and Fabian J. Theis. Generalizing RNA velocity to transient cell states through dynamical modeling. *Nature Biotechnology*, 38:1408–1414, 2020. doi: 10.1038/s41587-020-0591-3.

[25] Adam A. Margolin, Ilya Nemenman, Katia Basso, Chris Wiggins, Gustavo Stolovitzky, Riccardo Dalla Favera, and Andrea Califano. ARACNE: An algorithm for the reconstruction of gene regulatory networks in a mammalian cellular context. *BMC Bioinformatics*, 7:S7, 2006. doi: 10.1186/1471-2105-7-S1-S7.

[26] Vân Anh Huynh-Thu, Alexandre Irrthum, Louis Wehenkel, and Pierre Geurts. Inferring regulatory networks from expression data using tree-based methods. *PLoS ONE*, 5(9):e12776, 2010. doi: 10.1371/journal.pone.0012776.

[27] Sara Aibar, Carmen Bravo González-Blas, Thomas Moerman, Vân Anh Huynh-Thu, Hana Imrichova, Gert Hulselmans, Florian Rambow, Jean-Christophe Marine, Pierre Geurts, Jan Aerts, Joost van den Oord, Zeynep Kalender Atak, Jasper Wouters, and Stein Aerts. SCENIC: single-cell regulatory network inference and clustering. *Nature Methods*, 14:1083–1086, 2017. doi: 10.1038/nmeth.4463.

[28] Claudia Skok Gibbs, Christopher A. Jackson, Giuseppe-Antonio Saldi, Andreas Tjärnberg, Aashna Shah, Aaron Watters, Nicholas De Veaux, Konstantine Tchourine, Ren Yi, Tymor Hamamsy, Dayanne M. Castro, Nicholas Carriero, Bram L. Gorissen, David Gresham, Emily R. Miraldi, and Richard Bonneau. High-performance single-cell gene regulatory network inference at scale: the Inferelator 3.0. *Bioinformatics*, 38(9):2519–2528, 2022. doi: 10.1093/bioinformatics/btac117.

[29] Asako Sakaue-Sawano, Hiroshi Kurokawa, Toshifumi Morimura, Aki Hanyu, Hiroshi Hama, Hatsuki Osawa, Saori Kashiwagi, Kiyoko Fukami, Takaki Miyata, Hiroyuki Miyoshi, Takeshi Imamura, Masaharu Ogawa, Hisao Masai, and Atsushi Miyawaki. Visualizing spatiotemporal dynamics of multicellular cell-cycle progression. *Cell*, 132:487–498, 2008. doi: 10.1016/j.cell.2007.12.033.

[30] Chiaowen Joyce Hsiao, Po-Yuan Tung, John D. Blischak, Jonathan E. Burnett, Kenneth A. Barr, Kushal K. Dey, Matthew Stephens, and Yoav Gilad. Characterizing and inferring quantitative cell cycle phase in single-cell RNA-seq data analysis. *Genome Research*, 30: 611–621, 2020. doi: 10.1101/gr.247759.118.

[31] Diana Mahdessian, Anthony J. Cesnik, Christian Gnann, Frida Danielsson, Lovisa Stenström, Muhammad Arif, Cheng Zhang, Trang Le, Fredric Johansson, Rutger Schutten, Anna Bäckström, Ulrika Axelsson, Peter Thul, Nathan H. Cho, Oana Carja, Mathias Uhlén, Adil Mardinoglu, Charlotte Stadler, Cecilia Lindskog, Burcu Ayoglu, Manuel D. Leonetti, Fredrik Pontén, Devin P. Sullivan, and Emma Lundberg. Spatiotemporal dissection of the cell cycle with single-cell proteogenomics. *Nature*, 590:649–654, 2021. doi: 10.1038/s41586-021-03232-9.

[32] Ming Yuan and Yi Lin. Model selection and estimation in regression with grouped variables. *Journal of the Royal Statistical Society: Series B (Statistical Methodology)*, 68(1):49–67, 2006. doi: 10.1111/j.1467-9868.2005.00532.x.

[33] Rita Santos, Oleg Ursu, Anna Gaulton, A. Patrícia Bento, Ramesh S. Donadi, Cristian G. Bologa, Anneli Karlsson, Bissan Al-Lazikani, Anne Hersey, Tudor I. Oprea, and John P. Overington. A comprehensive map of molecular drug targets. *Nature Reviews Drug Discovery*, 16(1):19–34, 2017. doi: 10.1038/nrd.2016.230.

[34] Philippe L. Bedard, David M. Hyman, Matthew S. Davids, and Lillian L. Siu. Small molecules, big impact: 20 years of targeted therapy in oncology. *The Lancet*, 395(10229):1078–1088, 2020. doi: 10.1016/S0140-6736(20)30164-1.

[35] Ronald M. Evans and David J. Mangelsdorf. Nuclear receptors, RXR, and the big bang. *Cell*, 157(1):255–266, 2014. doi: 10.1016/j.cell.2014.03.012.

[36] Joel S. Parker, Michael Mullins, Maggie C.U. Cheang, Samuel Leung, David Voduc, Tammi Vickery, Sherri Davies, Christiane Fauron, Xiaping He, Zhiyuan Hu, John F. Quackenbush, Inge J. Stijleman, Juan Palazzo, J.S. Marron, Andrew B. Nobel, Elaine Mardis, Torsten O. Nielsen, Matthew J. Ellis, Charles M. Perou, and Philip S. Bernard. Supervised risk predictor of breast cancer based on intrinsic subtypes. *Journal of Clinical Oncology*, 27:1160–1167, 2009. doi: 10.1200/JCO.2008.18.1370.

[37] C. Lengauer, K. W. Kinzler, and B. Vogelstein. Genetic instability in colorectal cancers. *Nature*, 386:623–627, 1997. doi: 10.1038/386623a0.

[38] Liliane Michalik, Béatrice Desvergne, and Walter Wahli. Peroxisome-proliferator-activated receptors and cancers: complex stories. *Nature Reviews Cancer*, 4(1):61–70, 2004. doi: 10.1038/nrc1254.

[39] Susana Alvarez, Pierre Germain, Rosana Alvarez, Fátima Rodríguez-Barrios, Hinrich Gronemeyer, and Angel R. de Lera. Structure, function and modulation of retinoic acid receptor beta, a tumor suppressor. *The International Journal of Biochemistry & Cell Biology*, 39(7–8): 1406–1415, 2007. doi: 10.1016/j.biocel.2007.02.010.

[40] Mark A. Dawson and Tony Kouzarides. Cancer epigenetics: from mechanism to therapy. *Cell*, 150(1):12–27, 2012. doi: 10.1016/j.cell.2012.06.013.

[41] David A. Fruman, Honyin Chiu, Benjamin D. Hopkins, Shubha Bagrodia, Lewis C. Cantley, and Robert T. Abraham. The PI3K pathway in human disease. *Cell*, 170(4):605–635, 2017. doi: 10.1016/j.cell.2017.07.029.

[42] Shao-Cong Sun. CYLD: a tumor suppressor deubiquitinase regulating NF-κB activation and diverse biological processes. *Cell Death & Differentiation*, 17(1):25–34, 2010. doi: 10.1038/cdd.2009.43.

[43] E. Van Cutsem, C.-H. Köhne, E. Hitre, J. Zaluski, C.-R. Chang Chien, A. Makhson, G. D'Haens, T. Pintér, R. Lim, G. Bodoky, J. K. Roh, G. Folprecht, P. Ruff, C. Stroh, S. Tejpar, M. Schlichting, J. Nippgen, and P. Rougier. Cetuximab and chemotherapy as initial treatment for metastatic colorectal cancer. *New England Journal of Medicine*, 360(14): 1408–1417, 2009. doi: 10.1056/NEJMoa0805019.

[44] M. Peeters, T. J. Price, A. Cervantes, A. F. Sobrero, M. Ducreux, Y. Hotko, T. André, E. Chan, F. Lordick, C. J. A. Punt, et al. Randomized phase III study of panitumumab with fluorouracil, leucovorin, and irinotecan (FOLFIRI) compared with FOLFIRI alone as second-line treatment in patients with metastatic colorectal cancer. *Journal of Clinical Oncology*, 28(31):4706–4713, 2010. doi: 10.1200/JCO.2009.27.6055.

[45] H. Hurwitz, L. Fehrenbacher, W. Novotny, T. Cartwright, J. Hainsworth, W. Heim, J. Berlin, A. Baron, S. Griffing, E. Holmgren, N. Ferrara, G. Fyfe, B. Rogers, R. Ross, and F. Kabbinavar. Bevacizumab plus irinotecan, fluorouracil, and leucovorin for metastatic colorectal cancer. *New England Journal of Medicine*, 350(23):2335–2342, 2004. doi: 10.1056/NEJMoa032691.

[46] J. Tabernero, T. Yoshino, A. L. Cohn, R. Obermannova, G. Bodoky, R. Garcia-Carbonero, T.-E. Ciuleanu, D. C. Portnoy, E. Van Cutsem, A. Grothey, et al. Ramucirumab versus placebo in combination with second-line FOLFIRI in patients with metastatic colorectal carcinoma that progressed during or after first-line therapy with bevacizumab, oxaliplatin, and a fluoropyrimidine (RAISE): a randomised, double-blind, multicentre, phase 3 study. *The Lancet Oncology*, 16(5):499–508, 2015. doi: 10.1016/S1470-2045(15)70127-0.

[47] Karim Lounici, Massimiliano Pontil, Sara van de Geer, and Alexandre B. Tsybakov. Oracle inequalities and optimal inference under group sparsity. *Annals of Statistics*, 39(4):2164–2204, 2011. doi: 10.1214/11-AOS896.

[48] Nabil Guelzim, Samuele Bottani, Paul Bourgine, and François Képès. Topological and causal structure of the yeast transcriptional regulatory network. *Nature Genetics*, 31(1):60–63, 2002. doi: 10.1038/ng873.

[49] M. Madan Babu, Nicholas M. Luscombe, L. Aravind, Mark Gerstein, and Sarah A. Teichmann. Structure and evolution of transcriptional regulatory networks. *Current Opinion in Structural Biology*, 14(3):283–291, 2004. doi: 10.1016/j.sbi.2004.05.004.

[50] Helena L. Crowell, Charlotte Soneson, Pierre-Luc Germain, Daniela Calini, Ludovic Collin, Catarina Raposo, Dheeraj Malhotra, and Mark D. Robinson. muscat detects subpopulation-specific state transitions from multi-sample multi-condition single-cell transcriptomics data. *Nature Communications*, 11:6077, 2020. doi: 10.1038/s41467-020-19894-4.

[51] Jordan W. Squair, Matthieu Gautier, Claudia Kathe, Mark A. Anderson, Nicholas D. James, Thomas H. Hutson, Rémi Hudelle, Taha Qaiser, Kaya J. E. Matson, Quentin Barraud, Ariel J. Levine, Gioele La Manno, Michael A. Skinnider, and Grégoire Courtine. Confronting false discoveries in single-cell differential expression. *Nature Communications*, 12:5692, 2021. doi: 10.1038/s41467-021-25960-2.

[52] Dénes Türei, Tamás Korcsmáros, and Julio Saez-Rodriguez. OmniPath: guidelines and gateway for literature-curated signaling pathway resources. *Nature Methods*, 13:966–967, 2016. doi: 10.1038/nmeth.4077.

[53] Dénes Türei, Alberto Valdeolivas, Lejla Gul, Nicolàs Palacio-Escat, Michal Klein, Olga Ivanova, Márton Ölbei, Attila Gábor, Fabian Theis, Dezső Módos, Tamás Korcsmáros, and Julio Saez-Rodriguez. Integrated intra- and intercellular signaling knowledge for multicellular omics analysis. *Molecular Systems Biology*, 17:e9923, 2021. doi: 10.15252/msb.20209923.

[54] Sophia Müller-Dott, Eirini Tsirvouli, Miguel Vazquez, Ricardo O. Ramirez Flores, Pau Badia-i-Mompel, Robin Fallegger, Dénes Türei, Astrid Lægreid, and Julio Saez-Rodriguez. Expanding the coverage of regulons from high-confidence prior knowledge for accurate estimation of transcription factor activities. *Nucleic Acids Research*, 51:10934–10949, 2023. doi: 10.1093/nar/gkad841.

[55] Markus Meissner, Monika Stein, Carmen Urbich, Kerstin Reisinger, Guntram Suske, Bart Staels, Roland Kaufmann, and Jens Gille. PPARα activators inhibit vascular endothelial growth factor receptor-2 expression by repressing Sp1-dependent DNA binding and transactivation. *Circulation Research*, 94:324–332, 2004. doi: 10.1161/01.RES.0000113781.08139.81.

[56] Kristin J. Lastwika, Willie Wilson, III, Qing Kay Li, Jeffrey Norris, Haiying Xu, Sharon R. Ghazarian, Hiroshi Kitagawa, Shigeru Kawabata, Janis M. Taube, Sheng Yao, Linda N. Liu, Joell J. Gills, and Phillip A. Dennis. Control of PD-L1 expression by oncogenic activation of the AKT–mTOR pathway in non-small cell lung cancer. *Cancer Research*, 76(2):227–238, 2016. doi: 10.1158/0008-5472.CAN-14-3362.

[57] Lawrence P. Andrews, Ariel E. Marciscano, Charles G. Drake, and Dario A. A. Vignali. LAG3 (CD223) as a cancer immunotherapy target. *Immunological Reviews*, 276(1):80–96, 2017. doi: 10.1111/imr.12519.

[58] Brendan D. Manning and Alex Toker. AKT/PKB signaling: Navigating the network. *Cell*, 169(3):381–405, 2017. doi: 10.1016/j.cell.2017.04.001.

[59] Kimberly H. Kim and Charles W. M. Roberts. Targeting EZH2 in cancer. *Nature Medicine*, 22(2):128–134, 2016. doi: 10.1038/nm.4036.

[60] Joan Massagué. TGFβ in cancer. *Cell*, 134(2):215–230, 2008. doi: 10.1016/j.cell.2008.07.001.

[61] Yi Liu, Yasunori Deguchi, Rui Tian, Daoyan Wei, Ling Wu, Weidong Chen, Weiguo Xu, Min Xu, Fuyao Liu, Shen Gao, Jonathan C. Jaoude, Sarah P. Chrieki, Micheline J. Moussalli, Mihai Gagea, Jeffrey Morris, Russell R. Broaddus, Xiangsheng Zuo, and Imad Shureiqi. Pleiotropic effects of PPARD accelerate colorectal tumorigenesis, progression, and invasion. *Cancer Research*, 79(5):954–969, 2019. doi: 10.1158/0008-5472.CAN-18-1790.

[62] Richard S. Finn, Miguel Martin, Hope S. Rugo, Stephen Jones, Seock-Ah Im, Karen Gelmon, Nadia Harbeck, Oleg N. Lipatov, Janice M. Walshe, Stacy Moulder, Eric Gauthier, Dongrui R. Lu, Sophia Randolph, Véronique Diéras, and Dennis J. Slamon. Palbociclib and letrozole in advanced breast cancer. *New England Journal of Medicine*, 375:1925–1936, 2016. doi: 10.1056/NEJMoa1607303.

[63] Fabrice André, Eva Ciruelos, Gabor Rubovszky, Mario Campone, Sibylle Loibl, Hope S. Rugo, Hiroji Iwata, Pierfranco Conte, Ingrid A. Mayer, Bella Kaufman, Toshinari Yamashita, Yen-Shen Lu, Kenichi Inoue, Masato Takahashi, Zsuzsanna Pápai, Anne-Sophie Longin, David Mills, Celine Wilke, Samit Hirawat, and Dejan Juric. Alpelisib for PIK3CA-mutated, hormone receptor-positive advanced breast cancer. *New England Journal of Medicine*, 380: 1929–1940, 2019. doi: 10.1056/NEJMoa1813904.

[64] José Baselga, Mario Campone, Martine Piccart, Howard A. Burris, III, Hope S. Rugo, Tarek Sahmoud, Shinzaburo Noguchi, Michael Gnant, Kathleen I. Pritchard, Fabienne Lebrun, J. Thaddeus Beck, Yoshinori Ito, Denise Yardley, Ines Deleu, Alejandra Perez, Thomas Bachelot, Luc Vittori, Zhiying Xu, Pabak Mukhopadhyay, David Lebwohl, and Gabriel N. Hortobagyi. Everolimus in postmenopausal hormone-receptor-positive advanced breast cancer. *New England Journal of Medicine*, 366:520–529, 2012. doi: 10.1056/NEJMoa1109653.

[65] J. Y. Douillard, D. Cunningham, A. D. Roth, M. Navarro, R. D. James, P. Karasek, P. Jandik, T. Iveson, J. Carmichael, M. Alakl, G. Gruia, L. Awad, and P. Rougier. Irinotecan combined with fluorouracil compared with fluorouracil alone as first-line treatment for metastatic colorectal cancer: a multicentre randomised trial. *Lancet*, 355:1041–1047, 2000. doi: 10.1016/s0140-6736(00)02034-1.

[66] Leonard B. Saltz, John V. Cox, Charles Blanke, Lee S. Rosen, Louis Fehrenbacher, Malcolm J. Moore, Jean A. Maroun, Stephen P. Ackland, Paula K. Locker, Nicoletta Pirotta, Gary L. Elfring, and Langdon L. Miller. Irinotecan plus fluorouracil and leucovorin for metastatic colorectal cancer. Irinotecan Study Group. *New England Journal of Medicine*, 343:905–914, 2000. doi: 10.1056/NEJM200009283431302.

[67] Barbara Zdrazil, Eloy Felix, Fiona Hunter, Emma J. Manners, James Blackshaw, Sybilla Corbett, Marleen de Veij, Harris Ioannidis, David Mendez Lopez, Juan F. Mosquera, Maria Paula Magarinos, Nicolas Bosc, Ricardo Arcila, Tevfik Kizilören, Anna Gaulton, A. Patrícia Bento, Melissa F. Adasme, Peter Monecke, Gregory A. Landrum, and Andrew R. Leach. The ChEMBL database in 2023: a drug discovery platform spanning multiple bioactivity data types and time periods. *Nucleic Acids Research*, 52:D1180–D1192, 2024. doi: 10.1093/nar/gkad1004.

[68] WHO Collaborating Centre for Drug Statistics Methodology. WHO Anatomical Therapeutic Chemical (ATC) classification of drugs, as distributed in ChEMBL release 37. https://ftp.ebi.ac.uk/pub/databases/chembl/ChEMBLdb/releases/chembl_37/chembl_37_release_notes.txt, 2026.

[69] U.S. National Library of Medicine. Medical subject headings (MeSH), 2026 edition. https://www.nlm.nih.gov/mesh/, 2026. Courtesy of the U.S. National Library of Medicine.

[70] Shom Goel, Qi Wang, April C. Watt, Sara M. Tolaney, Deborah A. Dillon, Wei Li, Susanne Ramm, Adam C. Palmer, Haluk Yuzugullu, Vinay Varadan, David Tuck, Lyndsay N. Harris, Kwok-Kin Wong, X. Shirley Liu, Piotr Sicinski, Eric P. Winer, Ian E. Krop, and Jean J. Zhao. Overcoming therapeutic resistance in HER2-positive breast cancers with CDK4/6 inhibitors. *Cancer Cell*, 29(3):255–269, 2016. doi: 10.1016/j.ccell.2016.02.006.

[71] Navid Sobhani, Anne Fassl, Giuseppina Mondani, Daniele Generali, and Tobias Otto. Targeting aberrant FGFR signaling to overcome CDK4/6 inhibitor resistance in breast cancer. *Cells*, 10(2):293, 2021. doi: 10.3390/cells10020293.

[72] D. Adkins, J. Ley, P. Neupane, F. Worden, A. G. Sacco, K. Palka, J. E. Grilley-Olson, et al. Palbociclib and cetuximab in platinum-resistant and in cetuximab-resistant human papillomavirus-unrelated head and neck cancer: a multicentre, multigroup, phase 2 trial. *The Lancet Oncology*, 20(9):1295–1305, 2019. doi: 10.1016/S1470-2045(19)30405-X.

[73] D. R. Adkins, J. C. Lin, A. Sacco, J. Ley, P. Oppelt, V. Vanchenko, N. Komashko, C. J. Yen, T. Wise-Draper, J. Lopez-Picazo Gonzalez, S. Radulovic, Q. Shen, H. Thurm, J. F. Martini, J. Hoffman, X. Huang, B. Melichar, and M. Tahara. Palbociclib and cetuximab compared with placebo and cetuximab in platinum-resistant, cetuximab-naïve, human papillomavirus-unrelated recurrent or metastatic head and neck squamous cell carcinoma: A double-blind, randomized, phase 2 trial. *Oral Oncology*, 115:105192, 2021. doi: 10.1016/j.oraloncology.2021.105192.

[74] J. D. Sorah, D. T. Moore, M. J. Reilley, M. E. Salem, T. Triglianos, A. J. McRee, M. S. Lee, H. K. Sanoff, and A. S. Somasundaram. Phase II single-arm study of palbociclib and cetuximab in anti-EGFR naive patients with KRAS/NRAS/BRAF wild-type, metastatic colorectal cancer. *The Oncologist*, 30(10):oyaf305, 2025. doi: 10.1093/oncolo/oyaf305.

[75] Kimmie Ng, Halla S. Nimeiri, Nadine J. McCleary, Thomas A. Abrams, Matthew B. Yurgelun, James M. Cleary, Douglas A. Rubinson, Deborah Schrag, Rebecca Miksad, Andrea J. Bullock, Jill Allen, Dan Zuckerman, Emily Chan, Jennifer A. Chan, Brian M. Wolpin, Michael Constantine, Douglas J. Weckstein, Meredith A. Faggen, Christian A. Thomas, Chryssanthi Kournioti, Chen Yuan, Christine Ganser, Brittney Wilkinson, Christopher Mackintosh, Hui Zheng, Bruce W. Hollis, Jeffrey A. Meyerhardt, and Charles S. Fuchs. Effect of high-dose vs standard-dose vitamin D_3 supplementation on progression-free survival among patients with advanced or metastatic colorectal cancer: The SUNSHINE randomized clinical trial. *JAMA*, 321(14):1370–1379, 2019. doi: 10.1001/jama.2019.2402.

[76] A. Wood, S. George, N. Adra, S. Chintala, N. Damayanti, and R. Pili. Phase I study of the mTOR inhibitor everolimus in combination with the histone deacetylase inhibitor panobinostat in patients with advanced clear cell renal cell carcinoma. *Investigational New Drugs*, 38(4):1108–1116, 2020. doi: 10.1007/s10637-019-00864-7.

[77] Brian M. Wolpin, Kimmie Ng, Andrew X. Zhu, Thomas Abrams, Peter C. Enzinger, Nadine J. McCleary, Deborah Schrag, Eunice L. Kwak, Jill N. Allen, Pankaj Bhargava, Jennifer A. Chan, Wolfram Goessling, Lawrence S. Blaszkowsky, Jeffrey G. Supko, Meaghan Elliot, Kaori Sato, E. Regan, Jeffrey A. Meyerhardt, and Charles S. Fuchs. Multicenter phase II study of tivozanib (AV-951) and everolimus (RAD001) for patients with refractory, metastatic colorectal cancer. *The Oncologist*, 18(4):377–378, e8–e16, 2013. doi: 10.1634/theoncologist.2012-0378.

[78] B. Besse, N. Leighl, J. Bennouna, V. A. Papadimitrakopoulou, N. Blais, A. M. Traynor, J.-C. Soria, S. Gogov, N. Miller, V. Jehl, and B. E. Johnson. Phase II study of everolimus-erlotinib in previously treated patients with advanced non-small-cell lung cancer. *Annals of Oncology*, 25(2):409–415, 2014. doi: 10.1093/annonc/mdt536.

[79] Alain Ravaud, Carlos Gomez-Roca, Marie-Quitterie Picat, Laurence Digue, Christine Chevreau, Anne Gimbert, Emmanuelle Chauzit, Rémi Sitta, François Cornelis, Julien Asselineau, Richard Aziza, Antoine Daste, Cathy Quemener, Jessica Baud, Andreas Bikfalvi, Delphine Pedenon-Perichout, Adélaïde Doussau, Mathieu Molimard, and Jean-Pierre Delord. Phase I study of axitinib and everolimus in metastatic solid tumours and extension to metastatic renal cell carcinoma: Results of EVAX study. *European Journal of Cancer*, 85:39–48, 2017. doi: 10.1016/j.ejca.2017.07.031.

[80] Ana M. Molina, Darren R. Feldman, Martin H. Voss, Michelle S. Ginsberg, Michael S. Baum, Dion R. Brocks, Patricia M. Fischer, Michael J. Trinos, Sujata Patil, and Robert J. Motzer.

Phase I trial of everolimus plus sunitinib in patients with metastatic renal cell carcinoma. *Cancer*, 118(7):1868–1876, 2012. doi: 10.1002/cncr.26429.

[81] D. Cunningham, Y. Humblet, S. Siena, D. Khayat, H. Bleiberg, A. Santoro, D. Bets, M. Mueser, A. Harstrick, C. Verslype, I. Chau, and E. Van Cutsem. Cetuximab monotherapy and cetuximab plus irinotecan in irinotecan-refractory metastatic colorectal cancer. *New England Journal of Medicine*, 351(4):337–345, 2004. doi: 10.1056/NEJMoa033025.

[82] E. Van Cutsem, J. Tabernero, R. Lakomy, H. Prenen, J. Prausová, T. Macarulla, P. Ruff, G. A. van Hazel, V. Moiseyenko, D. Ferry, J. McKendrick, J. Polikoff, A. Tellier, R. Castan, and C. Allegra. Addition of aflibercept to fluorouracil, leucovorin, and irinotecan improves survival in a phase III randomized trial in patients with metastatic colorectal cancer previously treated with an oxaliplatin-based regimen. *Journal of Clinical Oncology*, 30(28):3499–3506, 2012. doi: 10.1200/JCO.2012.42.8201.

[83] Scott Kopetz, Katherine A. Guthrie, Van K. Morris, Heinz-Josef Lenz, Anthony M. Magliocco, Dipen Maru, Yibing Yan, Richard Lanman, Ganiraju Manyam, David S. Hong, Alexey Sorokin, Chloe E. Atreya, Luis A. Diaz, Carmen Allegra, Kanwal P. Raghav, Stephen E. Wang, Christopher H. Lieu, Shannon L. McDonough, Philip A. Philip, and Howard S. Hochster. Randomized trial of irinotecan and cetuximab with or without vemurafenib in BRAF-mutant metastatic colorectal cancer (SWOG S1406). *Journal of Clinical Oncology*, 39(4):285–294, 2021. doi: 10.1200/JCO.20.01994.

[84] C. Eng, A. Bessudo, L. L. Hart, A. Severtsev, O. Gladkov, L. Müller, M. V. Kopp, V. Vladimirov, R. Langdon, B. Kotiv, S. Barni, C. Hsu, E. Bolotin, R. von Roemeling, B. Schwartz, and J. C. Bendell. A randomized, placebo-controlled, phase 1/2 study of tivantinib (ARQ 197) in combination with irinotecan and cetuximab in patients with metastatic colorectal cancer with wild-type KRAS who have received first-line systemic therapy. *International Journal of Cancer*, 139(1):177–186, 2016. doi: 10.1002/ijc.30049.

[85] Vladimir J. N. Bykov, Sofi E. Eriksson, Julie Bianchi, and Klas G. Wiman. Targeting mutant p53 for efficient cancer therapy. *Nature Reviews Cancer*, 18(2):89–102, 2018. doi: 10.1038/nrc.2017.109.

[86] David A. Sallman, Amy E. DeZern, Guillermo Garcia-Manero, David P. Steensma, Gail J. Roboz, Mikkael A. Sekeres, Thomas Cluzeau, Kendra L. Sweet, Amy McLemore, Kathy L. McGraw, John Puskas, Ling Zhang, Jiqiang Yao, Qianxing Mo, Lisa Nardelli, Najla H. Al Ali, Eric Padron, Greg Korbel, Eyal C. Attar, Hagop M. Kantarjian, Jeffrey E. Lancet, Pierre Fenaux, Alan F. List, and Rami S. Komrokji. Eprenetapopt (APR-246) and azacitidine in *TP53*-mutant myelodysplastic syndromes. *Journal of Clinical Oncology*, 39(14):1584–1594, 2021. doi: 10.1200/JCO.20.02341.

[87] Tong-Chuan He, Timothy A. Chan, Bert Vogelstein, and Kenneth W. Kinzler. PPARδ is an APC-regulated target of nonsteroidal anti-inflammatory drugs. *Cell*, 99(3):335–345, 1999. doi: 10.1016/S0092-8674(00)81664-5.

[88] Rajnish A. Gupta, Dingzhi Wang, Sharada Katkuri, Haibin Wang, Sudhansu K. Dey, and Raymond N. DuBois. Activation of nuclear hormone receptor peroxisome proliferator-activated receptor-δ accelerates intestinal adenoma growth. *Nature Medicine*, 10(3):245–247, 2004. doi: 10.1038/nm993.

[89] Dingzhi Wang, Haibin Wang, Qiong Shi, Sharada Katkuri, Walter Wahli, Béatrice Desvergne, Sanjoy K. Das, Sudhansu K. Dey, and Raymond N. DuBois. Prostaglandin E2 promotes colorectal adenoma growth via transactivation of the nuclear peroxisome proliferator-activated receptor δ. *Cancer Cell*, 6(3):285–295, 2004. doi: 10.1016/j.ccr.2004.08.011.

[90] Yuzhi Yin, Robert G. Russell, Luis E. Dettin, Renkui Bai, Zhi-Liang Wei, Alan P. Kozikowski, Levy Kopelovich, and Robert I. Glazer. Peroxisome proliferator-activated receptor δ and γ agonists differentially alter tumor differentiation and progression during mammary carcinogenesis. *Cancer Research*, 65(9):3950–3957, 2005. doi: 10.1158/0008-5472.CAN-04-3990.

[91] Hongyan Yuan, Jin Lu, Junfeng Xiao, Geeta Upadhyay, Rachel Umans, Bhaskar Kallakury, Yuzhi Yin, Michael E. Fant, Levy Kopelovich, and Robert I. Glazer. PPARδ induces estrogen receptor-positive mammary neoplasia through an inflammatory and metabolic phenotype linked to mTOR activation. *Cancer Research*, 73(14):4349–4361, 2013. doi: 10.1158/0008-5472.CAN-13-0322.

[92] Yaacov Barak, Debbie Liao, Weimin He, Estelita S. Ong, Michael C. Nelson, Jerrold M. Olefsky, Richard Boland, and Ronald M. Evans. Effects of peroxisome proliferator-activated receptor δ on placentation, adiposity, and colorectal cancer. *Proceedings of the National Academy of Sciences of the USA*, 99:303–308, 2002.

[93] Fred S. Harman, Christopher J. Nicol, Holly E. Marin, Jerrold M. Ward, Frank J. Gonzalez, and Jeffrey M. Peters. Peroxisome proliferator-activated receptor-δ attenuates colon carcinogenesis. *Nature Medicine*, 10(5):481–483, 2004. doi: 10.1038/nm1026.

[94] Karen R. Reed, Owen J. Sansom, Anthony J. Hayes, Andreas J. Gescher, Douglas J. Winton, Jeffrey M. Peters, and Alan R. Clarke. PPARδ status and Apc-mediated tumourigenesis in the mouse intestine. *Oncogene*, 23:8992–8996, 2004.

[95] Xiangsheng Zuo, Zhanglong Peng, Micheline J. Moussalli, Jeffrey S. Morris, Russell R. Broaddus, Susan M. Fischer, and Imad Shureiqi. Targeted genetic disruption of peroxisome proliferator-activated receptor-δ and colonic tumorigenesis. *Journal of the National Cancer Institute*, 101(10):762–767, 2009. doi: 10.1093/jnci/djp078.

[96] Mark B. Gerstein, Anshul Kundaje, Manoj Hariharan, Stephen G. Landt, Koon-Kiu Yan, Chao Cheng, Xinmeng Jasmine Mu, Ekta Khurana, Joel Rozowsky, Roger Alexander, Renqiang Min, Pedro Alves, Alexej Abyzov, Nick Addleman, Nitin Bhardwaj, Alan P. Boyle, Philip Cayting, Alexandra Charos, David Z. Chen, Yong Cheng, Declan Clarke, Catharine Eastman, Ghia Euskirchen, Seth Frietze, Yao Fu, Jason Gertz, Fabian Grubert, Arif Harmanci, Preti Jain, Maya Kasowski, Phil Lacroute, Jing Leng, Jin Lian, Hannah Monahan, Henriette O'Geen, Zhengqing Ouyang, E. Christopher Partridge, Dorrelyn Patacsil, Florencia Pauli, Debasish Raha, Lucia Ramirez, Timothy E. Reddy, Brian Reed, Minyi Shi, Teri Slifer, Jing Wang, Linfeng Wu, Xinqiong Yang, Kevin Y. Yip, Gili Zilberman-Schapira, Serafim Batzoglou, Arend Sidow, Peggy J. Farnham, Richard M. Myers, Sherman M. Weissman, and Michael Snyder. Architecture of the human regulatory network derived from ENCODE data. *Nature*, 489(7414):91–100, 2012. doi: 10.1038/nature11245.

[97] Soudeh Ghafouri-Fard, Tayyebeh Khoshbakht, Bashdar Mahmud Hussen, Peixin Dong, Nikolaus Gassler, Mohammad Taheri, Aria Baniahmad, and Nader Akbari Dilmaghani. A review on the role of cyclin dependent kinases in cancers. *Cancer Cell International*, 22(1): 325, 2022. doi: 10.1186/s12935-022-02747-z.

[98] Kosuke Yoshihara, Maria Shahmoradgoli, Emmanuel Martínez, Rahulsimham Vegesna, Hoon Kim, Wandaliz Torres-Garcia, Victor Treviño, Hui Shen, Peter W. Laird, Douglas A. Levine, Scott L. Carter, Gad Getz, Katherine Stemke-Hale, Gordon B. Mills, and Roel G.W. Verhaak. Inferring tumour purity and stromal and immune cell admixture from expression data. *Nature Communications*, 4:2612, 2013. doi: 10.1038/ncomms3612.

[99] Etienne Becht, Nicolas A. Giraldo, Laetitia Lacroix, Bénédicte Buttard, Nabila Elarouci, Florent Petitprez, Janick Selves, Pierre Laurent-Puig, Catherine Sautès-Fridman, Wolf H. Fridman, and Aurélien de Reyniès. Estimating the population abundance of tissue-infiltrating

immune and stromal cell populations using gene expression. *Genome Biology*, 17:218, 2016. doi: 10.1186/s13059-016-1070-5.

[100] Liacine Bouaoun, Dmitriy Sonkin, Maude Ardin, Monica Hollstein, Graham Byrnes, Jiri Zavadil, and Magali Olivier. TP53 variations in human cancers: New lessons from the IARC TP53 Database and genomics data. *Human Mutation*, 37(9):865–876, 2016. doi: 10.1002/humu.23035.

[101] Ethan Cerami, Jianjiong Gao, Ugur Dogrusoz, Benjamin E. Gross, Selcuk Onur Sumer, Bülent Arman Aksoy, Anders Jacobsen, Caitlin J. Byrne, Michael L. Heuer, Erik Larsson, Yevgeniy Antipin, Boris Reva, Arthur P. Goldberg, Chris Sander, and Nikolaus Schultz. The cBio cancer genomics portal: an open platform for exploring multidimensional cancer genomics data. *Cancer Discovery*, 2:401–404, 2012. doi: 10.1158/2159-8290.CD-12-0095.

[102] Jianjiong Gao, Bülent Arman Aksoy, Ugur Dogrusoz, Gideon Dresdner, Benjamin Gross, S. Onur Sumer, Yichao Sun, Anders Jacobsen, Rileen Sinha, Erik Larsson, Ethan Cerami, Chris Sander, and Nikolaus Schultz. Integrative analysis of complex cancer genomics and clinical profiles using the cBioPortal. *Science Signaling*, 6:pl1, 2013. doi: 10.1126/scisignal.2004088.

[103] Katherine A. Hoadley, Christina Yau, Toshinori Hinoue, Denise M. Wolf, Alexander J. Lazar, Esther Drill, Ronglai Shen, Alison M. Taylor, Andrew D. Cherniack, Vésteinn Thorsson, Rehan Akbani, Reanne Bowlby, Christopher K. Wong, Maciej Wiznerowicz, Francisco Sanchez-Vega, A. Gordon Robertson, Barbara G. Schneider, Michael S. Lawrence, Houtan Noushmehr, Tathiane M. Malta, Cancer Genome Atlas Network, Joshua M. Stuart, Christopher C. Benz, and Peter W. Laird. Cell-of-origin patterns dominate the molecular classification of 10,000 tumors from 33 types of cancer. *Cell*, 173:291–304.e6, 2018. doi: 10.1016/j.cell.2018.03.022.

[104] Ruth L. Seal, Bryony Braschi, Kristian Gray, Tamsin E. M. Jones, Susan Tweedie, Liora Haim-Vilmovsky, and Elspeth A. Bruford. Genenames.org: the HGNC resources in 2023. *Nucleic Acids Research*, 51:D1003–D1009, 2023. doi: 10.1093/nar/gkac888.

[105] Yang Liu, Nilay S. Sethi, Toshinori Hinoue, Barbara G. Schneider, Andrew D. Cherniack, Francisco Sanchez-Vega, Jose A. Seoane, Farshad Farshidfar, Reanne Bowlby, Mirazul Islam, Jaegil Kim, Walid Chatila, Rehan Akbani, Rupa S. Kanchi, Charles S. Rabkin, Joseph E. Willis, Kenneth K. Wang, Shannon J. McCall, Lopa Mishra, Akinyemi I. Ojesina, Susan Bullman, Chandra Sekhar Pedamallu, Alexander J. Lazar, Ryo Sakai, Cancer Genome Atlas Research Network, Vésteinn Thorsson, Adam J. Bass, and Peter W. Laird. Comparative molecular analysis of gastrointestinal adenocarcinomas. *Cancer Cell*, 33:721–735.e8, 2018. doi: 10.1016/j.ccell.2018.03.010.

[106] Ian E. Krop, Ingrid A. Mayer, Vinod Ganju, Maura Dickler, Stephen Johnston, Serafin Morales, Denise A. Yardley, Bohuslav Melichar, Andres Forero-Torres, Soo Chin Lee, Richard de Boer, Katarina Petrakova, Susanne Vallentin, Edith A. Perez, Martine Piccart, Matthew Ellis, Eric Winer, Steven Gendreau, Mika Derynck, Mark Lackner, Gallia Levy, Jiaheng Qiu, Jing He, and Peter Schmid. Pictilisib for oestrogen receptor-positive, aromatase inhibitor-resistant, advanced or metastatic breast cancer (FERGI): a randomised, double-blind, placebo-controlled, phase 2 trial. *Lancet Oncology*, 17:811–821, 2016. doi: 10.1016/S1470-2045(16)00106-6.

[107] Julian R. Molina, Scott H. Kaufmann, Joel M. Reid, Stephen D. Rubin, Marina Gálvez-Peralta, Robert Friedman, Karen S. Flatten, Kevin M. Koch, Tona M. Gilmer, Robert J. Mullin, Roxanne C. Jewell, Sara J. Felten, Sumithra J. Mandrekar, Alex A. Adjei, and Charles Erlichman. Evaluation of lapatinib and topotecan combination therapy: tissue culture, murine xenograft, and phase I clinical trial data. *Clinical Cancer Research*, 14(23):7900–7908, 2008. doi: 10.1158/1078-0432.CCR-08-0415.

[108] Tressie A. Posey, Joan Jacob, Ashlyn Parkhurst, Shraddha Subramanian, Liezl E. Francisco, Zhengdong Liang, and Kendra S. Carmon. Loss of LGR5 through therapy-induced downregulation or gene ablation is associated with resistance and enhanced MET-STAT3 signaling in colorectal cancer cells. *Molecular Cancer Therapeutics*, 22(5):667–678, 2023. doi: 10.1158/1535-7163.MCT-22-0415.

[109] Haidong Dong, Scott E. Strome, Diva R. Salomao, Hideto Tamura, Fumiya Hirano, Dallas B. Flies, Patrick C. Roche, Jun Lu, Gefeng Zhu, Koji Tamada, Vanda A. Lennon, Esteban Celis, and Lieping Chen. Tumor-associated B7-H1 promotes T-cell apoptosis: a potential mechanism of immune evasion. *Nature Medicine*, 8(8):793–800, 2002. doi: 10.1038/nm730.

Supplementary Information

Section S1 (Mathematical Proofs), Section S2 (Figures S1–S3), and Section S3 (Tables S1–S11)

This supplement has three parts. Section S1 gives complete statements and proofs of the theoretical results summarized in Methods (Section 5.3): notation and error constants (Section S1.1), the expected lag covariances (Theorem 1; Section S1.2), recovery of interaction signs up to a positive scale factor (Theorem 2; Section S1.3), uniqueness of the fitted network and the random-ordering null distribution (Section S1.4), and technical notes on the synthetic and pseudo-bulk benchmarks (Section S1.5). Section S2 contains Supplementary Figures S1–S3: the synthetic benchmark grid, histograms of raw tumor-versus-healthy interaction changes, and the three-block bipartite view of the shared subnetwork. Section S3 contains Supplementary Tables S1–S11 with the full numerical results behind the main-text claims; each figure and table caption notes the main-text figure or section it relates to.

S1 Complete Mathematical Proofs and Technical Notes (*Related to Methods*)

S1.1 Notation, error constants, and auxiliary lemmas

Recall from Definitions 1 and 2 in Methods that $z_i = x^i_{t_i} \in \mathbb{R}^p$ $(i \in \{1,\dots,n\})$ denotes the i-th observed snapshot at progression time t_i and $\bar{z} = \frac{1}{n}\sum_{i=1}^n z_i$ is the sample mean across the n snapshots. Further, π is the permutation sorting the distinct approximate clock values $\tau = (\tau_1,\dots,\tau_n)$ in ascending order $(\theta_k = \tau_{\pi(k)})$, $w_k = z_{\pi(k)} - \bar{z}$ $(k \in \{1,\dots,n\})$ is the k-th mean-centered clock-ordered snapshot, and $S = \frac{1}{n-1}\sum_{k=1}^n w_k w_k^\top = \frac{1}{n-1}\sum_{a=1}^n (z_a - \bar{z})(z_a - \bar{z})^\top$ is the static sample covariance (Eq. (4)). Throughout our formal analysis, $B \in \mathbb{R}^{p\times p}$ is Hurwitz stable ($\mathrm{Re}\,\lambda_i(B) < 0$), the pair (B, A) is controllable (for example, $AA^\top \succ 0$) so that the Lyapunov equation $B\Sigma + \Sigma B^\top = -AA^\top$ (Eq. (2)) admits a unique positive-definite stationary covariance $\Sigma \succ 0$. We also assume that the initial states $(z^0, \tilde{z}^1, \dots, \tilde{z}^n)$ are independent of the driving Brownian motions $(W^0, \tilde{W}^1, \dots, \tilde{W}^n)$. Define the matrix-exponential bound κ and the first- and second-order error constants a_1, a_2:

$$\kappa := \sup_{h\ge 0} \|e^{Bh}\|_2 < \infty, \qquad a_1 := \|B\|_2\, \kappa\, \|\Sigma\|_F, \qquad a_2 := \|B\|_2^2\, \kappa\, \|\Sigma\|_F. \tag{S1}$$

Here κ is finite because $h \mapsto \|e^{Bh}\|_2$ is continuous on $[0,\infty)$ and decays exponentially as $h \to \infty$ by Hurwitz stability of B. For index lag $\ell \in \{1,\dots,n-2\}$, there are $N := n - \ell \ge 2$ lag-ℓ sample pairs $(w_{k+\ell}, w_k)$ $(k = 1,\dots,N)$. Denote the true-time step of the k-th pair by $h_k := t_{k+\ell} - t_k > 0$, with mean $\bar{h} := \frac{1}{N}\sum_{k=1}^N h_k$ and mean of squares $\overline{h^2} := \frac{1}{N}\sum_{k=1}^N h_k^2$. By contrast, the signed true-time step between the clock-ordered pair, $g_k := t_{\pi(k+\ell)} - t_{\pi(k)} \in \mathbb{R}$, can be negative when the noisy clock inverts sample order; this motivates the even and odd lag-covariance functions in Lemma S2. Finally, define the mean lag-ℓ clock step error $\delta_\pi := \frac{1}{N}\sum_{k=1}^N |g_k - h_k|$ and set $\ell_0 := \min(\ell, N)$.

Lemma S1 (Trajectory covariance under shared and private noise)**.** *Define the stationary OU autocovariance function $\Gamma(h) := e^{Bh}\Sigma$ for $h \ge 0$ and $\Gamma(h) := \Sigma e^{B^\top |h|}$ for $h < 0$. Under Definitions 1 and 2, for any sample indices $a, b \in \{1,\dots,n\}$ and observed snapshots $z_a = x^a_{t_a}, z_b = x^b_{t_b} \in \mathbb{R}^p$, conditioned on (t,τ), we have $\mathbb{E}[z_a \mid t,\tau] = 0$, $\mathbb{E}[z_a z_a^\top \mid t,\tau] = \Sigma$, and $\mathbb{E}[z_a z_b^\top \mid t,\tau] = \rho\,\Gamma(t_a - t_b)$ for all $a \ne b$.*

Proof. Each sample trajectory is a weighted sum of one shared stationary OU process (common to all samples) and one private stationary OU process (independent across samples), so cross-sample covariances ($a \ne b$) retain only the shared trajectory.

Specifically, let y_t solve the stationary OU equation $dy_t = By_t\,dt + A\,dW^0_t$ with $y_0 = z^0 \sim \mathcal{N}(0,\Sigma)$, and for each sample $i \in \{1,\dots,n\}$ let $\tilde{y}^i_t$ solve $d\tilde{y}^i_t = B\tilde{y}^i_t\,dt + A\,d\tilde{W}^i_t$ with $\tilde{y}^i_0 = \tilde{z}^i \sim \mathcal{N}(0,\Sigma)$. By

linearity of the SDE (1) and Definition 1, the linear combination $\sqrt{\rho}\, y_t + \sqrt{1-\rho}\, \tilde{y}_t^i$ has initial state $\sqrt{\rho}\, z^0 + \sqrt{1-\rho}\, \tilde{z}^i = x_0^i$ and driving Brownian motion $\sqrt{\rho}\, W_t^0 + \sqrt{1-\rho}\, \tilde{W}_t^i = W_t^i$. Hence, by uniqueness of strong solutions to linear SDEs, each sample trajectory decomposes as

$$x_t^i = \sqrt{\rho}\, y_t + \sqrt{1-\rho}\, \tilde{y}_t^i.$$

Here y_t and $\tilde{y}_t^1, \ldots, \tilde{y}_t^n$ are mutually independent stationary Gaussian OU processes with marginal law $\mathcal{N}(0, \Sigma)$. For any $0 \le t_b \le t_a$ with $h = t_a - t_b \ge 0$, integrating $dy_t = By_t\, dt + A\, dW_t^0$ gives $y_{t_a} = e^{Bh} y_{t_b} + \int_{t_b}^{t_a} e^{B(t_a - u)} A\, dW_u^0$. Because the stochastic integral has mean zero and is independent of y_{t_b}, the lag-h autocovariance is $\mathbb{E}[y_{t_a} y_{t_b}^\top] = e^{Bh}\mathbb{E}[y_{t_b} y_{t_b}^\top] = e^{Bh}\Sigma = \Gamma(t_a - t_b)$. When $0 \le t_a < t_b$, taking transposes gives $\mathbb{E}[y_{t_a} y_{t_b}^\top] = (\mathbb{E}[y_{t_b} y_{t_a}^\top])^\top = \Sigma e^{B^\top |t_a - t_b|} = \Gamma(t_a - t_b)$.

Evaluating at the snapshot times $z_a = x_{t_a}^a$ gives $\mathbb{E}[z_a] = 0$. When $a = b$, independence of y_{t_a} and $\tilde{y}_{t_a}^a$ gives $\mathbb{E}[z_a z_a^\top] = \rho\, \mathbb{E}[y_{t_a} y_{t_a}^\top] + (1-\rho)\, \mathbb{E}[\tilde{y}_{t_a}^a (\tilde{y}_{t_a}^a)^\top] = \rho\Sigma + (1-\rho)\Sigma = \Sigma$. When $a \ne b$, independence of $\tilde{y}^a$, $\tilde{y}^b$, and y implies that all cross-terms involving the private processes $\tilde{y}^a$ or $\tilde{y}^b$ have expectation zero, leaving only $\mathbb{E}[z_a z_b^\top] = \rho\, \mathbb{E}[y_{t_a} y_{t_b}^\top] = \rho\, \Gamma(t_a - t_b)$. Finally, because the approximate clock τ is conditionally independent of the expression trajectories given t (Definition 2), conditioning on (t, τ) leaves these expectations unchanged. □

Lemma S2 (Lag covariance Taylor regularity and Lipschitz bounds)**.** *For a stationary OU trajectory y_t and lag $h \ge 0$, define the expected symmetric difference covariance $G(h) := \mathbb{E}[(y_{t+h} - y_t)(y_{t+h} - y_t)^\top]$ and antisymmetric lead–lag covariance $H(h) := \mathbb{E}[y_{t+h} y_t^\top - y_t y_{t+h}^\top]$:*

$$G(h) = 2\Sigma - e^{Bh}\Sigma - \Sigma e^{B^\top h}, \qquad H(h) = e^{Bh}\Sigma - \Sigma e^{B^\top h},$$

and extend H to an odd function $\tilde{H}$ on $\mathbb{R}$ by setting $\tilde{H}(h) := -H(-h)$ for $h < 0$. Then:

(i) (First-order Taylor approximation at $h = 0$.) *For all $h \ge 0$, $\|G(h) - h\, AA^\top\|_F \le a_2 h^2$ and $\|H(h) - h(B\Sigma - \Sigma B^\top)\|_F \le a_2 h^2$.*

(ii) (Lipschitz continuity in the time step.) *For all $x, y \in \mathbb{R}$, $\|G(|x|) - G(|y|)\|_F \le 2a_1 |x - y|$ and $\|\tilde{H}(x) - \tilde{H}(y)\|_F \le 2a_1 |x - y|$.*

Proof. Both $G(h)$ and $H(h)$ vanish at $h = 0$, their initial slopes at $h = 0$ are $AA^\top$ and $B\Sigma - \Sigma B^\top$, and their first two derivatives are uniformly bounded for all $h \ge 0$ because B is Hurwitz stable.

Specifically, differentiating $G(h)$ and $H(h)$ with respect to $h \ge 0$ gives

$$G'(h) = -Be^{Bh}\Sigma - \Sigma e^{B^\top h} B^\top, \qquad H'(h) = Be^{Bh}\Sigma - \Sigma e^{B^\top h} B^\top,$$
$$G''(h) = -B^2 e^{Bh}\Sigma - \Sigma e^{B^\top h}(B^\top)^2, \qquad H''(h) = B^2 e^{Bh}\Sigma - \Sigma e^{B^\top h}(B^\top)^2.$$

Evaluating at $h = 0$ and using the Lyapunov equation $B\Sigma + \Sigma B^\top = -AA^\top$ (Eq. (2)) yields $G(0) = H(0) = 0$, $G'(0) = -(B\Sigma + \Sigma B^\top) = AA^\top$, and $H'(0) = B\Sigma - \Sigma B^\top$. For every $h \ge 0$, using $\|M^\top\|_F = \|M\|_F$, the submultiplicative bound $\|XY\|_F \le \|X\|_2 \|Y\|_F$, and $\|e^{Bh}\|_2 \le \kappa$ (Eq. (S1)), we have $\|Be^{Bh}\Sigma\|_F \le \|B\|_2 \kappa \|\Sigma\|_F = a_1$ and $\|B^2 e^{Bh}\Sigma\|_F \le \|B\|_2^2 \kappa \|\Sigma\|_F = a_2$. By the triangle inequality, the first and second derivatives are bounded uniformly across all $h \ge 0$ by

$$\|G'(h)\|_F,\ \|H'(h)\|_F \le 2a_1, \qquad \|G''(h)\|_F,\ \|H''(h)\|_F \le 2a_2.$$

For part (i), applying the integral Taylor remainder $G(h) - G(0) - hG'(0) = \int_0^h (h - s) G''(s)\, ds$ gives

$$\|G(h) - h\, AA^\top\|_F \le \int_0^h (h - s)\|G''(s)\|_F\, ds \le 2a_2 \int_0^h (h - s)\, ds = a_2 h^2,$$

and the identical bound holds for $\|H(h) - h(B\Sigma - \Sigma B^\top)\|_F$. For part (ii), for any $x, y \in \mathbb{R}$, integrating G' between $|y|$ and $|x|$ gives $\|G(|x|) - G(|y|)\|_F = \|\int_{|y|}^{|x|} G'(s)\, ds\|_F \le 2a_1 ||x| - |y|| \le 2a_1 |x - y|$. Similarly, for $s < 0$, the chain rule gives $\tilde{H}'(s) = \frac{d}{ds}[-H(-s)] = H'(-s) = H'(|s|)$. Since $\tilde{H}$ is continuous on $\mathbb{R}$ with $\tilde{H}(0) = 0$ and piecewise smooth with $\|\tilde{H}'(s)\|_F = \|H'(|s|)\|_F \le 2a_1$ for all $s \ne 0$, integrating $\tilde{H}'$ from y to x yields $\|\tilde{H}(x) - \tilde{H}(y)\|_F = \|\int_y^x \tilde{H}'(s)\, ds\|_F \le 2a_1 |x - y|$. □

S1.2 Complete statement and proof of Theorem 1

Theorem 1 (Complete statement). *Under Definitions 1 and 2, conditioned on (t,τ) with distinct clock values ($\theta_1 < \cdots < \theta_n$, so $\Delta > 0$) for arbitrary progression times $0 \le t_1 < \cdots < t_n$:*

(a) (Difference and lead–lag matrices.) *The expected difference and lead–lag matrices satisfy*

$$\begin{aligned}\mathbb{E}[D \mid t,\tau] &= \frac{\rho\bar{h}}{\Delta}\,AA^\top + \frac{2(1-\rho)}{\Delta}\Sigma + \frac{1}{\Delta}E_D = -\frac{\rho\bar{h}}{\Delta}\big(B\Sigma + \Sigma B^\top\big) + \frac{2(1-\rho)}{\Delta}\Sigma + \frac{1}{\Delta}E_D,\\ \mathbb{E}[J \mid t,\tau] &= \frac{\rho\bar{h}}{\Delta}\big(B\Sigma - \Sigma B^\top\big) + \frac{1}{\Delta}E_J,\end{aligned} \tag{S2}$$

where the error matrices E_D and E_J satisfy

$$\|E_D\|_F \le \rho\big(a_2\overline{h^2} + 2a_1\delta_\pi\big), \qquad \|E_J\|_F \le \rho\left(a_2\overline{h^2} + 2a_1\delta_\pi + \frac{4\ell_0\kappa\|\Sigma\|_F}{N}\right). \tag{S3}$$

(b) (Equally spaced true times and Brownian clock displacement.) *If $t_i = t_0 + i\,\delta t$ ($t_0 \ge 0$, $\delta t > 0$) and $\tau_i = v\,t_i + \varepsilon\,W'_{t_i}$ with drift $v > 0$, noise $\varepsilon > 0$, and per-step clock signal-to-noise ratio $\mathrm{SNR} := v^2\delta t/\varepsilon^2$, then $\bar{h} = \ell\,\delta t$, $\overline{h^2} = \ell^2\delta t^2$, and*

$$\mathbb{E}[\delta_\pi \mid t] \le \frac{4n}{N}\,\delta t\,\Psi(\mathrm{SNR}), \qquad \Psi(\mathrm{SNR}) := \sum_{r=1}^{\infty}\Phi\big(-\sqrt{r\,\mathrm{SNR}}\big) \le \frac{1}{2}\,\frac{e^{-\mathrm{SNR}/2}}{1-e^{-\mathrm{SNR}/2}},$$

where Φ denotes the standard normal cumulative distribution function. In particular, the expected clock displacement decays exponentially as SNR *increases:*

$$\mathbb{E}[\delta_\pi \mid t] \le \frac{2n}{N}\,\delta t\,\frac{e^{-\mathrm{SNR}/2}}{1-e^{-\mathrm{SNR}/2}}. \tag{S4}$$

Proof. Throughout the proof we write $\mathbb{E}[\cdot]$ for the conditional expectation $\mathbb{E}[\cdot \mid t,\tau]$. Given (t,τ), the clock sorting permutation π is fixed, so D and J are fixed quadratic forms in the snapshots whose expectations follow from Lemma S1.

Part (a): Expected difference and lead–lag matrices. We proceed in three steps: (1) compute the exact expectation of each lag-ℓ pair, (2) replace the noisy clock-ordered time step g_k by the true step h_k and linearize in h_k, and (3) bound the mean-centering correction in J.

Step 1 (exact pairwise expectations). For the k-th lag-ℓ pair $(a,b) = (\pi(k+\ell), \pi(k))$ ($a \ne b$ since $\ell \ge 1$) with signed true-time gap $g_k = t_a - t_b$, the sample mean $\bar{z}$ cancels in the difference $w_{k+\ell} - w_k = (z_a - \bar{z}) - (z_b - \bar{z}) = z_a - z_b$. Expanding $(z_a - z_b)(z_a - z_b)^\top = z_a z_a^\top + z_b z_b^\top - z_a z_b^\top - z_b z_a^\top$ and applying Lemma S1 gives

$$\begin{aligned}\mathbb{E}\big[(w_{k+\ell} - w_k)(w_{k+\ell} - w_k)^\top\big] &= 2\Sigma - \rho\big(\Gamma(g_k) + \Gamma(-g_k)\big) = 2(1-\rho)\Sigma + \rho\,G(|g_k|),\\ \mathbb{E}\big[z_a z_b^\top - z_b z_a^\top\big] &= \rho\big(\Gamma(g_k) - \Gamma(-g_k)\big) = \rho\,\tilde{H}(g_k).\end{aligned}$$

Notice why private variance affects D but not J: the private variance $2(1-\rho)\Sigma$ enters D through the same-sample terms $z_a z_a^\top$ and $z_b z_b^\top$, whereas $z_a z_b^\top - z_b z_a^\top$ involves only distinct samples $a \ne b$ whose private noise processes are independent and cancel in expectation.

Step 2 (clock-ordering error and Taylor linearization). We now approximate $G(|g_k|)$ and $\tilde{H}(g_k)$ by their linearizations at the true lag-ℓ step $h_k = t_{k+\ell} - t_k > 0$. Because $h_k > 0$, we have $G(h_k) = G(|h_k|)$ and $H(h_k) = \tilde{H}(h_k)$. By the triangle inequality, replacing the noisy step g_k by h_k incurs at most $2a_1|g_k - h_k|$ (Lemma S2(ii)), and replacing $G(h_k)$ and $H(h_k)$ by their tangents $h_k AA^\top$ and $h_k(B\Sigma - \Sigma B^\top)$ incurs at most $a_2 h_k^2$ (Lemma S2(i)):

$$\begin{aligned}\big\|G(|g_k|) - h_k AA^\top\big\|_F &\le \big\|G(|g_k|) - G(h_k)\big\|_F + \big\|G(h_k) - h_k AA^\top\big\|_F \le 2a_1|g_k - h_k| + a_2 h_k^2,\\ \big\|\tilde{H}(g_k) - h_k(B\Sigma - \Sigma B^\top)\big\|_F &\le \big\|\tilde{H}(g_k) - H(h_k)\big\|_F + \big\|H(h_k) - h_k(B\Sigma - \Sigma B^\top)\big\|_F\\ &\le 2a_1|g_k - h_k| + a_2 h_k^2.\end{aligned}$$

Averaging over $k = 1, \dots, N$ and dividing by Δ yields Eq. (S2) for $\mathbb{E}[D]$ with $\|E_D\|_F \le \rho(a_2\overline{h^2} + 2a_1\delta_\pi)$, and gives the same bound for the uncentered version of J.

Step 3 (mean-centering correction in J). In Eq. (4), J is computed from the mean-centered snapshots $w_k = z_{\pi(k)} - \bar{z}$. For $(a, b) = (\pi(k+\ell), \pi(k))$, expanding $(z_a - \bar{z})(z_b - \bar{z})^\top - (z_b - \bar{z})(z_a - \bar{z})^\top$ gives $(z_a z_b^\top - z_b z_a^\top) - (z_a - z_b)\bar{z}^\top + \bar{z}(z_a - z_b)^\top$, because the terms $\bar{z}\bar{z}^\top - \bar{z}\bar{z}^\top = 0$ cancel. Averaging over $k = 1, \dots, N$ leaves

$$\frac{1}{N}\sum_{k=1}^{N}(w_{k+\ell}w_k^\top - w_k w_{k+\ell}^\top) - \frac{1}{N}\sum_{k=1}^{N}(z_{\pi(k+\ell)}z_{\pi(k)}^\top - z_{\pi(k)}z_{\pi(k+\ell)}^\top) = -\frac{1}{N}\big(\zeta\bar{z}^\top - \bar{z}\zeta^\top\big),$$

where $\zeta := \sum_{k=1}^{N}(z_{\pi(k+\ell)} - z_{\pi(k)}) = \sum_{j=\ell+1}^{n} z_{\pi(j)} - \sum_{k=1}^{N} z_{\pi(k)}$. When $\ell \le N$, the overlapping interior indices $\{\ell+1, \dots, N\}$ cancel, leaving $\ell_0 = \ell$ terms in each sum; when $\ell > N$, the two index sets already have size $N = \ell_0$ and are disjoint. In both cases, $\zeta = \sum_{k\in\mathcal{I}_+} z_{\pi(k)} - \sum_{k\in\mathcal{I}_-} z_{\pi(k)}$ over the disjoint sets $\mathcal{I}_+ := \{n - \ell_0 + 1, \dots, n\}$ and $\mathcal{I}_- := \{1, \dots, \ell_0\}$ ($\ell_0 = \min(\ell, N) \le n/2$). Expanding $\bar{z} = \frac{1}{n}\sum_{j=1}^{n} z_j$ gives

$$\mathbb{E}[\zeta\bar{z}^\top] = \frac{1}{n}\sum_{a\in\pi(\mathcal{I}_+)}\sum_{j=1}^{n}\mathbb{E}[z_a z_j^\top] - \frac{1}{n}\sum_{a\in\pi(\mathcal{I}_-)}\sum_{j=1}^{n}\mathbb{E}[z_a z_j^\top].$$

By Lemma S1, the ℓ_0 positive and ℓ_0 negative same-sample ($j = a$) terms equal $+\frac{\ell_0}{n}\Sigma$ and $-\frac{\ell_0}{n}\Sigma$, respectively, and cancel. For every $h \in \mathbb{R}$, we have $\|\Gamma(h)\|_F \le \kappa\|\Sigma\|_F$: this holds directly for $h \ge 0$ since $\|e^{Bh}\Sigma\|_F \le \kappa\|\Sigma\|_F$, and holds for $h < 0$ by symmetry of Σ since $\|\Sigma e^{B^\top|h|}\|_F = \|(e^{B|h|}\Sigma)^\top\|_F = \|e^{B|h|}\Sigma\|_F \le \kappa\|\Sigma\|_F$. Thus each of the remaining $2\ell_0(n-1)$ cross-sample ($j \ne a$) terms $\pm\frac{\rho}{n}\Gamma(t_a - t_j)$ has Frobenius norm at most $\rho\kappa\|\Sigma\|_F/n$. Hence

$$\big\|\mathbb{E}[\zeta\bar{z}^\top - \bar{z}\zeta^\top]\big\|_F \le 2\|\mathbb{E}[\zeta\bar{z}^\top]\|_F \le 2\,\frac{2\ell_0(n-1)}{n}\,\rho\kappa\|\Sigma\|_F \le 4\rho\ell_0\kappa\|\Sigma\|_F,$$

which after dividing by N adds at most $4\rho\ell_0\kappa\|\Sigma\|_F/N$ to $\|E_J\|_F$.

Part (b): Brownian clock displacement. When true snapshot times are equally spaced ($t_i = t_0 + i\,\delta t$), the clock step error δ_π is controlled by the number of pairwise ordering inversions, and an inversion between two samples r steps apart has Gaussian tail probability $\Phi(-\sqrt{r\,\mathrm{SNR}})$.

Step 1 (step error vs. rank displacement). For $t_i = t_0 + i\,\delta t$, the true lag-ℓ step is $h_k = t_{k+\ell} - t_k = \ell\,\delta t$ and the clock-ordered step is $g_k = t_{\pi(k+\ell)} - t_{\pi(k)} = (\pi(k+\ell) - \pi(k))\,\delta t$. Writing $g_k - h_k = \delta t\,\big((\pi(k+\ell) - (k+\ell)) - (\pi(k) - k)\big)$ and applying the triangle inequality gives

$$\delta_\pi = \frac{1}{N}\sum_{k=1}^{N}|g_k - h_k| \le \frac{\delta t}{N}\sum_{k=1}^{N}\big(|\pi(k+\ell) - (k+\ell)| + |\pi(k) - k|\big) \le \frac{2\,\delta t}{N}\sum_{i=1}^{n}|\pi(i) - i|,$$

since each position $i \in \{1, \dots, n\}$ appears at most once as $k + \ell$ and at most once as k.

Step 2 (rank displacement vs. pairwise inversions). Relabeling $a = \pi(i)$ gives $\sum_{i=1}^{n}|\pi(i) - i| = \sum_{a=1}^{n}|\pi^{-1}(a) - a|$, where $\pi^{-1}(a) = 1 + \sum_{b\ne a}\mathbb{I}\{\tau_b < \tau_a\}$ is the sorted rank of sample a. Because $a = 1 + \sum_{b<a} 1 = 1 + \sum_{b<a}(\mathbb{I}\{\tau_b < \tau_a\} + \mathbb{I}\{\tau_b > \tau_a\})$ (with ties having probability zero), subtracting a from $\pi^{-1}(a)$ gives

$$\pi^{-1}(a) - a = \sum_{b>a}\mathbb{I}\{\tau_b < \tau_a\} - \sum_{b<a}\mathbb{I}\{\tau_b > \tau_a\} \quad\Longrightarrow\quad |\pi^{-1}(a) - a| \le \sum_{b>a}\mathbb{I}\{\tau_a > \tau_b\} + \sum_{b<a}\mathbb{I}\{\tau_b > \tau_a\}.$$

Summing over $a = 1, \dots, n$ counts each inverted pair $1 \le j < j' \le n$ with $\tau_j > \tau_{j'}$ twice, yielding $\sum_{a=1}^{n}|\pi^{-1}(a) - a| \le 2\sum_{1\le j<j'\le n}\mathbb{I}\{\tau_j > \tau_{j'}\}$.

Step 3 (expected number of inversions). Under the Brownian clock model (3), for any pair $j < j'$ separated by $r = j' - j \ge 1$ steps, $\tau_{j'} - \tau_j \sim \mathcal{N}(vr\delta t,\, \varepsilon^2 r\delta t)$, so

$$\mathbb{P}(\tau_j > \tau_{j'} \mid t) = \mathbb{P}(\tau_{j'} - \tau_j < 0 \mid t) = \Phi\left(-\frac{vr\delta t}{\sqrt{\varepsilon^2 r\delta t}}\right) = \Phi\big(-\sqrt{r\,\mathrm{SNR}}\big),$$

where $\mathrm{SNR} = v^2\delta t/\varepsilon^2$. Because there are $n - r < n$ pairs at step lag $r \geq 1$, combining Steps 1–3 and summing over $r \geq 1$ gives $\mathbb{E}[\delta_\pi \mid t] \leq \frac{4n}{N}\delta t \sum_{r=1}^{\infty} \Phi(-\sqrt{r\,\mathrm{SNR}}) = \frac{4n}{N}\delta t\,\Psi(\mathrm{SNR})$. Applying $\Phi(-x) \leq \frac{1}{2}e^{-x^2/2}$ $(x > 0)$ and summing the geometric series yields Eq. (S4). □

S1.3 Complete statement and proof of Theorem 2, Remarks S1–S2, and Corollary S1

Theorem 2 (Complete statement).

(a) (Closed-form solution and Hurwitz stability.) *For any $S \succ 0$, symmetric D, and antisymmetric J, the coupled balance equations (6) have the unique solution $\mathcal{B}(S, D, J) := \frac{1}{2}(J - D)S^{-1}$. If $D \succeq 0$, then every eigenvalue ζ of $\mathcal{B}(S, D, J)$ satisfies $\mathrm{Re}\,\zeta \leq 0$; if $D \succ 0$, then $\mathcal{B}(S, D, J)$ is Hurwitz stable.*

(b) (Population target and sign recovery.) *Under Definitions 1 and 2 with $\rho \in (0, 1]$, let $\bar{D} := \mathbb{E}[D \mid t, \tau]$, $\bar{J} := \mathbb{E}[J \mid t, \tau]$, and define the population target*

$$T := \frac{\rho\bar{h}\,B - (1-\rho)I}{\Delta} = s(B - \mu I), \qquad s := \frac{\rho\bar{h}}{\Delta} > 0, \qquad \mu := \frac{1-\rho}{\rho\bar{h}} \geq 0. \tag{S5}$$

Then

$$\left\|\mathcal{B}(\Sigma, \bar{D}, \bar{J}) - T\right\|_F \leq \frac{\rho\,\|\Sigma^{-1}\|_2}{\Delta}\left(a_2\overline{h^2} + 2a_1\delta_\pi + \frac{2\ell_0\kappa\|\Sigma\|_F}{N}\right).$$

The left-hand side is exactly

$$\left\|\mathcal{B}(\Sigma, \bar{D}, \bar{J}) - T\right\|_F = s\,\omega, \qquad \omega := \frac{\|(E_J - E_D)\Sigma^{-1}\|_F}{2\rho\bar{h}}, \tag{S6}$$

where the error level ω (in the units of B) satisfies

$$\omega \leq \bar{\omega} := \frac{\|\Sigma^{-1}\|_2}{\bar{h}}\left(a_2\overline{h^2} + 2a_1\delta_\pi + \frac{2\ell_0\kappa\|\Sigma\|_F}{N}\right).$$

Every off-diagonal entry $i \neq j$ satisfies $|\mathcal{B}(\Sigma, \bar{D}, \bar{J})_{ij}/s - B_{ij}| \leq \omega$; in particular, if $|B_{ij}| > \omega$ (for example, if $|B_{ij}| > \bar{\omega}$), then $\mathrm{sign}\,\mathcal{B}(\Sigma, \bar{D}, \bar{J})_{ij} = \mathrm{sign}\,B_{ij}$. For equally spaced times $t_i = t_0 + i\,\delta t$ $(t_0 \geq 0,\ \delta t > 0)$, we have $\bar{h} = \ell\,\delta t$, $\overline{h^2} = \ell^2\delta t^2$, and $\ell_0 \leq \ell$, so the three sources of error separate as

$$\bar{\omega} \leq \|\Sigma^{-1}\|_2\Big(\underbrace{a_2\,\ell\,\delta t}_{\text{lag } \ell \text{ too long}} + \underbrace{\frac{2a_1\,\delta_\pi}{\ell\,\delta t}}_{\text{clock noise}} + \underbrace{\frac{2\kappa\|\Sigma\|_F}{N\,\delta t}}_{\text{time window too short}}\Big).$$

Proof. Part (a). Adding $XS - SX^\top = J$ and $XS + SX^\top = -D$ cancels $SX^\top$ and gives $2XS = J - D$. Since $S \succ 0$ is invertible, $X = \frac{1}{2}(J - D)S^{-1} = \mathcal{B}(S, D, J)$ is the unique candidate solution. Substituting back into Eq. (6) with $S^\top = S$, $D^\top = D$, and $J^\top = -J$ verifies both equations. For any eigenvalue $\zeta \in \mathbb{C}$ of X with left eigenvector $\xi \in \mathbb{C}^p \setminus \{0\}$, multiplying $XS + SX^\top = -D$ on the left by ξ^* and on the right by ξ gives $-\xi^*D\xi = 2(\mathrm{Re}\,\zeta)\,\xi^*S\xi$, so $\mathrm{Re}\,\zeta = -\xi^*D\xi/(2\xi^*S\xi)$, proving stability.

Part (b). Substituting $(\bar{D}, \bar{J})$ from Eq. (S2) into $\Delta(\bar{J} - \bar{D})$ cancels $\mp\rho\bar{h}\,\Sigma B^\top$:

$$\Delta(\bar{J} - \bar{D}) = \rho\bar{h}\,(B\Sigma - \Sigma B^\top) + \rho\bar{h}\,(B\Sigma + \Sigma B^\top) - 2(1-\rho)\Sigma + E_J - E_D = 2\rho\bar{h}\,B\Sigma - 2(1-\rho)\Sigma + E_J - E_D.$$

Right-multiplying by $\frac{1}{2\Delta}\Sigma^{-1}$ gives $\mathcal{B}(\Sigma, \bar{D}, \bar{J}) = T + \frac{1}{2\Delta}(E_J - E_D)\Sigma^{-1}$. Taking the Frobenius norm and applying Eq. (S3) yields the stated bounds. Since $T_{ij} = sB_{ij}$ for $i \neq j$, we have $|\mathcal{B}(\Sigma, \bar{D}, \bar{J})_{ij}/s - B_{ij}| \leq \omega$, which preserves signs whenever $|B_{ij}| > \omega$. □

Remark S1 (Non-uniform progression speed)**.** Neither Theorem 1(a) nor Theorem 2(b) requires equally spaced progression times $t_1 < \cdots < t_n$. Because $AA^\top$ and $B\Sigma - \Sigma B^\top$ are time-invariant, arbitrary step sizes $h_k = t_{k+\ell} - t_k$ factor into $\bar{h} = \frac{1}{N}\sum_{k=1}^{N} h_k$ and $\overline{h^2} = \frac{1}{N}\sum_{k=1}^{N} h_k^2$. Variations in progression speed therefore alter only the overall positive scale factor $s = \rho\bar{h}/\Delta$, provided $\overline{h^2}/\bar{h}$ remains small.

Remark S2 (The diagonal shift carries over to the penalized estimator)**.** The diagonal shift $-s\mu I$ in Theorem 2(b) also applies to the penalized estimator $\hat{B}(D, J)$ in Algorithm 1 (Eq. (5)): for any $S \succ 0$, $\lambda, r > 0$, and scalar $\varphi \in \mathbb{R}$, $\hat{B}(D + 2\varphi S,\, J) = \hat{B}(D, J) - \varphi I$. This holds because substituting $B' = B - \varphi I$ leaves both quadratic residuals and the off-diagonal penalty $\sum_j \|B_{-j,j}\|_2$ invariant, while s_{unpen} (Eq. (7)) depends on B_{unpen} solely through off-diagonal columns.

Corollary S1 (Steady-state perturbation response and scale-free off-diagonal recovery)**.** *Under a constant perturbation $u \in \mathbb{R}^p$ to Eq. (1), the steady-state mean shift is $\delta\bar{x} = -B^{-1}u$. For $\rho \in (0, 1]$ and $T = s(B - \mu I)$, T is Hurwitz stable and invertible with $-T^{-1} = s^{-1}(\mu I - B)^{-1}$. When $\mu > \|B\|_2$ (small ρ), its convergent Neumann expansion is*

$$-T^{-1} = \frac{1}{s\mu} I + \frac{1}{s\mu^2} B + O(s^{-1}\mu^{-3}) = \frac{\Delta}{1-\rho} I + \frac{\Delta\rho\bar{h}}{(1-\rho)^2} B + O(\rho^2),$$

whose leading off-diagonal term $(s\mu^2)^{-1}\text{offdiag}(B)$ is a positive scalar multiple of $\text{offdiag}(B)$*. Hence, Frobenius normalization of either* $\text{offdiag}(T)$ *or* $(s\mu^2)^{-1}\text{offdiag}(B)$ *eliminates (s, μ) and recovers* $\text{offdiag}(B)/\|\text{offdiag}(B)\|_F$ *exactly.*

Proof. Under $dx_t = (Bx_t + u)\, dt + A\, dW_t$, Hurwitz stability of B drives $\bar{x}_t = \mathbb{E}[x_t]$ to $\delta\bar{x} = -B^{-1}u$. Since $\mu \geq 0$, every eigenvalue of $\mu I - B$ has strictly positive real part, so $-T^{-1} = s^{-1}(\mu I - B)^{-1}$. When $\mu > \|B\|_2$, the bound $\|B/\mu\|_2 < 1$ gives the convergent Neumann series $\mu^{-1}\sum_{k=0}^{\infty}(B/\mu)^k$. Dividing $\text{offdiag}(T)$ or $(s\mu^2)^{-1}\text{offdiag}(B)$ by its Frobenius norm cancels $s > 0$ and $(s\mu^2)^{-1} > 0$. □

S1.4 Uniqueness, scale equivariance, and random-ordering null distribution

Proposition S1 (Uniqueness and scale equivariance of Algorithm 1)**.** *For any $S \succ 0$ and $\lambda, r > 0$, Eq. (5) is strongly convex and admits a unique global solution $\hat{B}$. Moreover, if $\lambda(\beta D, \beta J) = \beta\,\lambda(D, J)$ for all $\beta > 0$, then $\hat{B}(\beta D, \beta J) = \beta\hat{B}(D, J)$, leaving* $\text{offdiag}(\hat{B})/\|\text{offdiag}(\hat{B})\|_F$ *invariant whenever* $\text{offdiag}(\hat{B}) \neq 0$.

Proof. Writing $\lambda_2 = r\lambda > 0$, $\mathcal{L}(B) = \frac{1}{\lambda}\|BS + SB^\top + D\|_F^2 + \frac{1}{\lambda_2}\|BS - SB^\top - J\|_F^2$, and $S = Q\Lambda Q^\top$ ($\Lambda_{ii} \geq \sigma_{\min}(S) > 0$). Setting $\tilde{V} = Q^\top V Q$ and applying $\|M + M^\top\|_F^2 + \|M - M^\top\|_F^2 = 4\|M\|_F^2$ to $M = \tilde{V}\Lambda$ yields $\frac{1}{2}D^2\mathcal{L}(B)[V, V] \geq \frac{4\sigma_{\min}(S)^2}{\max(\lambda, \lambda_2)}\|V\|_F^2$, proving strong convexity and uniqueness. Substituting $B = \beta B'$ when $\lambda(\beta D, \beta J) = \beta\lambda(D, J)$ factors $\beta > 0$ out of the entire objective. □

Proposition S2 (Zero expected directed signal under random sample orderings)**.** *For any fixed snapshot matrix $Z = (z_1, \ldots, z_n)$ ($n \geq 3$) with $S \succ 0$ and fixed phase grid θ ($\Delta > 0$), if π is drawn uniformly at random from all $n!$ permutations independently of Z, then*

$$\mathbb{E}[J \mid Z] = 0, \qquad \mathbb{E}[D \mid Z] = \frac{2}{\Delta} S, \qquad \mathbb{E}\big[\mathcal{B}(S, D, J) \mid Z\big] = -\frac{1}{\Delta} I. \tag{S7}$$

Proof. Let $u_a = z_a - \bar{z}$ ($\sum_a u_a = 0$, $\sum_a u_a u_a^\top = (n-1)S$). Under uniform π, $\mathbb{E}[w_k w_k^\top \mid Z] = \frac{n-1}{n} S$, and each distinct pair $(\pi(k+\ell), \pi(k))$ is uniform over $a \neq b$, giving $\mathbb{E}[w_{k+\ell} w_k^\top \mid Z] = \frac{1}{n(n-1)}\sum_{a \neq b} u_a u_b^\top = -\frac{1}{n} S$. Symmetry of S yields $\mathbb{E}[J \mid Z] = 0$, $\mathbb{E}[D \mid Z] = \frac{2}{\Delta} S$, and $\mathbb{E}[\mathcal{B}(S, D, J) \mid Z] = -\frac{1}{\Delta} I$. □

S1.5 Supplementary technical notes on synthetic sweeps, pseudo-bulk recovery, and first-order Neumann proxy

S1.5.1 Synthetic and U2OS pseudo-bulk diagnostics (Tables S1–S3)

In Tables S1 and S2, self-calibrated regularization ($c_{\text{mult}} = 1.0$) selects a stable active regulator count (4.95–6.15 of 10 columns in clock-ordered fits versus 4.95–6.16 in random-order fits) across all 21 regimes. Varying $c_{\text{mult}} \in \{0.5, \ldots, 2.5\}$ preserves a 12/12 single-cell pass rate (84.7%–92.6% mean sign accuracy) and 3/3 pass rate under tight (0.3 rad) bulk synchrony (Table S10). In Table S3, averaging 100 U2OS cells per pseudo-bulk biopsy reduces sample-level clock noise so that transcriptomic clock ordering matches experimental FUCCI fluorescence ordering across all six settings on the candidate panel ($r = 0.300$–0.318 vs. 0.296–0.313 at 0.3 rad; $r = 0.317$–0.366 vs. 0.315–0.367 at 1.0 rad). Both orderings exceed the random-order 95th percentile (0.051–0.057) by five- to six-fold.

Remark S3 (First-order Neumann justification for $S_g^{(c)}$ and $\chi^{(c)} = S_t^{(c)} - S_h^{(c)}$)**.** Decomposing each fitted bulk matrix as $\hat{B}_g = \mathcal{D}_g + O_g$ with strictly negative diagonal $\mathcal{D}_g = \text{diag}(\hat{B}_g)$ and off-diagonal part $O_g = \text{offdiag}(\hat{B}_g)$. Whenever the spectral radius of $\mathcal{D}_g^{-1} O_g$ is strictly below 1 (verified across all four bulk cohorts in Table S9: 0.320–0.747), the steady-state response matrix expands as $-\hat{B}_g^{-1} = -\mathcal{D}_g^{-1} + \mathcal{D}_g^{-1} O_g \mathcal{D}_g^{-1} + \sum_{k=2}^{\infty} (-\mathcal{D}_g^{-1} O_g)^k (-\mathcal{D}_g^{-1})$. Because $\hat{B}_{g,ii}\hat{B}_{g,jj} > 0$, each (i, j) entry $\hat{B}_{g,ij}/(\hat{B}_{g,ii}\hat{B}_{g,jj})$ of the leading off-diagonal term $\mathcal{D}_g^{-1} O_g \mathcal{D}_g^{-1}$ shares the exact sign of $\hat{B}_{g,ij}$ and $\tilde{B}_{g,ij}$ ($r = 0.793$–0.954 with $\text{offdiag}(-\hat{B}_g^{-1})$ in Table S9). Thresholding $\tilde{B}_g^{(c)}$ into $S_g^{(c)}$ (Eq. (9)) therefore provides a scale-invariant first-order proxy $S_h^{(2)} u$ for healthy off-diagonal steady-state perturbation and $\Delta B_{\text{rect}} u$ for the shared difference in steady-state response between tumor and healthy networks.

S2 Supplementary Figures (Figures S1–S3)

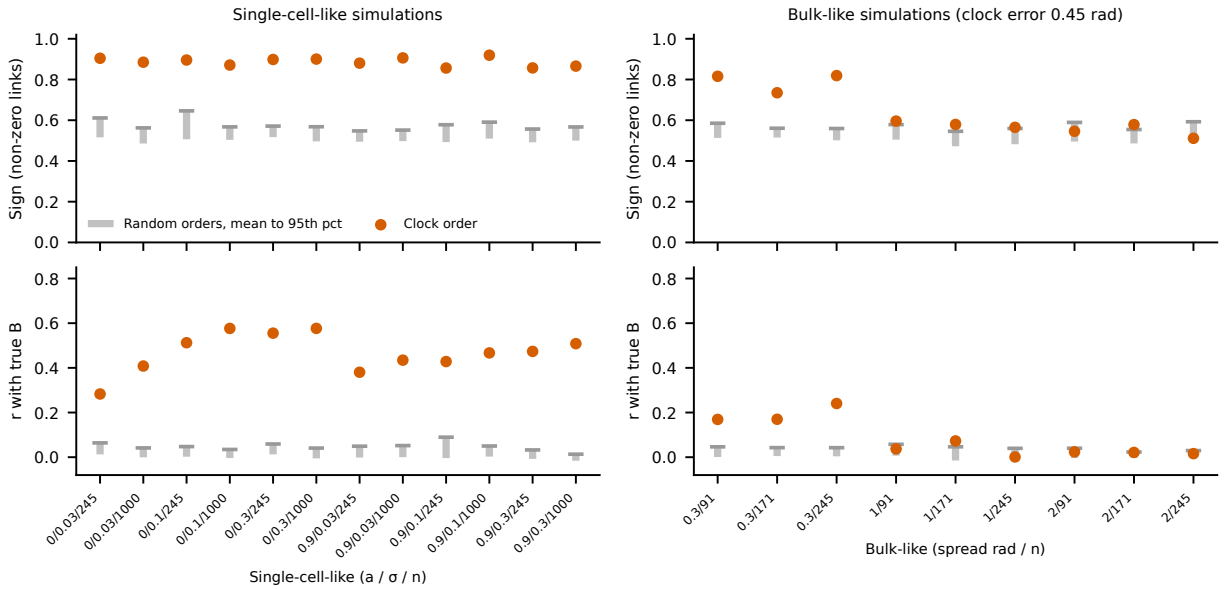


Figure S1: **Synthetic network recovery from noisy clock orderings across 21 single-cell and bulk phase-dispersion regimes, related to Figure 1 and Methods.** Non-zero off-diagonal sign accuracy (top) and off-diagonal Pearson correlation r with the true 8-gene target matrix B (bottom) for clock-ordered fits ($\sigma_{\text{clock}} = 0.45$ rad, orange circles) versus the range from the mean to the 95th percentile of 20 uniform random orderings per replicate (grey bars), across 20 independent replicates. Left: 12 unpooled single-cell settings varying progression-speed heterogeneity $a \in \{0, 0.9\}$, diffusion noise $\sigma \in \{0.03, 0.1, 0.3\}$, and cohort size $n \in \{245, 1{,}000\}$. Right: 9 pooled 100-cell bulk settings with circular phase spread 0.3, 1.0, or 2.0 rad across $n \in \{91, 171, 245\}$. Complete numerical summaries are provided in Tables S1 and S2.

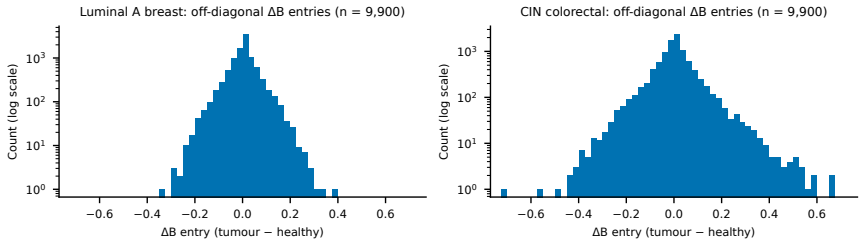


Figure S2: **Raw off-diagonal differences between tumor and healthy networks prior to Frobenius scale normalization, related to Figure 4 and Methods.** Histograms of all 9,900 off-diagonal entries of $\hat{B}_t^{(c)} - \hat{B}_h^{(c)}$ across $[-0.75, 0.75]$ in LumA breast cancer (5,242 entries within $[-0.025, 0.025]$; off-diagonal Frobenius norms 4.81 healthy vs. 2.98 tumor) and CIN colorectal cancer (4,186 entries within $[-0.025, 0.025]$; wider tails $[-0.725, 0.675]$ reflecting off-diagonal Frobenius norms 8.43 healthy colon vs. 3.05 CIN tumor). These scale differences motivate the scale-invariant normalization in Eq. (8).

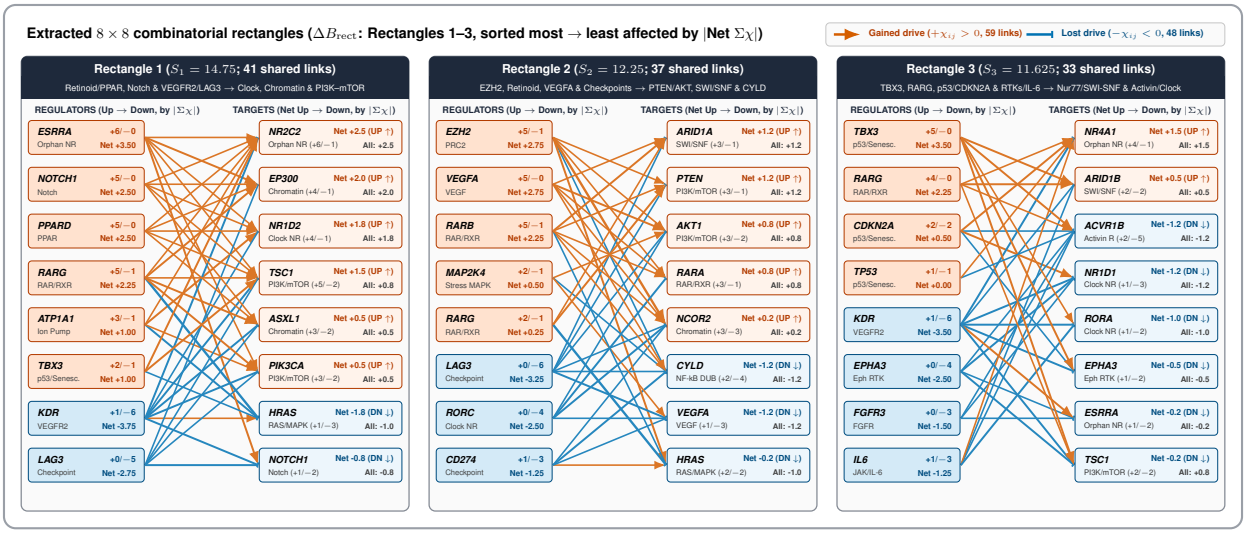


Figure S3: **Bipartite graphs of the three 8×8 biclusters comprising the 107-link shared subnetwork ΔB_{rect}, related to Figure 4.** The constituent biclusters are Rectangle 1 ($S_1 = 14.75$, 41 shared same-sign links), Rectangle 2 ($S_2 = 12.25$, 37 links), and Rectangle 3 ($S_3 = 11.625$, 33 links). Four links overlap across rectangles, giving 107 unique shared links across 19 upstream regulators and 22 downstream targets at $\epsilon = 2.0\, m_h$. Regulators (left) and targets (right) are grouped by net shift sign ($\Sigma\chi \geq 0$, orange; $\Sigma\chi < 0$, blue) and ordered by $|\text{Net } \Sigma\chi|$. Orange arrows denote $\Delta B_{\text{rect},ij} > 0$ and blue T-bars denote $\Delta B_{\text{rect},ij} < 0$.

S3 Supplementary Tables (Tables S1–S11)

Table S1: **Network recovery in unpooled single-cell synthetic simulations across 12 combinations of oscillator speed (a), dynamical noise (σ), and sample size (n) at $c_{\text{mult}} = 1.0$, related to Figure 1, Figure S1, and Methods.** Clock-ordered estimates met both pre-declared criteria in all 12 settings: non-zero sign accuracy (sign_{nz}) exceeded the random-order mean by ≥ 0.10 (random-order 95th percentile 0.548–0.646), and off-diagonal correlation (r) exceeded the random-order 95th percentile (0.013–0.090). Unpenalized r was 0.088–0.518, vs. an unpenalized random-order 95th percentile of 0.020–0.062. Rightmost column reports mean active off-diagonal column count (out of 10) for clock-ordered (and random-order) fits.

a	σ	n	sign (nz)	rand sign (nz), mean (95th)	sign (all)	rand sign (all), mean (95th)	r	unpen r	rand r, 95th pct	active cols (rand)
0	0.03	245	0.904	0.516 (0.611)	0.518	0.290 (0.390)	0.283	0.111	0.064	5.05 (4.95)
0	0.03	1000	0.885	0.486 (0.562)	0.544	0.278 (0.378)	0.408	0.206	0.042	5.35 (5.07)
0	0.1	245	0.896	0.507 (0.646)	0.568	0.309 (0.402)	0.513	0.324	0.048	5.25 (5.44)
0	0.1	1000	0.871	0.504 (0.567)	0.575	0.292 (0.380)	0.577	0.470	0.035	4.95 (5.35)
0	0.3	245	0.898	0.517 (0.571)	0.591	0.345 (0.466)	0.555	0.441	0.059	5.80 (5.99)
0	0.3	1000	0.900	0.496 (0.568)	0.611	0.323 (0.420)	0.577	0.518	0.041	5.85 (5.99)
0.9	0.03	245	0.880	0.494 (0.548)	0.601	0.320 (0.443)	0.380	0.088	0.049	5.35 (5.31)
0.9	0.03	1000	0.906	0.497 (0.552)	0.620	0.313 (0.379)	0.434	0.212	0.052	5.55 (5.19)
0.9	0.1	245	0.856	0.493 (0.578)	0.599	0.307 (0.436)	0.428	0.247	0.090	5.90 (5.31)
0.9	0.1	1000	0.919	0.510 (0.591)	0.611	0.326 (0.452)	0.467	0.400	0.050	5.45 (5.37)
0.9	0.3	245	0.857	0.492 (0.557)	0.607	0.323 (0.409)	0.474	0.379	0.033	6.15 (6.12)
0.9	0.3	1000	0.866	0.500 (0.567)	0.558	0.332 (0.410)	0.508	0.468	0.013	5.75 (6.16)

Table S2: **Network recovery in pooled 100-cell bulk synthetic simulations at $c_{\text{mult}} = 1.0$, related to Figure 1, Figure S1, and Methods.** Each sample averages 100 cells drawn with circular phase spread 0.3, 1.0, or 2.0 rad. Clock-ordered estimates exceeded the 95th-percentile random-order threshold on off-diagonal correlation (r) in all 3 tight-spread (0.3 rad) settings and in 4 of 9 settings overall (adding 1.0 rad at $n = 171$). They exceeded it in 7 of 9 settings for non-zero sign accuracy (0.3 rad and 1.0 rad across all $n \in \{91, 171, 245\}$, plus 2.0 rad at $n = 171$).

spread (rad)	n	sign (non-zero links)	threshold	r	threshold	active cols (rand)
0.3	91	0.816	0.585	0.169	0.046	5.60 (5.16)
0.3	171	0.735	0.561	0.170	0.043	5.10 (5.22)
0.3	245	0.819	0.559	0.240	0.043	5.35 (5.29)
1.0	91	0.596	0.578	0.037	0.058	5.60 (5.56)
1.0	171	0.579	0.546	0.073	0.047	5.80 (5.74)
1.0	245	0.565	0.559	0.001	0.040	6.15 (5.80)
2.0	91	0.546	0.589	0.024	0.040	5.35 (5.70)
2.0	171	0.578	0.554	0.021	0.023	6.05 (6.05)
2.0	245	0.511	0.593	0.016	0.030	6.05 (6.02)

Table S3: **Recovery of the single-cell U2OS network from 100-cell pseudo-bulk profiles at $c_{\text{mult}} = 1.0$, related to Figure 2.** Across 10 random U2OS splits (429 clock-training and 430 pseudo-bulk test cells per split), clock-ordered pseudo-bulk networks (100 cells per sample, spread 0.3 or 1.0 rad) beat the 95th percentile of 100 random orders. They did so in 8–10 of 10 splits on the 20 strongest cycle-phase genes (10/10 in 5 of 6 settings) and in 10/10 splits across all 6 settings on 100 stratified 20-gene subsets from the 157 U2OS-expressed candidate genes, passing 12/12 benchmark settings (gene sets listed in Table S8).

genes	spread	n	clock r	true-order r	random r mean / 95th	clock sign (rand 95th)	splits
cycle-phase (20)	0.3	91 / 171 / 245	0.637 / 0.621 / 0.628	0.589 / 0.619 / 0.610	−0.002 to 0.003 / 0.297–0.313	0.813 / 0.811 / 0.823 (0.713–0.722)	10 / 10 / 10
candidate panel (100 × 20)	0.3	91 / 171 / 245	0.300 / 0.312 / 0.318	0.296 / 0.308 / 0.313	≈0 / 0.051–0.054	0.602 / 0.604 / 0.604 (0.529–0.530)	10 / 10 / 10
cycle-phase (20)	1.0	91 / 171 / 245	0.604 / 0.713 / 0.709	0.634 / 0.745 / 0.742	−0.022 to 0.019 / 0.389–0.431	0.850 / 0.928 / 0.900 (0.800–0.849)	10 / 8 / 10
candidate panel (100 × 20)	1.0	91 / 171 / 245	0.317 / 0.356 / 0.366	0.315 / 0.353 / 0.367	≈0 / 0.056–0.057	0.583 / 0.587 / 0.590 (0.527–0.529)	10 / 10 / 10

Table S4: **Empirical permutation p-values for clock-ordered bulk networks ($\hat{B}_g$, $c_{\text{mult}} = 1.0$) against 1,000 random sample orderings across 42 external tests, related to Figure 3.** 14/42 tests reach $p \leq 0.10$ (binomial $p = 8.4 \times 10^{-5}$; 9/24 in the two carcinoma cohorts, $p = 2.8 \times 10^{-4}$). Curated sign agreement is scored on non-zero fitted links (nz) and across all curated links with zeros counted as wrong (zw); *auxiliary MCF7 L1000 knockdown scores for healthy breast.

comparison	LumA	CIN	healthy breast	healthy colon
knock-down response, 24 directly measured L1000 genes (96 h, primary)	0.261	0.004	0.720*	0.411
knock-down response, 93 panel genes (96 h, secondary)	0.122	0.001	0.656*	0.675
copy-number response (primary)	0.631	0.874	–	–
copy-number response, Spearman	0.399	0.996	–	–
sign, OmniPath (nz / zw)	0.003 / 0.042	0.102 / 0.088	0.469 / 0.484	0.519 / 0.901
sign, CollecTRI supported (nz / zw)	0.186 / 0.319	0.643 / 0.623	0.186 / 0.703	0.020 / 0.051
sign, CollecTRI all (nz / zw)	0.090 / 0.158	0.721 / 0.715	0.828 / 0.957	0.011 / 0.070
sign, restricted set (nz / zw)	0.073 / 0.177	0.025 / 0.024	0.209 / 0.070	0.986 / 0.998

Table S5: **Cross-cancer link overlap and bicluster extraction across thresholds $\epsilon \in \{1.5, 2.0, 2.5\}\, m_h$ and rectangle sizes $k_{\text{rect}} \in \{3, 5, 8\}$ benchmarked against 1,000 CIN gene-label permutations, related to Figure 4.** Here m_h is the median non-zero healthy off-diagonal magnitude, $|\mathcal{A}_c| = |\{(i,j) : \chi_{ij}^{(c)} \neq 0\}|$ is the count of links with altered sign in cancer c, and S_t is the round-t bicluster concordance score.

Cutoff / rectangle size	Requirement / metric	$\lvert\mathcal{A}_{\text{LumA}}\rvert$, $\lvert\mathcal{A}_{\text{CIN}}\rvert$	Observed	Analytical	Null mean	Null 95th pct	p
$\epsilon = 1.5\, m_h$	altered, any sign	3,934, 4,449	1,950	1,767.9	1,768.2	1,879.0	0.005
$\epsilon = 1.5\, m_h$	altered, same sign	3,934, 4,449	985	884.0	884.6	971.0	0.026
$\epsilon = 2.0\, m_h$ (main)	altered, any sign	3,148, 3,575	1,339	1,136.8	1,139.1	1,237.0	0.001
$\epsilon = 2.0\, m_h$ (main)	altered, same sign	3,148, 3,575	663	568.4	569.2	643.0	0.014
$\epsilon = 2.0\, m_h$ (main)	exact transition (disappear 139, appear 172, flip 2)	3,148, 3,575	313	–	244.2	297.0	0.016
$\epsilon = 2.0\, m_h$ (40 cols, 40-col perm)	altered, any sign ($N = 3{,}960$ links)	1,792, 1,878	852	849.8	850.2	895.0	0.484
$\epsilon = 2.0\, m_h$ (40 cols, 40-col perm)	altered, same sign ($N = 3{,}960$ links)	1,792, 1,878	472	424.9	425.7	472.0	0.054
$\epsilon = 2.5\, m_h$	altered, any sign	2,448, 2,817	835	696.6	699.6	782.0	0.007
$\epsilon = 2.5\, m_h$	altered, same sign	2,448, 2,817	410	348.3	349.9	409.0	0.050
Rectangles $k_{\text{rect}} = 3$ ($\epsilon = 2.0\, m_h$)	3-round union: 26 same-sign links (S_1 / $\sum_{t=1}^{3} S_t$)	$9 + 9 + 8$ links	4.00 / 11.25	–	4.10 / 11.26	5.00 / 13.50	0.630 / 0.484
Rectangles $k_{\text{rect}} = 5$ ($\epsilon = 2.0\, m_h$)	3-round union: 57 same-sign links (S_1 / $\sum_{t=1}^{3} S_t$)	$20 + 19 + 18$ links	8.00 / 21.75	–	7.61 / 20.80	9.25 / 24.75	0.349 / 0.294
Rectangles $k_{\text{rect}} = 8$ (main ΔB_{rect})	3-round union: 107 same-sign links (S_1 / $\sum_{t=1}^{3} S_t$)	$41 + 37 + 33$ links	14.75 / 38.625	–	13.16 / 35.16	16.25 / 41.13	0.148 / 0.131

Table S6: **Cross-cancer outgoing regulatory shift concordance ($\Delta\tilde{B}_{\cdot,G}^{(c)} = \tilde{B}_{t,\cdot,G}^{(c)} - \tilde{B}_{h,\cdot,G}^{(c)}$) across the 20 clinical drug-mechanism families and two reference groups, related to Figure 4.** Columns report gene count $|G|$, panel genes, mean outgoing shift $\mu_G^{(c)}$ ($\times 10^{-3}$), signed-product permutation p_{prod}, outgoing profile correlation r_G, one-sided permutation p_{corr}, Benjamini–Hochberg q_{20} (q_{22}), and fraction of outgoing links with altered sign at $\epsilon = 2.0\, m_h$ [33, 34].

ID	Mechanism axis / group	$\lvert G\rvert$	Panel genes	μ_{LumA}	μ_{CIN}	p_{prod}	r_G	p_{corr}	q_{20} (q_{22})	alt^{LumA}	alt^{CIN}
1	EGFR/HER (ERBB) inhibitors	3	*EGFR, ERBB2, ERBB3*	2.37	−1.70	0.712	−0.073	0.771	1.000 (1.000)	0.128	0.404
2	VEGF/VEGFR anti-angiogenics	4	*VEGFA, KDR, FLT1, FLT4*	9.92	−1.74	0.772	0.201	0.032	0.120 (0.132)	0.543	0.480
3	FGFR inhibitors	3	*FGFR1, FGFR2, FGFR3*	−3.81	−0.31	0.435	−0.051	0.818	1.000 (1.000)	0.337	0.135
4	KIT/CSF1R (PDGFR) inhibitors	2	*KIT, CSF1R*	0.02	1.64	0.327	−0.113	0.943	1.000 (1.000)	0.157	0.202
5	MET inhibitors	1	*MET*	2.81	0.00	0.591	0.000	0.533	0.970 (1.000)	0.232	0.000
6	IGF1R inhibitors (clinical)	1	*IGF1R*	−1.08	−1.26	0.339	0.196	0.027	0.120 (0.132)	0.182	0.273
7	RAS–RAF (MAPK) inhibitors	5	*KRAS, HRAS, BRAF, RAF1, ARAF*	0.81	−1.75	0.822	−0.047	0.784	1.000 (1.000)	0.216	0.446
8	PI3K–AKT–mTOR inhibitors	6	*PIK3CA, PIK3R1, AKT1, AKT2, AKT3, MTOR*	−4.43	3.64	0.910	0.152	0.069	0.197 (0.217)	0.335	0.414
9	CDK4/6 inhibitors	2	*CDK4, CDK6*	6.03	2.73	0.250	0.069	0.232	0.579 (0.637)	0.419	0.212
10	JAK–STAT / IL-6 inhibitors	3	*JAK1, JAK2, IL6*	0.23	−5.43	0.972	−0.056	0.823	1.000 (1.000)	0.242	0.343
11	Immune checkpoint inhibitors	2	*CD274, LAG3*	−8.76	−8.16	0.010	0.177	0.036	0.120 (0.132)	0.576	0.591
12	HDAC inhibitors	2	*HDAC1, HDAC2*	1.96	4.86	0.105	−0.240	0.998	1.000 (1.000)	0.540	0.293
13	EZH2 / DNMT inhibitors	2	*EZH2, DNMT3A*	−7.06	6.97	0.942	0.187	0.007	0.070 (0.077)	0.646	0.556
14	Topoisomerase I inhibitors	1	*TOP1*	0.00	2.64	1.000	0.000	1.000	1.000 (1.000)	0.000	0.303
15	Retinoid (RAR/RXR) agonists	5	*RARA, RARB, RARG, RXRA, RXRB*	2.51	0.79	0.417	0.185	0.029	0.120 (0.132)	0.277	0.339
16	PPAR agonists	3	*PPARA, PPARD, PPARG*	1.30	−0.50	0.637	0.296	0.002	0.040 (0.044)	0.279	0.532
17	Corticosteroid modulators	2	*NR3C1, NR3C2*	2.29	0.00	0.575	0.000	0.468	0.935 (1.000)	0.101	0.000
18	THR / VDR agonists	3	*THRA, THRB, VDR*	10.42	−4.84	0.946	0.080	0.320	0.710 (0.781)	0.414	0.438
19	HIF-2α inhibitors	1	*EPAS1*	0.00	−1.83	1.000	0.000	1.000	1.000 (1.000)	0.000	0.071
20	Other druggable receptors / pumps	7	*NOTCH1, ATP1A1, CACNA1D, ACVR1B, ACVR2A, EPHA3, EPHB4*	3.11	3.67	0.068	−0.235	0.998	1.000 (1.000)	0.430	0.391
21	Tumor suppressors & adaptors	26	*AFDN, ARID1A/B, ASXL1, ATM, BIRC6, CCDC6, CDKN2A, CYLD, EML4, EP300, ETV1, FBXW7, GNAS, KMT2C, MAP2K4, MAP3K1, MYH9, NCOR2, NF1, PTEN, SETDB1, SMAD4, TBX3, TP53, TSC1*	−1.26	1.27	0.802	−0.144	1.000	– (1.000)	0.264	0.340
22	Orphan nuclear receptors	16	*ESRRA, NR1D1/2, NR1H2/3, NR2C1/2, NR2F1/2/6, NR4A1–3, NR5A2, RORA/C*	1.69	−0.42	0.710	−0.027	0.639	– (1.000)	0.361	0.393

Table S7: Complete class-level parameter summary of top drug-combination rankings on ΔB_{rect} and clinical/preclinical context, related to Figure 5 and Table 1. The single-drug baseline has $\alpha = 1.000$, $c = 0$, and ratio 1.000. Columns report backbone weight α, partner weight c, subnetwork residual ratio $r^\star$ (with full $\chi^{(2)}$ ratio and top-20 opposition sign match in parentheses), and rank-1 permutation $p_{\text{net}}/p_{\text{push}}$.

Backbone ($k_{\text{drug}} = 0$: $\alpha = 1.000$, ratio 1.000)	Partner drug class (listed compounds match rows 1-to-1)	α (c)	ΔB_{rect} ratio (full; sign)	Literature context (tumor type and setting)
palbociclib (CDK4/6) LumA→CIN (myelo.) $p_{\text{net/push}}$=0.067/0.082 (rep 0.087/0.139)	TP53 stabilizer (*eprenetapopt* [Ph3])	0.604 (0.604)	0.563 (0.672; 0.70)	Mutant-TP53 reactivation studied preclinically in solid tumors and in Phase Ib/II MDS/AML [85, 86].
	EGFR / FGFR / VEGFR (*erlotinib*, *gefitinib*, *infigratinib*, *orantinib* [Ph3])	0.553 (0.553) 0.618 (0.618) 0.584 (0.584) 0.995 (0.109)	0.832 (1.010; 0.45) 0.844 (1.025; 0.40) 0.918 (0.767; 0.15) 0.994 (0.978; 0.65)	Preclinical: FGFR1 amplification and EGFR-family signaling linked to CDK4/6-inhibitor resistance in breast cancer [11, 70, 71]; *palbociclib* + *cetuximab* showed mixed results in Phase II (head and neck [72, 73]; mCRC primary endpoint not met [74]).
	PPARα / VDR / RAR agonist (*gemfibrozil*, *calcifediol*, *fenofibrate*, *tretinoin*)	0.591 (0.578) 0.706 (0.706) 0.688 (0.688) 0.553 (0.553)	0.633 (0.913; 0.65) 0.747 (0.674; 0.70) 0.759 (0.893; 0.80) 0.788 (0.950; 0.30)	High-dose vitamin D_3 with chemotherapy in mCRC (Phase II SUNSHINE; primary PFS comparison not significant [75]); PPAR and retinoid-receptor biology [38, 39].
pictilisib (PI3K proxy) LumA→CIN (non-myelo.) $p_{\text{net/push}}$=0.684/0.830 (rep 0.748/0.920)	HDAC / FGFR / JAK / TP53 (*tacedinaline* [Ph3], *dovitinib* [Ph3], *ruxolitinib* [Ph4 hem.], *eprenetapopt* [Ph3], *infigratinib*)	0.530 (0.530) 0.562 (0.562) 0.580 (0.580) 0.765 (0.765) 0.633 (0.633)	0.745 (0.571; 0.25) 0.758 (0.558; 0.50) 0.798 (0.579; 0.45) 0.822 (0.602; 0.60) 0.825 (0.657; 0.50)	PI3K inhibitors with endocrine therapy in ER$^+$ breast cancer [63, 106]; feedback RTK reactivation under PI3K–mTOR blockade [10, 41]; PI3K/mTOR + HDAC tested only in Phase I [76]; colon combinations untested clinically.
	PPARα / RAR / VDR / THR (*gemfibrozil*, *tretinoin*, *doxercalciferol*, *levothyroxine*)	0.561 (0.561) 0.533 (0.533) 0.658 (0.441) 0.907 (0.762)	0.826 (0.712; 0.40) 0.853 (0.666; 0.25) 0.870 (0.690; 0.40) 0.888 (0.941; 0.75)	Exploratory nuclear-receptor co-targeting of Rectangle-1/2 *RARG*/*PPARD*/*PIK3CA* links.
everolimus (mTORC1) LumA→CIN (non-myelo.) $p_{\text{net/push}}$=0.457/0.098 (rep 0.511/0.126)	TP53 / EGFR / HDAC / RTK (*eprenetapopt* [Ph3], *gefitinib*, *entinostat* [Ph3], *masitinib* [Ph3], *neratinib*)	0.584 (0.490) 0.728 (0.551) 0.598 (0.598) 0.929 (0.292) 0.889 (0.285)	0.696 (0.832; 0.50) 0.724 (1.076; 0.55) 0.781 (0.917; 0.35) 0.903 (1.200; 0.70) 0.938 (1.144; 0.60)	Preclinical feedback RTK/AKT reactivation under mTOR inhibition [10]; Phase II everolimus + VEGFR TKI tivozanib in refractory mCRC (no responses) [77] and + erlotinib in lung cancer (efficacy threshold not met) [78]; Phase I everolimus + VEGFR TKIs [79, 80]; mTOR + HDAC Phase I only [76].
	RAR / PPARα / VDR agonist (*tretinoin*, *fenofibrate*, *calcifediol*)	0.668 (0.668) 0.727 (0.470) 0.880 (0.249)	0.711 (1.149; 0.60) 0.797 (0.855; 0.65) 0.954 (0.877; 0.35)	Exploratory retinoid, fibrate, and vitamin D pairings with mTORC1 blockade [38].
irinotecan (& metab., TOP1) CIN→LumA (myelo.) $p_{\text{net/push}}$=0.137/0.063 (rep 0.198/0.092)	TP53 / EGFR / MET / IGF1R (*eprenetapopt* [Ph3], *gefitinib*, *tivantinib* [Ph3], *crizotinib*, *linsitinib* [Ph3])	0.560 (0.560) 0.592 (0.592) 0.631 (0.631) 0.680 (0.680) 0.633 (0.633)	0.593 (0.774; 0.65) 0.696 (1.005; 0.55) 0.785 (1.229; 0.55) 0.869 (0.684; 0.50) 0.879 (0.984; 0.45)	Irinotecan + EGFR antibody improved outcomes in mCRC (Phase III and randomized Phase II [43, 44, 81]; control arm of SWOG S1406 [83]); irinotecan + cetuximab + tivantinib (MET) missed its randomized Phase II primary endpoint [84]; untested in LumA breast cancer; active metab. ratio 0.653 (p_{net}=0.228/0.309, p_{push}=0.072/0.133).
	PPAR / 5-ASA / VDR agonist (*fenofibrate*, *gemfibrozil*, *balsalazide*, *calcifediol*)	0.789 (0.549) 0.629 (0.629) 0.623 (0.566) 0.621 (0.579)	0.763 (0.935; 0.65) 0.769 (0.960; 0.60) 0.845 (0.962; 0.45) 0.859 (0.766; 0.50)	Untested nuclear-receptor pairings with TOP1 chemotherapy for LumA breast translation.
topotecan (TOP1 proxy) CIN→LumA (myelo.) $p_{\text{net/push}}$=0.210/0.412 (rep 0.263/0.608)	TP53 / JAK / VEGFR / FGFR / MET (*eprenetapopt* [Ph3], *ruxolitinib* [Ph4 hem.], *linifanib* [Ph3], *infigratinib*, *crizotinib*)	0.664 (0.664) 0.621 (0.621) 0.737 (0.626) 0.609 (0.609) 0.536 (0.536)	0.662 (0.855; 0.65) 0.695 (1.036; 0.55) 0.790 (0.724; 0.50) 0.819 (0.852; 0.55) 0.824 (0.706; 0.25)	Topotecan + EGFR/HER2 inhibitor lapatinib studied preclinically and in Phase I [107]; irinotecan-based chemotherapy + VEGF-pathway antibodies or aflibercept improved survival in mCRC (Phase III [45, 46, 82]) but has not been tested with linifanib; no TOP1 + JAK-inhibitor trials; non-myelosuppressive partners cancel 17.6–33.8% of $\Delta B_{\text{rect}} u_R$ (repurposing: *gemfibrozil* 0.714, *doxercalciferol* 0.785, *tretinoin* 0.790).

Table S8: Functional classification of the 11-gene cell-cycle clock, the 100-gene bulk network panel (Bulk), and the 200-gene extended candidate pool (Bulk + Ext.) across 12 classes, related to Figures 1–5 and Methods.

Functional class (total; bulk/ext.)	HGNC gene symbols (**Bulk**: 100-gene bulk panel; **Ext.**: +100 extended pool)
Cell-cycle clock [29–31] (11; clock only)	*CCNA2, CCNB1, CCNB2, CCND1, CCND2, CCND3, CCNE1, CCNE2, CDK1, TOP2A, UBE2C*
Nuclear hormone receptors [35, 38, 39, 75] (29; 29/0)	**Bulk (29):** *ESRRA, NR1D1, NR1D2, NR1H2, NR1H3, NR2C1, NR2C2, NR2F1, NR2F2, NR2F6, NR3C1, NR3C2, NR4A1, NR4A2, NR4A3, NR5A2, PPARA, PPARD, PPARG, RARA, RARB, RARG, RORA, RORC, RXRA, RXRB, THRA, THRB, VDR*
Non-receptor transcription factors [54, 60, 85, 100] (15; 5/10)	**Bulk (5):** *EPAS1, ETV1, SMAD4, TBX3, TP53*; **Ext. (+10):** *CREB1, E2F1, FOXO1, FOXO3, JUN, MYC, NFE2L2, RELA, SMAD2, SMAD3*
Receptor tyrosine kinases [7, 11, 34, 108] (16; 15/1)	**Bulk (15):** *CSF1R, EGFR, EPHA3, EPHB4, ERBB2, ERBB3, FGFR1, FGFR2, FGFR3, FLT1, FLT4, IGF1R, KDR, KIT, MET*; **Ext. (+1):** *INSR*
Intracellular signaling kinases [8–10, 41, 58, 63, 64] (40; 12/28)	**Bulk (12):** *AKT1, AKT2, AKT3, ARAF, BRAF, JAK1, JAK2, MAP2K4, MAP3K1, MTOR, PIK3CA, RAF1*; **Ext. (+28):** *ABL1, CHUK, CSNK1D, FYN, GSK3A, GSK3B, IKBKB, LCK, LYN, MAP2K1, MAP2K2, MAPK1, MAPK10, MAPK14, MAPK3, MAPK8, PAK1, PDK1, PDPK1, PRKAA1, PRKACA, PRKCA, PRKD1, PTK2, RPS6KA3, SRC, STK3, STK4*
Small GTPases, G-proteins & adaptors [13, 14, 34, 41] (13; 6/7)	**Bulk (6):** *GNAS, HRAS, KRAS, NF1, PIK3R1, TSC1*; **Ext. (+7):** *DAB2IP, GRB10, IRS1, NRAS, RAC1, SHC1, TSC2*
Protein & lipid phosphatases [41, 53, 58] (4; 1/3)	**Bulk (1):** *PTEN*; **Ext. (+3):** *PPP2CA, PTPN1, PTPN11*
Cell-cycle checkpoints, DNA repair & replication [62, 65, 66, 70] (18; 5/13)	**Bulk (5):** *ATM, CDK4, CDK6, CDKN2A, TOP1*; **Ext. (+13):** *ATR, AURKA, BRCA1, CDK2, CDK7, CDKN1A, CHEK1, CHEK2, PARP1, PLK1, POLD1, POLE, PRKDC*
Chromatin & epigenetic modifiers [40, 59, 103] (12; 11/1)	**Bulk (11):** *ARID1A, ARID1B, ASXL1, DNMT3A, EP300, EZH2, HDAC1, HDAC2, KMT2C, NCOR2, SETDB1*; **Ext. (+1):** *MEN1*
Ubiquitin–proteasome & E3 ligases [13, 14, 42, 53] (7; 3/4)	**Bulk (3):** *BIRC6, CYLD, FBXW7*; **Ext. (+4):** *CBL, ITCH, MDM2, TRAF6*
Cytokines, TGF-β & immune checkpoints [5, 57, 60, 109] (14; 6/8)	**Bulk (6):** *ACVR1B, ACVR2A, CD274, IL6, LAG3, VEGFA*; **Ext. (+8):** *FCGR2B, FCGR3A, HGF, IL6ST, LCN2, LIF, TGFB1, TIGIT*
Cell adhesion, cytoskeleton, ECM & scaffolds [13, 14, 33, 67] (13; 5/8)	**Bulk (5):** *AFDN, CCDC6, EML4, MYH9, NOTCH1*; **Ext. (+8):** *CDH1, CTNNB1, ELN, HSP90AA1, MMP2, MMP9, TACSTD2, TUBB3*
Ion channels, transporters & metabolic enzymes [33, 34, 67] (19; 2/17)	**Bulk (2):** *ATP1A1, CACNA1D*; **Ext. (+17):** *ABCA1, ABCB1, ABCC1, ABCC3, ATP2A2, CACNA1C, CACNB2, KCNH2, NT5E, PTGS2, SIRT1, SLC29A1, SLC39A6, SLC44A4, SLC6A9, SLC7A5, TYMS*

Table S9: Empirical verification of Hurwitz stability and first-order Neumann steady-state approximation across the four bulk tissue drift matrices ($\hat{B}_g = \mathcal{D}_g + O_g$ at $c_{\text{mult}} = 1.0$), related to Figure 3, Figure 4, and Methods. Here $\mathcal{D}_g = \text{diag}(\hat{B}_g)$ and $O_g = \text{offdiag}(\hat{B}_g)$ (Remark S3). The last three columns compare $N_1 = -\mathcal{D}_g^{-1} + \mathcal{D}_g^{-1} O_g \mathcal{D}_g^{-1}$ against the exact steady-state response matrix $-\hat{B}_g^{-1}$ via relative Frobenius error and off-diagonal Pearson correlation r (non-zero sign agreement in parentheses).

	Stability & Neumann convergence conditions				Frobenius norms of steady-state terms				1st-order Neumann accuracy (N_1 vs. $-\hat{B}_g^{-1}$)		
Bulk tissue cohort	Active reg. cols (of 100)	Max real eig. $\max_i \text{Re}\,\lambda_i(\hat{B}_g)$	Condition no. $\text{cond}(\hat{B}_g)$	Spec. rad. of $\mathcal{D}_g^{-1}O_g$ (< 1)	Exact full $\|-\hat{B}_g^{-1}\|_F$	Diag. term $\|-\mathcal{D}_g^{-1}\|_F$	Exact off-diag. $\|\text{offdiag}(-\hat{B}_g^{-1})\|_F$	1st-order off-diag. $\|\mathcal{D}_g^{-1}O_g\mathcal{D}_g^{-1}\|_F$	Full rel. err.	Off-diag. rel. err.	Off-diag. r (sign acc.)
LumA breast ($n = 498$)	68	−0.998	4.75	0.320	8.23	8.00	2.05	1.93	0.076	0.301	0.954 (0.898)
healthy breast ($n = 217$)	70	−0.767	8.92	0.441	9.66	8.96	3.76	3.82	0.138	0.351	0.940 (0.892)
CIN colorectal ($n = 245$)	85	−0.832	3.74	0.341	9.08	8.78	2.42	2.29	0.090	0.335	0.943 (0.893)
healthy colon ($n = 91$)	75	−0.559	20.62	0.747	10.99	8.83	6.63	6.32	0.383	0.630	0.793 (0.804)

Table S10: **End-to-end sensitivity across the ADMM column group-lasso multiplier $c_{\text{mult}} \in \{0.5, \ldots, 2.5\}$, related to Figures 2–5, Table 1, and Methods.** Stage 1: pass counts in synthetic single-cell (12 settings), synthetic bulk (3 tight 0.3-rad and all 9 settings), and U2OS pseudo-bulk (12 settings; cycle-phase / 157-gene panel mean r). Stage 2: active regulators in LumA, healthy breast (H-Br), CIN, and healthy colon (H-Col) [shared all-4], Hurwitz-unstable fits (of 4,004), external proxy hits (of 42), and 96-h L1000 shRNA knockdown p-values (24 perturbed vs. 93 assayed genes). Stage 3: shared same-sign links ($\epsilon = 2\,m_h$) across all 9,900 pairs and among all-4 active regulators, and 3-round bicluster score $\sum_{t=1}^{3} S_t$ [total / all-4 links]. Stage 4: Algorithm 2 mean rank-1 residual $r^\star$ across the 12 backbone/pool rows (*eprenetapopt* #1 count).

	1. Synthetic & U2OS recovery			2. Bulk network sparsity, stability & proxy validation					3. Cross-cancer subnetwork ($\epsilon = 2\,m_h$)			4. Drug rank
Penalty c_{mult}	Single-cell sim. pass (mean r / sign acc.)	Bulk sim. pass: tight; all 9 (mean sign acc.)	U2OS pass (cycle r / panel r)	Active reg. cols: LumA/H-Br/CIN/H-Col [shared all 4]	Unstable fits (of 4,004)	Proxy tests $p \le 0.10$ (≤ 0.05) / 42	LumA shRNA KD p-val. (24 / 93 genes)	CIN shRNA KD p-val. (24 / 93 genes)	Shared same-sign χ_{ij} (p)	All-4 active same-sign χ_{ij} (p)	Bicluster $\sum_{t=1}^{3} S_t$ (p-val.) [links / all-4]	Alg. 2 mean rank-1 $r^\star$ (*epren.* #1)
0.5	12/12 (0.441 / 0.847)	3/3; 4/9 (0.763)	12/12 (0.648 / 0.278)	81/80/93/88 [59]	0	8 (6)	0.146 / 0.149	0.004 / 0.002	678 (0.056)	564 (0.303)	36.875 (0.267) [107 / 93]	0.646 (1/12)
1.0 (main)	**12/12 (0.467 / 0.887)**	**3/3; 7/9 (0.790)**	**12/12 (0.652 / 0.328)**	**68/70/85/75 [40]**	**0**	**14 (8)**	**0.261 / 0.122**	**0.004 / 0.001**	**663 (0.014)**	**472 (0.054)**	**38.625 (0.131) [107 / 90]**	**0.652 (10/12)**
1.5	12/12 (0.478 / 0.908)	3/3; 4/9 (0.814)	12/12 (0.658 / 0.313)	63/61/75/68 [27]	0	16 (7)	0.155 / 0.068	0.003 / 0.001	566 (0.021)	289 (0.448)	34.250 (0.323) [99 / 56]	0.702 (2/12)
2.0	12/12 (0.484 / 0.916)	3/3; 5/9 (0.818)	12/12 (0.661 / 0.233)	59/56/65/59 [20]	0	12 (9)	0.039 / 0.031	0.009 / 0.001	413 (0.243)	192 (0.965)	28.750 (0.591) [93 / 51]	0.719 (3/12)
2.5	12/12 (0.487 / 0.926)	3/3; 5/9 (0.776)	11/12 (0.666 / 0.145)	52/52/59/58 [17]	0	12 (8)	0.023 / 0.018	0.015 / 0.001	352 (0.456)	143 (0.990)	24.875 (0.866) [86 / 34]	0.689 (0/12)

Table S11: **Sensitivity of Algorithm 2 drug-combination rankings to restricting regulators to those active in all four cohorts, to cell-line stratification, sign threshold ϵ, and rectangle size k_{rect}, related to Figure 5, Table 1, and Methods.**

Sensitivity setting	Links / regs	*Eprenetapopt* #1	Rank-1 partner shifts and permutation null summary
Baseline ΔB_{rect} ($\epsilon = 2.0\,m_h$, $k_{\text{rect}} = 8$, MCF7+HT29)	107 links (19 regs)	10/12 (mean 0.652)	*Eprenetapopt* #1 on 5 of 6 backbones (0.563–0.696); *tacedinaline* #1 on pictilisib (0.745). 0/12 rows at $p < 0.05$ ($p_{\text{net}} = 0.067$–0.748; $p_{\text{push}} = 0.063$–0.920; $p_{\text{push,ind}} = 0.061$–$0.949$).
90-link four-cohort subset (14 all-4 active regs)	90 links (14 regs)	6/12	Retains *eprenetapopt* #1 on palbociclib (0.645) and irinotecan/metab. (0.720, 0.808); shifts pictilisib to *dovitinib* (0.763), everolimus to *gefitinib* (0.739), and topotecan to *vemurafenib* (0.742). 0/12 rows reach $p < 0.10$ ($p_{\text{net}} = 0.202$–0.793, $p_{\text{push}} = 0.124$–0.967).
Cell-line 6-h pushes (MCF7-WT / HT29-mut)	107 links	3/12 / 2/12	Retains *eprenetapopt* #1 on palbociclib (plus irinotecan/metab. in MCF7); remaining rows shift to JAK/HDAC (*ruxolitinib, entinostat*) and PPARα/VDR (*gemfibrozil, calcifediol*) in MCF7, and to EGFR/MET (*gefitinib, erlotinib, lapatinib, crizotinib*) and *gemfibrozil* in HT29.
Sign threshold ($\epsilon = 1.5\,m_h$ / $2.5\,m_h$)	119 / 87 links	6/12 / 0/12	At $1.5\,m_h$, retains baseline #1 in 6/12 rows (8/12 in top 3). At $2.5\,m_h$, both *TP53* links drop out, shifting #1 to HDAC1/2, RTK, PI3K, and JAK inhibitors (*tacedinaline, entinostat, tivantinib, buparlisib, momelotinib, linsitinib*). VDR/PPAR agonists stay in the repurposing top 3.
Rectangle size ($k_{\text{rect}} = 3$ / 5)	26 / 57 links	2/12 / 0/12	Shifts oncology #1 to RTK, BRAF, and JAK inhibitors (*erlotinib, gefitinib, infigratinib, imatinib, lapatinib, linifanib, semaxanib, vemurafenib, ruxolitinib*) and repurposing #1 to VDR agonist *doxercalciferol* (0.740, 0.770).